IDENTIFICATION OF POSITION-DEPENDENT WORKPIECE DYNAMICS IN MILLING PROCESS

A THESIS SUBMITTED TO
THE GRADUATE SCHOOL OF NATURAL AND APPLIED SCIENCES
OF
MIDDLE EAST TECHNICAL UNIVERSITY

BY

BARIŞ ALTUN

IN PARTIAL FULFILLMENT OF THE REQUIREMENTS
FOR
THE DEGREE OF MASTER OF SCIENCE
IN
MECHANICAL ENGINEERING

AUGUST 2022

Approval of the thesis:

IDENTIFICATION OF POSITION-DEPENDENT WORKPIECE DYNAMICS IN MILLING PROCESS

submitted by **Barış ALTUN** in partial fulfillment of the requirements for the degree of **Master of Science** i**n Mechanical Engineering, Middle East Technical University** by,

Prof. Dr. Halil Kalıpçılar
Dean, Graduate School of **Natural and Applied Sciences** _____

Prof. Dr. Sahir Arıkan
Head of the Department, **Mechanical Engineering** _____

Assist. Prof. Dr. Hakan Çalışkan
Supervisor, **Mechanical Engineering, METU** _____

Assist. Prof. Dr. Orkun Özşahin
Co-Supervisor, **Mechanical Engineering, METU** _____

Examining Committee Members:

Prof. Dr. Melik Dölen
Mechanical Engineering, METU _____

Assist. Prof. Dr. Hakan Çalışkan
Supervisor, **Mechanical Engineering, METU** _____

Assoc. Prof. Dr. Hakkı Özgür Ünver
Mechanical Engineering, TOBB _____

Assoc. Dr. Bülent Özer
Mechanical Engineering, METU _____

Assist. Prof. Dr. Orkun Özşahin
Co-Supervisor, **Mechanical Engineering, METU** _____

Date: 25.08.2022

I hereby declare that all information in this document has been obtained and presented in accordance with academic rules and ethical conduct. I also declare that, as required by these rules and conduct, I have fully cited and referenced all material and results that are not original to this work.

Name Last name : Barış ALTUN

Signature :

ABSTRACT

IDENTIFICATION OF POSITION-DEPENDENT WORKPIECE DYNAMICS IN MILLING PROCESS

Altun,Barış
Master of Science, Mechanical Engineering
Supervisor : Assist. Prof. Dr. Hakan ÇALIŞKAN
Co-Supervisor: Assist. Prof. Dr. Orkun ÖZŞAHİN

August 2022, 129 pages

Frequency Response Functions (FRFs) are utilized for analyzing vibrations created during milling process. FRFs obtained with external excitations are often not sufficient as machine-tool dynamics are position-dependent (to machine-tool axes, workpiece placement) and frequency domain to be identified requires specialized equipment. In this thesis, an identification method based on operational excitation addressing these problems is proposed. A single rectangular workpiece is processed and acceleration measurements are taken. FRF is calculated according to the proposed method of sampling engagements individually and force calculation based on mechanistic models. Results are compared with tap test results. Force coefficients to be used are identified by tap tests obtained from a different spot and mechanistic force model by processing a similar rectangular workpiece. Results are confirmed with FRF obtained in the same location.

Keywords: Operational Modal Analysis, Position dependent Machine-Tool Dynamics, Identification of Force Coefficients, Chatter, Milling Force

ÖZ

KONUMA BAĞLI FREZE İŞ PARÇASI DİNAMİĞİNİN FREZELEME İŞLEMİNDE TANILANMASI

Altun,Barış
Yüksek Lisans, Makina Mühendisliği
Tez Yöneticisi: Dr. Hakan ÇALIŞKAN
Ortak Tez Yöneticisi: Dr. Orkun ÖZŞAHİN

Ağustos 2022, 129 sayfa

Frekans Tepki Fonksiyonları (FRF) frezeleme sürecinde oluşan titreşimlerin analizinde kullanılır. Dışarıdan gelen uyarımlarla elde edilen FRF'ler sıklıkla frezeleme sürecinde ortaya çıkan titreşimleri tanımlamakta yetersiz kalmaktadır. Bunun başlıca sebepleri FRF'in tezgahın o anki pozisyonuna bağlı olması (eksenler ve parça pozisyonu) ve incelenen frekans bölgesinin bölgeye uygun ekipmana ihtiyaç duymasıdır. Bu tezde, bu sorunları aşan operasyonel bir uyarım metodu sunulmuştur. Tek, dikdörtgen bir parça frezelenmiş ve ivme ölçümleri alınmıştır. Frekans Tepki Fonksiyonu bu çalışmada önerilen şekilde takım-temas ivmelerinin tek tek örneklenmesi ile mekanistik kuvvet modelleri sayesinde hesaplanmıştır.Sonuçlar çekiç testleri ile karşılaştırılmıştır. Kuvvet katsayıları freze tezgahının başka bir konumunda yapılan çekiç testleri ile yine dikdörtgen bir parçanın işlenmesi ile tanımlanmıştır. Sonuçlar aynı konumda elde edilen FRF'lerin çekiç testiyle karşılaştırılması ile doğrulanmıştır.

Anahtar Kelimeler: Operasyonel Modal Analiz, Pozisyona Bağlı Takım-Tezgah Dinamikleri, Kuvvet Katsayısı Tanımlamaları, Tırlama, Frezeleme kuvveti

ACKNOWLEDGMENTS

The author wishes to express his deepest gratitude to his supervisor Dr. Hakan Çalışkan and co-supervisor Dr. Orkun Özşahin for their guidance, advice, criticism, encouragements and insight throughout the research.

This work is partially funded by Scientific and Technological Research Council of Turkey under grant number TUBİTAK 218M430.

TABLE OF CONTENTS

LIST OF TABLES

TABLES

LIST OF FIGURES

FIGURES

LIST OF ABBREVIATIONS

ABBREVIATIONS	
FRF	Frequency Response Function
IRF	Impulse Response Function
IFFT	Inverse Fast Fourier Transform
RMSE	Root Mean Squares Error
SMAPE	Symmetric Mean Absolute Percentage Error

LIST OF SYMBOLS

$h_0(t)$	Static chip thickness [mm]
$h_j(t)$	Total chip thickness [mm]
c	Feed per insert [mm]
$\theta_j(t)$	Angular position per insert [rad] $j \in \{1,2, \ldots . N_t\}$ (j: Insert index)
N_t	Number of inserts
n_s	Angular speed of spindle [rad/s]
V_x	Feed in X direction [m/s]
τ	Time delay between two consecutive cutting tool-workpiece contacts [s]
K_{tc}	Tangential cutting force coefficient [N/m^2]
K_{rc}	Radial cutting force coefficient [N/m^2]
K_{te}	Tangential edge force coefficient [N/m]
K_{re}	Radial edge force coefficient [N/m]
a_p	Axial depth [m]
$g_j(t)$	Window function [Unitless]
$\mathbf{F}(t)$	Force vector (all in [N])
$\mathbf{F_s}(t)$	Static force vector (all in [N])
$\mathbf{F_d}(t)$	Dynamic force vector (all in [N])
$F_x(t)$	Force in X direction [N]

$F_y(t)$	Force in Y direction [N]
$\mathbf{x}(t)$	Displacement vector (all in [m])
$\mathbf{x_1}(t)$	Displacement vector of table (represented by workpiece) (all in [m])
$\mathbf{x_2}(t)$	Displacement vector of spindle (represented by cutting tool) (all in [m])
$x(t)$	Displacement in X direction [m]
$y(t)$	Displacement in Y direction [m]
$\mathbf{A}(t),\ \mathbf{A_p}(t),\ \mathbf{A_{p,2}}(t)$	Transformation matrices [unitless]
$\mathbf{A}(s),\ \mathbf{A_p}(s),\ \mathbf{A_{p,2}}(s)$	Laplace domain representation of transformation matrices [unitless]
$a_{xx}(t),\ a_{xx,2}(t),\ a_{xy}(t)$	Transformation matrice members [unitless]
$a_{yx}(t),\ a_{yx,2}(t),\ a_{yy}(t)$	Transformation matrice members [unitless]
D	Diameter of cutting tool [m]
f_{zc}	Zero crossing frequency [Hz]
$\mathbf{x}(s)$	Laplace transformation of displacement vector [m]
$\mathbf{x_2}(s)$	Laplace transformation of displacement vector of Spindle (represented by cutting tool) [m]
$\mathbf{x_1}(s)$	Laplace transformation of displacement vector of Table (represented by workpiece) (all in [m])
$\mathbf{G_1}(s)$	Workpiece transfer function (all in [m/N])
$\mathbf{G_2}(s)$	Cutting tool transfer function (all in [m/N])

$P_k P_r$	FRF from point k to point r [m/N]
$G(\omega)_{d,fg}$	Transfer function of d in fg direction. $D \in \{1,2\}$, $f \in \{x,y\}$, $g \in \{x,y\}$ [m/N]
N	Number of modes
ω_n	Mode frequency [rad]
ξ	Mode damping
k_n	Mode stiffness [N/m]
ΔT_{sim}	Time step of simulation [s]
P	Data per one turn of cutting tool
L	Wall thickness [m]
$H_{mn,d}(t)$	Force in d direction caused by K_{mn} [m^2]
$\mathbf{D_{Fmatr}}$	Assumption Ratio Matrice $D \in \{X,Y\}$ (all in [m^2])
K_A, K_B	Intermediate force coefficients [N/m]
$\mathbf{K_A}, \mathbf{K_B}$	Intermediate force coefficients' matrices (all in [N/m])
$\boldsymbol{\omega} = [\omega_1, \omega_2, \ldots \omega_n]$	All frequency points selected [rad] (n : number of frequency samples)
$X_i(\boldsymbol{\omega})_{n\times 1}$ $Y_i(\boldsymbol{\omega})_{n\times 1}$	Response at i_{th} engagement sampled (n : number of frequency samples)
$\mathbf{W_d}$	Weight column $d \in \{1,2\}$ [Unitless]
$\mathbf{H_d}$	Regressor matrice of d direction $d \in \{x,y\}$ [Unitless]
$H_{te,y}(t)$	Geometry matrice member [Unitless]

$\mathbf{P_{i,d}}$	Covariance matrice (alternatively called information matrice) at i_{th} engagement sampled for X direction $d \in \{x, y\}$ [Unitless]
$\mathbf{J_{i+1}}$	Kalman gain [Unitless]
$\mathbf{H_1}$	Regressor matrice of second least squares application
[m]	
$F_{q,i}(\omega)$	Force at i_{th} engagement sampled $q \in \{X, Y\}$ [N]
$q_i(\omega)$	Response at i_{th} engagement sampled $q \in \{X, Y\}$ [m/s^2]
$S_{qq,i}(\omega)$, $S_{qF,i}(\omega)$	Spectral density functions of i_{th} engagement [m/Ns^2]
$S_{Fq,i}(\omega)$, $S_{FF,i}(\omega)$	Spectral density functions of i_{th} engagement [m/Ns^2]
$C(\omega)$	Coherence [Unitless]
$g_{1,xx}$	IRF on xx direction [m/Ns^2]
M	Limit number of array size [Unitless]
$\mathbf{F_{\omega_n}}$	All force calculations at ω_n frequency point sampled. (all in [N])
I	Indexes to include in the equation as equation (2.17c)
$\mathcal{F}$	Fourier Transformation

CHAPTER 1

INTRODUCTION

Milling is a category of manufacturing processes under the name of "Machining" in which a rotating cutting tool makes contact with a stationary workpiece and this action removes material from the workpiece in a form of small particles of deformed workpiece material called "chips." A graphic description is given in Figure 1.1. By controlling the position of the workpiece and cutting tool, material from the workpiece can be removed in a controlled fashion and this gives the workpiece the desired shape. Milling process is an established practice in the industry as it is especially useful in shaping metals and manufacturing complex shapes as long as features are accessible from the surface. Some of the application areas may be listed as manufacturing of casting molds, firearms, missile bodies, shafts and other power transmission members.

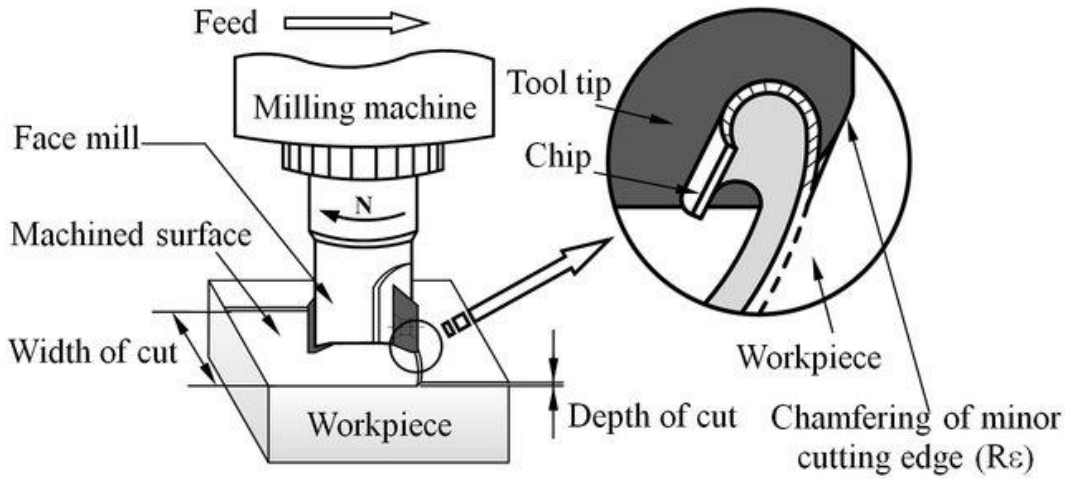

Figure 1.1 Description of Milling Process [1]

Just like all manufacturing processes, milling process has challenges. One major source of problems is vibrations present during operation. Because machining processes rely on material removal with an application of force in a small area, vibrations are inherent to machining processes. Vibrations are known to be detrimental to manufacturing results and harmful to machine-tool. For this reason, handling of vibrations in milling process is an important research area. Fundamentally, there are 3 types of vibrations are categorized. Transient vibrations occur when there is displacement but no additional force, such as when cutting tool leaves the workpiece. Forced vibrations are the direct result of force applied due to milling process itself. Self-excited (regenerative) [2] vibrations are observed with forced vibrations and caused by workpiece and machine-tool vibrations changing chip removal rate and consequently, the force applied. Regenerative vibrations are associated with a phenomenon called chatter when this self-excited event becomes unstable and starts diverging. Chatter can be diagnosed with abnormally high noise together with a characteristic wavy pattern left in the workpiece. Chatter results with poor surface finish and possible damage on workpiece and machine-tool.

The most critical thing to be known about these vibrations is the fact that just like any other vibration, they are a function of force applied and dynamic characteristics of machine-tool. In other words, machine-tool can be modelled and vibrations can be regarded as an output. This conclusion is used in some prominent ways such as chatter detection and suppression methods or chatter stability studies like Stability Lobe Diagram [2], various identification methods such as operational modal analysis [10], and even tool and spindle monitoring techniques related to noise and vibrations. This means that machine-tool identification techniques are in demand both in the Academy and the Industry.

One of the most useful methods to represent machine-tool behavior under excitation is utilizing Frequency Response Functions. FRFs are useful for milling dynamics analysis for several reasons. They are fairly easy to calculate and utilize in practice with minimal training. Since a lot of machinery used in industry, such as milling machines, have some sort of periodic or mostly periodic excitations, frequency

domain methods like FRF are well utilized for representing such dynamics of such systems. Utilizing multiple measurements for a better estimation is easy to apply with FRFs and for this reason, they function well with noise and uncertainties. Finally, together with some assumptions such as a linear system, they can be used to construct a transfer function.

1.1 FRF Identification Methods for Milling Machines

In the previous chapter, the motivation for obtaining FRF from machine-tool is explained. This chapter gives the literature regarding how to obtain FRF in machine-tool.

FRFs for milling applications are commonly obtained by measurement of output under excitation, i.e. empirically. These methods can be separated into two based on the method of excitation as experimental and operational. Experimental methods rely on external force application devices such as hammers or shakers and output measurements. Experimental methods to obtain desired data for identification is a practical and reliable approach in terms of excitation control and for testing a select few spots. Such methods are great at applying accurate excitation but implementing them can be challenging, especially during operation [22]. Operational approach is to obtain data during the machine under investigation is performing its intended task. In other words, excitation is provided by the system itself. In this approach, information regarding input excitation can be obtained through various methods depending on the system, such as modelling of the system or assuming randomized excitation such as white noise, as in Output-Only Modal Analysis which is the most common form of operational modal analysis methods. Operational methods have the potential to reflect behavior during operation more accurately but control over excitation is more challenging.

Empirical methods of obtaining FRF have vast literature behind them. Significant work has been put into Experimental and Operational Modal Analysis [3], as well as

obtaining FRF only, i.e. without modal analysis. Experimental Modal Analysis is a highly automatized identification method [3,4] and is widely used. Yet, modal analysis results are not equivalent to FRF obtained and even on highly automatized systems, the accuracy of results depends on abilities of the researcher. Operational method applications for the milling process have motivational reasons supporting their development, such as machine tool structure dynamics are known to change during operation [3,7,8-11,13-15,17,21] and application of experimental methods during operation requires additional work as excitation reflecting operation conditions can be necessary and challenging to satisfy as an application of force at a specific spot can require accommodations [3,22].

Obtaining the desired excitation on operational methods is an important research area for milling applications. Major challenges regarding milling process are uncertainty in force excitation due to the complexity of the process and harmonic excitation being dominant during operation. Özşahin et.al. [13] utilize a workpiece with randomized channels and processed this workpiece with feed direction vertical to the side of a set of walls in order to achieve randomized excitation. The excitation method is confirmed with coherence function and frequency content of excitation. Dynamometer measurements are taken as input and a laser vibrometer is used on cutting tool. Li et.al. [10] utilize inertia of the machine itself for excitation for identification of machine tool structure at lower than 500 [Hz] domain where main structural mode frequencies reside. The core idea is to shake the machine tool by moving the table and the spindle of the machine under investigation at a desired speed and acceleration. The core purpose of the paper is to show differences in the dynamics of the worktable (table) at different movement speeds and locations. The method provides mode frequencies and damping ratios but not amplitude as there is no force measurement and the method relies on a flat frequency profile. In other words, scaling is missing Author explains which parameters change during the process. Li et.al. [11] apply the first single thin workpiece for machine tool identification. This method assumes an impulse model for excitation which is explained by parameters such as angular speed, feed and wall thickness for

excitation. The method intents to achieve white noise for application of Operational Modal Analysis methods. This article also offers several simplified calculations for estimating where excitations will be effective. Cai et.al. [7] have taken the method used by Li et.al. and in order to obtain better random signal which is used with Output Only Modal Analysis methods, designed a workpiece with a randomized shape. Moreover, the authors also randomized angular speed and feed. Berthold et.al. [21] apply the same principle with a generic process and have shown that white noise requirements can be satisfied without a special workpiece. The author also presents methods to select process parameters to achieve excitation with various frequency content. Koike et.al. [6] apply chip regeneration model with servo motor information to check chatter stability experimentally through a spindle model and real time data. This is not an identification application but sensors present in the machine itself is used to describe tool-tip behavior. Similar applications are done for force calculations. [20, 23] Wang et.al. [8] have also applied a designed workpiece but only targeted modal shapes and for heavy machinery by randomized channels approach. So far, the scaling issue had not been mentioned. There are various ways to approach scaling. The mass change approach is popular for cutting tool identification [9, 26] but it is hard to apply on heavy moving parts such as machine-tool table. Peng et.al. [9] address this issue with a hybrid approach. The author utilizes movement and so inertial forces of the machine tool structure for identification. In addition, the author utilizes tap tests on the same machine. Mode shapes are expected to stay stable during operation and mode frequencies and damping are obtained through operational modal analysis. Iglesias et.al. [12] utilize a simple sweeping method for exciting desired frequency domain for identification. Force and acceleration measurements were present. This method gives excellent control over excitation frequency and is very intuitive to use. The author also explains non-diagonal members of the transfer function matrice and how to obtain them. A major disadvantage of this method is that exciting higher frequencies can be limited by spindle speed. Berthold et.al. [12] compare EMA and OMA methods while questioning position dependence and time-invariance of the machine itself and

identifies regions (position of spindle and table) with constant FRF on the investigated machine. This is critical to maintain the white noise assumption. Li et.al. [15] develop another inertia based application. In this case, multiple axes are moved simultaneously for more accurate results. Effects of machine tool structure itself on transfer functions, namely collisions inside the screw nut pair and impact excitation as a result of it are given as problems and so different sequences of impulses are tested to see if there is a nonlinearity as a result of it. Results indicate no significant nonlinearity. There have been studies regarding FRF identification or utilization without force measurement for table of machine tool structure. One critical work is that of Cai et.al. [18]. This article applies a conventional uncut chip thickness based cutting force model with previously known force coefficients in order to obtain an input similar to white noise but predictable. The advantages of this approach are that the method obtains a great amount of test data and force calculation is confirmed with measurements. Moreover, this approach gives a great deal of control over force excitation. However, problems with the reliability of force coefficients and phase measurement are reported.

The current research area regarding modal analysis without measurement of force measurements relies heavily on white noise production at desired frequency domain in order to obtain modal shapes. This means identification quality is based on the quality of produced white noise and while modal parameter identification can be accurate, it necessarily includes these additional assumptions. Compounding with the fact that FRFs of machine-tool, especially table, is position dependent and so accurate positioning can be necessary, white noise approaches or even experimental methods can be not sufficient. Methods with force information are possible as Cai et.al. [18] have shown but they either require force measurement or accurate estimation of force in which it requires some initial knowledge.

1.2 Force Modelling

In the previous chapter, it is shown that some form of force data is necessary for FRF identification unless output only methods are utilized. One method of obtaining force data is (direct or indirect) measurement of force. Taps and shakers automatically does force measurement but for other methods additional sensors are necessary. Dynamometers are commonly used for such applications. However, dynamometers have some issues preventing them from widespread application. Many facilities, industrial or academic, do not possess such device. They are significantly expensive. Moreover, they are cumbersome as they are required to be attached to the table and used as a workpiece holder to function. This would change table dynamics. Indirect measurements with accelerometers or encoders are a possibility but they require knowledge of the machine-tool beforehand as this is not an option if identification of the said machine-tool is the mission. Another method of obtaining force data is force calculation. Force calculation does not have the same equipment limitation or knowledge requirement regarding the machine-tool but it requires process parameters such as axial depth or angular speed of cutting tool.

There are multiple approaches to force calculation in milling. Empirical models are interpolated formulations that are on top of experimental data. Such an approach is cumbersome and preferred only when other approaches are infeasible but most force calculation approaches are at least partially empirical as force coefficients need to be determined. Finite Element Analysis and similar numerical calculations are preferred for studies regarding contact surface and deformation zone research of machining applications and they are not easily scalable. Mechanistic calculations are the most popular and suitable calculation method for force estimation of milling process beforehand. Mechanistic models are based on geometric calculation of static chip thickness with process parameters and force coefficients which are usually obtained empirically. Total chip thickness is the summation of dynamic and static chip thicknesses. Static chip is calculated based on geometry of workpiece, cutting tool and kinematics and it is explained in this section. Dynamic chip thickness is based

on displacements that are the result of milling forces applied and they are explained in Chapter 1.3. The oldest known model regarding static chip thickness comes from Martellotti [27]. This model takes cutting tool edge as circular and takes cutting tool geometry ideal. In this model, the force is based on cutting tool angular position, diameter of cutting tool and feed per insert. This model is suitable when feed per tooth is small compared to cutting tool diameter. In literature, there are more advanced models with more process parameters [28]. Especially in micro-machining, there are models based on high eccentricity and high feed per tooth compared to cutting tool diameter [29]. Moreover, works such as the study of Niaki et.al. [30] offer geometry based numerical static chip thickness calculation methods as an alternative to analytical calculations. Such methods have high calculation cost but they are easily adaptable to various conditions and they are selected on trochoidal milling. As important as calculating static chip thickness, application to the tool geometry is also a must. Koenigsberger et.al. [31] are the first people to develop mechanistic model of milling process. Kline [32] include tool eccentricity into calculation. All models mentioned above utilizes coefficients called as force coefficients. These parameters change values depends on process parameters and the material of workpiece. Such a change may be critical depending on the application. Considering this factor, linear and nonlinear milling force models can be selected. Linear milling force models rely on constant force coefficients and edge force coefficients as such a model relies on the assumption that force coefficients does not change drastically under the process parameters selected during milling [33]. This means that such a model is suitable under a range of process parameters they should not be exceeded. Nonlinear milling force models utilizes force coefficients that are an exponential function of chip thickness and possibly many other process parameters. Compared to linear milling force model force coefficients, they can be applied to a wider range of process parameters but they are harder to obtain. Force coefficients in general are affected by multitude of factors [28] such as chip thickness [33], cutting tool geometry, cutting tool material and workpiece material [34]. Although it is observed comparably rare, literature also includes axial depth and

cutting tool angular speed of cutting tool [35] as possible process parameters to effect force coefficients.

1.3 Process Modelling

Given that force is created during chip removal and chip removal effects force itself, there should be a process model explaining this behavior. Dynamic chip regeneration model commonly used in chatter research in machining processes is the default approach regarding milling dynamics. This model is also used with mechanistic force calculations and transfer functions of machine-tool.

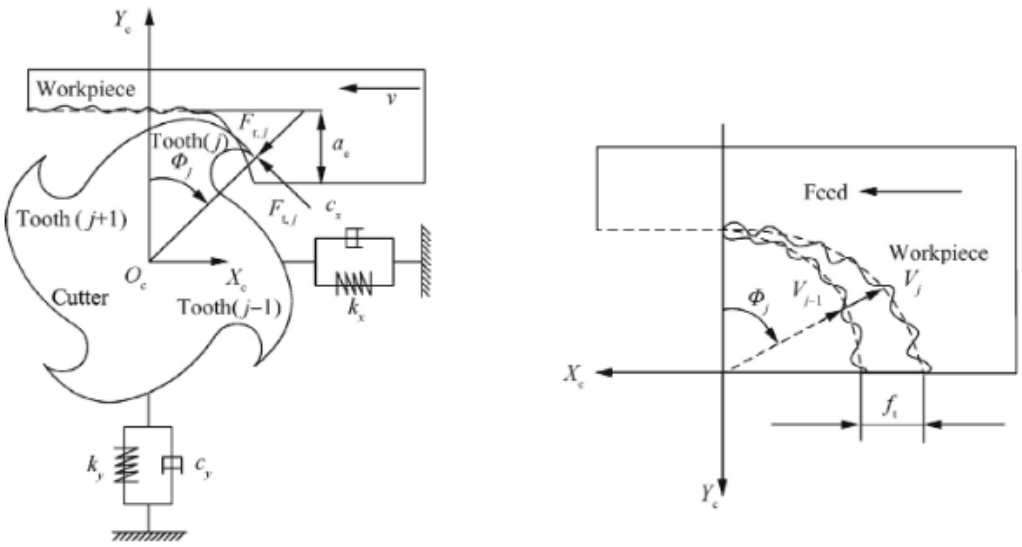

Figure 1.2 Example Demonstration of Milling Dynamics (A Review Of Chatter Vibration Research In Milling [40])

Entire milling dynamics can be described with merging of force model and cutting tool-workpiece vibration model. Force created during milling process is a function of chip thickness. Chip thickness is not just effected by process parameters but also displacement at workpiece and cutting tool as a result of force created. Since such a displacement during tool contact changes chip thickness, this causes a different amount of chip removed the next time cutting tool makes a contact. This results in a closed loop system in which chip thickness functions as delayed feedback [39].

Delay differential equations are usually analyzed under chatter research and they are the basis of self-excited vibration models [40].

1.4 Identification of Force Coefficients

Accurate information of force coefficients requires time and money investment to get. As the first approach, getting accurate force coefficients from literature is challenging from multiple points. First of all, there is no widely available database for such parameters that is easily reachable, contains desired information regarding materials or process parameters selected and accurate. Another factor is that force coefficients are usually specific to given cutting tool unless it is a generalized identification like orthogonal cutting test. Finally, material characteristics are varied from one manufacturer to another. Given these conditions, available coefficients without required knowledge of their method of obtainment are useful as a proxy and not much else. As the next approach, application of identification methods where or when it is needed with materials and tools to be used is attractive and this is an applied way of solving this problem. However, this usually requires a dynamometer for force measurement. Issues with dynamometers are mentioned in force modelling Chapter 1.2.

Force calculations without direct force measurement is a research area with multiple approaches. Aggarwal et.al. [20] utilize applied spindle motor current measurements together with inefficiencies on spindle structure to calculate tangential force coefficients. This method requires extensive initial study and only obtains tangential cutting force coefficient. Zhou et.al. [25] apply Kalman filter and tap test results to calculate force excitation. Yamato et.al. [21] apply motor current along with encoder readings and applies modelling of feed drive system to obtain force estimation. Load side disturbance observer (LSDO) relies on multiple encoder measurements and tool tip models. The method demands a force measurement reference for obtaining machine-tool parameters such as mass but process parameters or tap tests are not involved. Encoder measurements can require a strong enough excitation for

significant signal. Force observers in milling are an important research area but they are mostly omitted in this literature research because using indirect measurement in a machine-tool to be identified is challenging.

Regarding identification of force coefficients without dynamometer, Pawelko et.al. [19] perform the most prominent research regarding this area. Pawelko et.al. [19] utilize FRF measurements for identification of force coefficients and lists various error factors. The method applied is based on frequency domain representation of force model at only first two harmonics and workpiece dynamics are assumed rigid. The main issue the article addresses is that obtaining all four linear force model force coefficients at the same time requires ill-conditioned matrices and Tikhonov regularization can be applied for this problem. The method is only tested numerically Wang et.al. [41] utilize only one dominant modes of FRF to obtain a mass-spring-damper equation and by applying convolution, a set of linear equations in time domain to be used for least squares are created. The method does not give coefficients and results are accurate in amplitude for high radial engagement.

1.5 Scope of the Thesis

This thesis presents an easy-to-implement, in-operation identification method that offers more control over excitation compared to tap tests and the method offered has better control over the position force applied. In other words, this thesis proposes a quasi-operational FRF identification method for the table of a milling machine which can easily be applied in multiple spots with varying excitation levels and which does not rely on modal analysis. This is achieved by a force excitation that is obtained with pre-planned process and designed workpiece. The workpiece offered in this thesis is a single rectangular workpiece that is cut with small radial engagement. This provides a set of impulse-like force applied on a certain position with calculable amplitude distributed into a path, reaching numbers possibly more than a thousand individual excitations. Details regarding the utilized workpiece, the force model and the identification process are provided in their respective chapters.

The first step is to simulate the milling dynamics to observe effects of process parameters, dynamic chip thickness and transfer functions. This step allows to demonstrate accuracy and efficiency of following steps, as well as explains modelling choices, theoretical background and practical limitations regarding both the modelling itself and how process parameter selections affect identification methods to be applied in following chapters. Figure 1.3 describes the approach followed in this chapter. A milling dynamics model is developed. The model developed includes chip regeneration, transfer functions obtained with FRFs measured from the same milling machine the experiment performed, the force model and static chip thickness calculations chosen. Process model is a set of calculations obtained from the model that are merged together in order to be programmed. For programming, two different approaches are tested as MATLAB™ Simulink and Convolution Integral. Their differences are explained. Experiment is performed with same process parameters used in the model is confirmed with comparing acceleration data obtained from both approach.

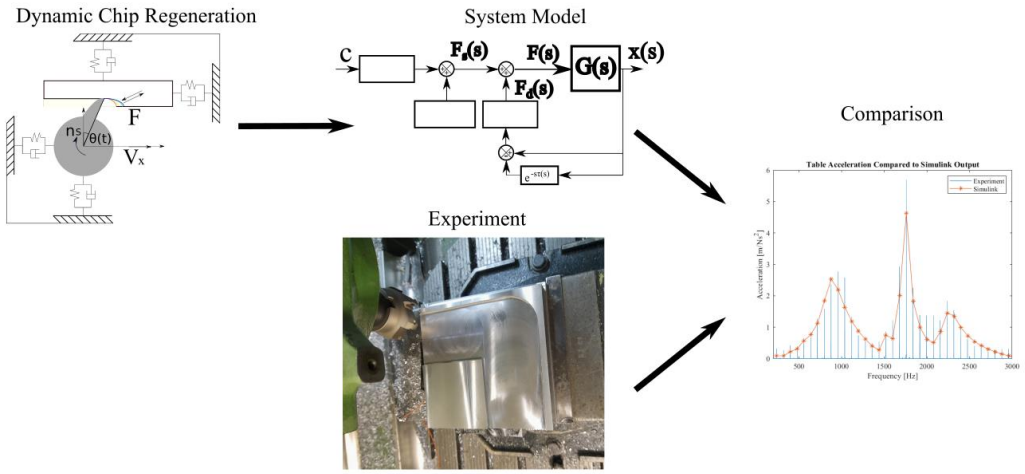

Figure 1.3 Milling Dynamics Model Verification

For identification, this thesis is separated into two steps. Figure 1.4 summarizes the approach. Since force is calculated, force coefficients must be accurate. In the first step, force coefficients are identified by tap tests applied on a selected spot in table and milling process performed in the same spot on table. In the second step,

identified force coefficients are used to obtain FRF from different, various positions with engagements and responses sampled from data. Details of these approaches are given in their respective chapters.

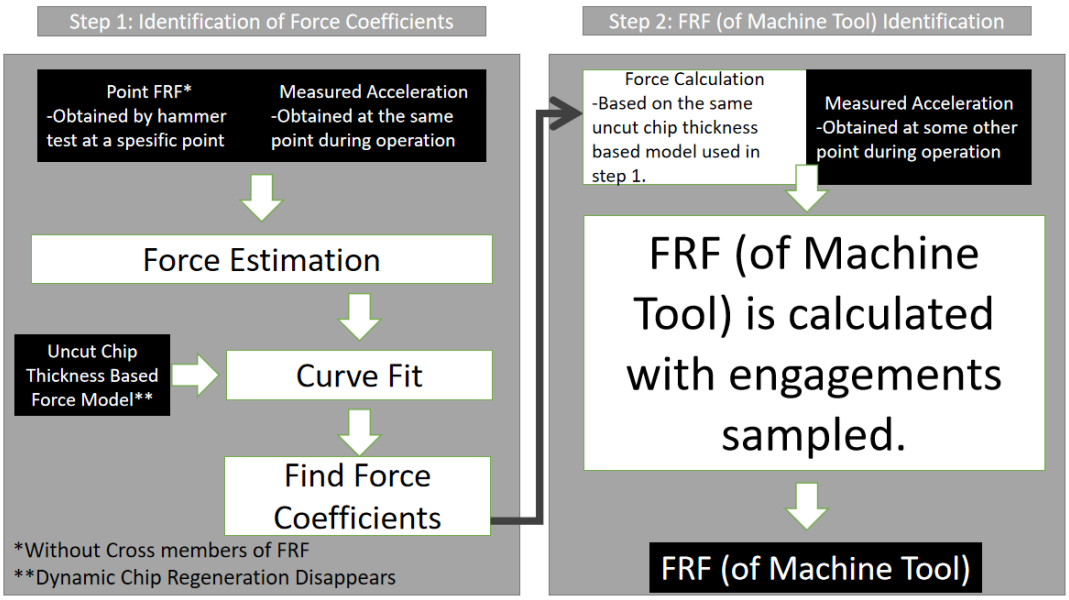

Figure 1.4 Identification Approach Summarized For Force Coefficients and FRF of Machine Tool Table

This thesis is separated into 6 chapters. In Chapter 2, a milling dynamics and force model to be used are introduced, along with the simulation developed. Chapter 3 explains identification of force coefficients. Chapter 4 explains the FRF identification method offered. Chapter 5 gives the experiment procedure and application of identification procedures introduced in the previous two chapters. Chapter 6 concludes the thesis.

CHAPTER 2

MILLING DYNAMICS MODEL

In Chapter 1.5, the intent and purposes of the process model have been explained only briefly. In this section, details are provided. There are two fundamental reasons utilization of a process model for milling dynamics in this thesis. The first reason is to address dynamic chip thickness and its effects on the excitation. It should be reminded that the method of excitation in this thesis is force application by a carefully designed milling process. The core purpose of this thesis is to identify the table of a milling machine considering its dynamics is position dependent, and this position dependency suggests an excitation method that has high distance resolution. In other words, fine control over where to apply force is desired. In addition, given applications in literature utilizing similar excitation methods and advantages they offered over such as controlling excitation levels and observing possible changes of dynamics during operation, this approach proves useful. However, there is no dynamometer available to measure the force excitation by process and even if there was one, it is heavy, cumbersome and it can change table dynamics. In other words, it cannot be used for the identification of table dynamics unless there is high confidence that it does not change table dynamics to be identified. This problem led to force calculation methods as an alternative method of regaining necessary knowledge regarding excitation input. The problem with utilizing force calculation methods is that self-excited vibrations change the force applied by chip regeneration. This means that static chip thickness based methods should not be applied directly before addressing dynamic chip thickness. The second reason the milling dynamics model for this thesis has been developed is to be able to test identification methods

before applying them to experimental results because experiments are costly both in terms of time and money.

The milling dynamics model to be used should reflect the purpose it is going to be used. In this thesis, linear milling force model is used and force coefficients are found experimentally. How they are found in this thesis is given at Chapter 3. For static chip thickness, Martellotti model [1] is deemed enough. A 2D delay differential equation model is utilized for X and Y directions of both table and spindle. For obtaining FRF, tap tests have been utilized. The model is programmed with two alternative solutions. The first approach is utilizing MATLAB Simulink and the second approach is utilizing convolution integral. For MATLAB Simulink, transfer functions are obtained with analysis done with CutPro. For the convolution integral approach, impulse response functions obtained with Inverse Fast Fourier Transform (IFFT) are utilized. The reasoning behind applying two different models is that so difference caused by modal analysis and transfer function format of MATLAB-Simulink model can be tested as the convolution model does not use transfer functions obtained with modal analysis. Details are provided at Section 2.2.2. Models are tested by comparing the output of models with an experiment using the same process parameters. Considering the frequency domain where tap test results may be deemed reliable (in other words where coherence is high), in order to excite the given frequency domain, workpiece dimensions and process parameters such as angular speed of cutting tool have been selected accordingly.

Chapter 2.1 explains the entire model's theoretical foundation. Chapter 2.2 explains MATLAB Simulink model and convolution integral model programmed. Chapter 2.3 validates the model with experimentation and discusses results obtained.

2.1 Mathematical Model Overview

Under this study, vibrations of spindle and table on X and Y directions are analyzed. Description of milling process is given in Figure 2.1. Here, the table of machine-tool ("table" for short) is represented by $G_{1,xx}(s)$, $G_{1,yy}(s)$ and the spindle of machine

tool (“spindle” for short) is represented by $G_{2,yy}(s)$, $G_{2,xx}(s)$. For transfer functions between X and Y directions, for table $G_{1,xy}(s)$, $G_{1,yx}(s)$ and for spindle $G_{2,xy}(s)$, $G_{2,yx}(s)$ are used. Transfer functions are given together in matrice form as shown in equation (2.13), as $G_1(s)$ for table and $G_2(s)$ for spindle. Dynamic chip thickness is briefly described in the figure. This entire model is explained in detail at Chapter 2.1.1.

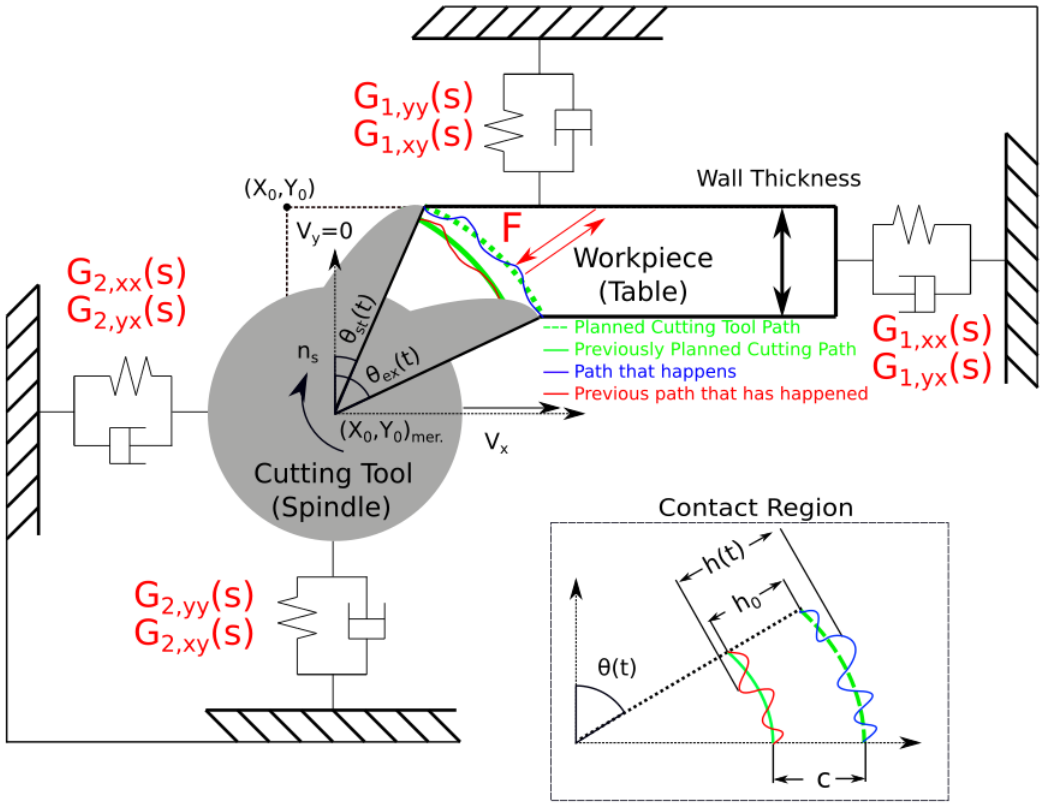

Figure 2.1 Milling Dynamics and Chip Regeneration

Workpiece and cutting tool transfer functions at the contact region are used for representing table and spindle dynamics respectively. These transfer functions are the ones which affect vibrations at the contact region. In other words, transfer functions utilized in this thesis represent the relation between force excitation at the contact region and vibration at the contact region.

To make the presentation of the model easier, milling dynamics has been separated into three parts. In Chapter 2.1.1, mechanistic force model utilized is explained. This chapter also explains selection principles regarding process parameters. As mentioned in this chapter, this model is not enough by itself to calculate force if there is dynamic chip regeneration present. Chapter 2.1.2 explains transfer functions to be used, how to obtain them and how to apply them in calculations. This chapter also presents transfer functions that are obtained. Chapter 2.1.3 explains utilizing these together.

2.1.1 Selection of Process Parameters for Mechanistic Force Model

Cutting force, F, is the result of chip removal. Chip thickness is the sum of static chip thickness based on feed per insert and dynamic chip thickness based on vibrations between cutting tool and workpiece as in chip regeneration factor. Figure 2.1 describes chip regeneration. Milling force created during operation pushes workpiece and cutting tool from their ideal path and this creates a difference in chip thickness when cutting tool contacts with workpiece for a second time. Ideal paths lead to static chip thickness h_0 [m]. Chip thickness is measured in radial direction and static chip thickness depends on cutting tool angular position of cutting tool θ_j as given below:

$$h_0(t) = c \sin \theta_j(t) \qquad j \in \{1,2, \dots . N_t\} \tag{2.1}$$

where c [m] gives feed per insert and it is a function of feed in X direction V_x[m/s] gives, angular speed of cutting tool n_s [rad/s] and number of inserts N_t. It is found as equation (2.2). j gives insert index.

$$c = \frac{V_x}{\frac{n_s}{60} N_t} \tag{2.2}$$

In practice, cutting tool deviates from following a kinematically determined path, as shown in Figure 2.1. Since the same situation applies for the previous contact of

workpiece and cutting tool, chip thickness is given as difference on the radial direction between two real paths as below:

$$h_j(t) = h_0(t) + [x(t) - x(t-\tau)]\sin\theta_j(t) + [y(t) - y(t-\tau)]\cos\theta_j(t) \qquad j \in \{1,2,\dots . N_t\} \tag{2.3}$$

Here, $x(t-\tau)$ and $y(t-\tau)$) gives the surface left from the previous contact of workpiece and cutting tool. τ [s] describes time passes between two contacts. τ [s] can be found with angular speed of cutting tool n_s and number of inserts N_t as below:

$$\tau = \frac{n_s}{N_t 60} \tag{2.4}$$

Forces in radial and tangential directions are given below:

$$F_{r,j}(t) = \left[K_{rc} h_j(t) + K_{re}\right] a_p g_j(t) \tag{2.5}$$

$$F_{t,j}(t) = \left[K_{tc} h_j(t) + K_{te}\right] a_p g_j(t) \tag{2.6}$$

Here, K_{tc} [N/m^2] and K_{rc} [N/m^2] gives tangential and radial cutting coefficients and K_{te}[N/m] and K_{re}[N/m] gives tangential and radial edge force coefficients. **Axial depth of cutting tool is given with constant a_p and chip thickness $h_j(t)$ is given in equation (2.3). Helix angle is omitted and cutting tool is selected according to this assumption as shown in Figure 5.2**. During the process, workpiece and cutting tool makes a contact at only a domain of angles. This domain is represented with the window function $g_j(t)$ as in equation (2.7). There is contact during cutting tool insert and workpiece when cutting tool angle is between θ_{st} and θ_{ex} as given in Figure 2.1.

$$g_j(t) = \begin{cases} 1, & \theta_{ex} \geq \mathrm{mod}(\theta_j(t), 2\pi) \\ 0, & \text{otherwise} \end{cases} \quad j \in \{1,2,\dots . N_t\} \tag{2.7}$$

Angular position of cutting tool (per inserts) $\theta_j(t)$ is given below for constant angular speed of cutting tool.

$$\theta_j(t) = 2\pi\left(\frac{n_s}{60}t + \frac{j-1}{N_t}\right) \quad j \in \{1,2,\dots.N_t\} \tag{2.8}$$

In this thesis, a shoulder face mill with inserts is selected and only one insert is used. This means that $N_t = 1$, as shown in Figure 5.2.

Because vibrations are measured at X and Y directions, a transformation calculation from radial coordinates to Cartesian coordinates is necessary. It is given at equation (2.9a).

$$\mathbf{F}(t) = \begin{bmatrix} F_x(t) \\ F_y(t) \end{bmatrix} = \mathbf{F_d}(t) + \mathbf{F_s}(t) \tag{2.9a}$$

$$\mathbf{F_s}(t) = a_p K_{tc} c \mathbf{A_p}(t) + a_p K_{te} \mathbf{A_{p,2}}(t) \tag{2.9b}$$

$$\mathbf{F_d}(t) = a_p K_{tc} \mathbf{A}(t)[\mathbf{x}(t) - \mathbf{x}(t-\tau)] \tag{2.9c}$$

where $(t) = [x(t) \quad y(t)]^{\mathbf{T}}$. Here, $\mathbf{F}(t)$ gives total forces in X and Y directions. Force caused by static chip thickness $\mathbf{F_s}(t)$ is given as equation (2.9b) and likewise, force caused by dynamic chip thickness $\mathbf{F_d}(t)$ is given as equation (2.9c). Similarly, displacement at X and Y directions are represented with $\mathbf{x}(t)$. $\mathbf{A}(t)$, $\mathbf{A_p}(t)$ and $\mathbf{A_{p,2}}(t)$ represents window function, angular relations and forces in general. Equation (2.10a) to (2.10g) explains $\mathbf{A}(t)$, $\mathbf{A_p}(t)$ and $\mathbf{A_{p,2}}(t)$ with matrice members.

$$\mathbf{A}(t) = \frac{1}{2}\begin{bmatrix} a_{xx}(t) & a_{xy}(t) \\ a_{yx}(t) & a_{yy}(t) \end{bmatrix} \quad \mathbf{A_p}(t) = \frac{1}{2}\begin{bmatrix} a_{xx}(t) \\ a_{yx}(t) \end{bmatrix} \quad \mathbf{A_{p,2}}(t) = \begin{bmatrix} a_{xx,2}(t) \\ a_{yx,2}(t) \end{bmatrix} \tag{2.10a}$$

$$a_{xx}(t) = -g(t)\left[\left(\sin 2\theta(t)\right) + \frac{K_{rc}}{K_{tc}}\left(1 - \cos 2\theta(t)\right)\right] \tag{2.10b}$$

$$a_{xx,2}(t) = -g(t)\left[\left(\cos\theta(t)\right) + \frac{K_{re}}{K_{te}}\sin\theta(t)\right] \tag{2.10c}$$

$$a_{xy}(t) = -g(t)\left[\left(1 + \cos 2\theta(t)\right) + \frac{K_{rc}}{K_{tc}}\sin 2\theta(t)\right] \tag{2.10d}$$

$$a_{yx}(t) = g(t)\left[\left(1 - \cos 2\theta(t)\right) - \frac{K_{rc}}{K_{tc}}\sin 2\theta(t)\right] \tag{2.10e}$$

$$a_{yx,2}(t) = g(t)\left[\left(\sin\theta(t)\right) - \frac{K_{re}}{K_{te}}\cos\theta(t)\right] \tag{2.10f}$$

$$a_{yy}(t) = g(t)\left[\left(\sin 2\theta(t)\right) - \frac{K_{rc}}{K_{tc}}\left(1 + \cos 2\theta(t)\right)\right] \tag{2.10g}$$

A general description of the milling process and the workpiece to be cut are shown in Figure 2.1. **Entry and exit angles, axial depth, feed, feed direction and angular speed are known through the geometry of the workpiece and process parameters. All of these parameters are kept constant for repeating the same excitation.** Together with this knowledge and force coefficients, the force is calculated through equations (2.10a) and its pieces, $\mathbf{x}(t-\tau)$ and $\mathbf{x}(t)$. As mentioned previously in the beginning of Section 2.1, $\mathbf{x}(t-\tau)$ and $\mathbf{x}(t)$ require process dynamics to be known and those are explained in the next chapter. The primary selection of workpiece geometry is a single thin walled workpiece that its' centerline is aligned to the feed direction In other words, $\theta_{st} + \theta_{ex} = \pi$, as shown in Figure 2.2. Workpieces that do not obey this rule (offset workpiece) are omitted from identification of force coefficients.

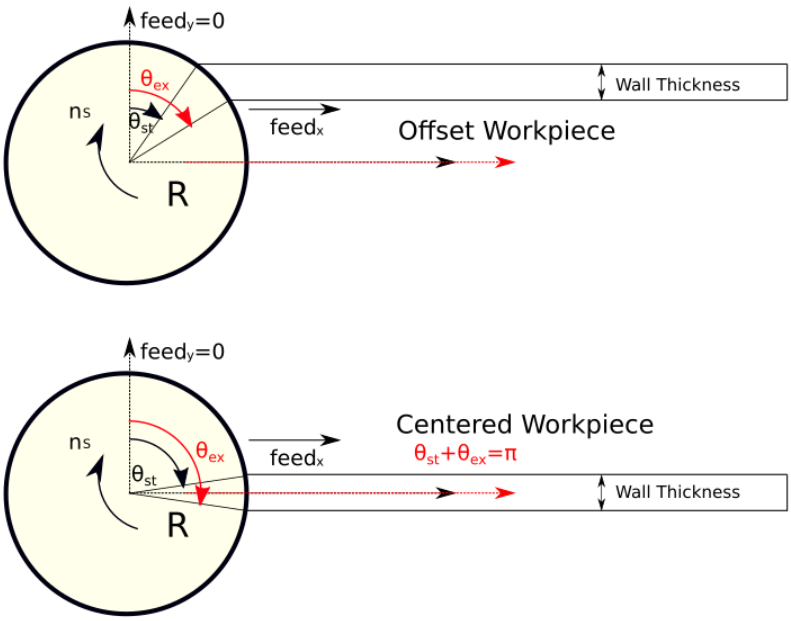

Figure 2.2 Centered Workpiece and Offset Workpiece

A centered workpiece has several advantages. Given that qualities of static force are critical because it is used for identification at following chapters and the fact that this thesis is primarily challenged by not being able to measure the force applied with a dynamometer; a simple excitation is desired and a centered workpiece helps to simplify the procedure. This means for the selection of a centered workpiece:

1. Due to low angular engagement, force excitation takes short time and is impulse-like. This means that the frequency bandwidth of force is high and uniform as possible. As an additional benefit, low radial engagement also reduces dynamic chip thickness.

2. The workpiece is easy to produce as the shape is simple. Moreover, positions of tool-workpiece engagement are easy to calculate and this is helpful for localized identification of FRF.

3. Cartesian forces ($F_x(t)$ and $F_y(t)$) are dominantly affected by tangential and radial forces and they are decoupled in case tool path coincides with the axis of the workpiece (longitudal centerline of the workpiece).

4. Change in static chip thickness during contact is limited as possible. In a milling process where chip thickness varies significantly at logarithmic scale, such as down-milling, nonlinear force model with exponential force coefficients would be required.

5. As it is shown on the next page, there is a certain level of control over force excitation characteristics by controlling milling process parameters.

Here is a sample static force calculation done with the given equation (2.9b) to show basic manipulations on the input on a centered workpiece. Process parameters can be used to control amplitude, harmonic peaks and frequency domain but not independently. For example, angular speed of cutting tool affects amplitude but also harmonic frequency and zero crossing position. Some of these relations were noted earlier [11]. Effects of angular speed and wall thickness at cutting force in the frequency domain are as shown in Figure 2.3.

Zero crossing is where excitation reaches zero. The frequency of this point f_{zc}[Hz] is engagement duration and is defined as equation (2.11). Here, L gives distance cutting edge travels during the process, which is roughly wall thickness.

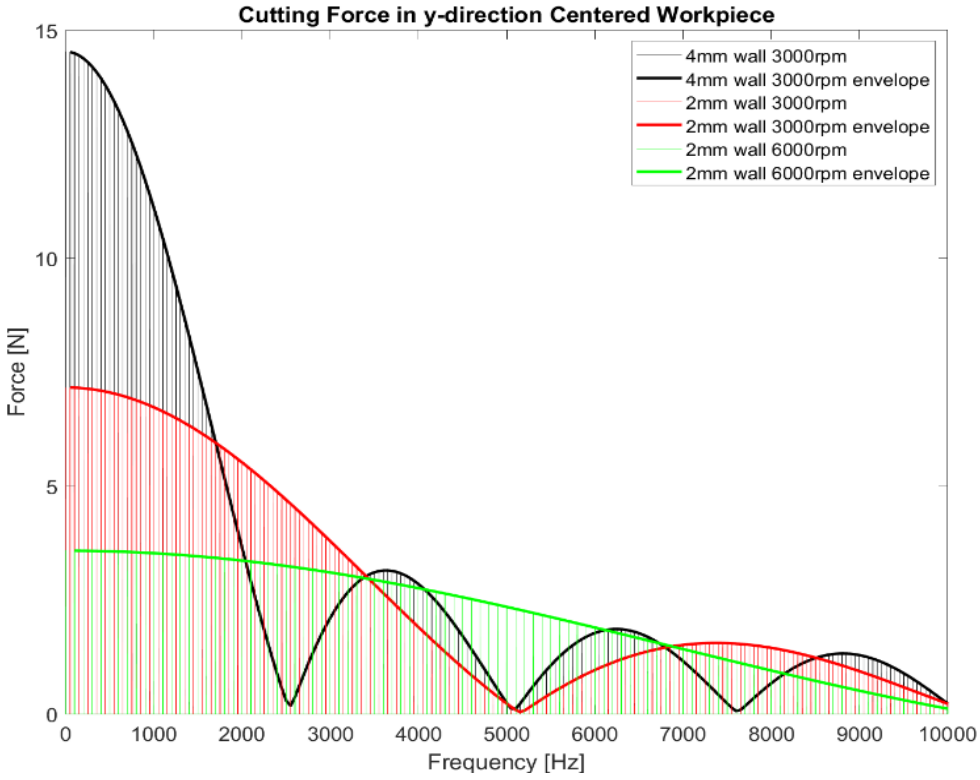

Figure 2.3 Effects of Angular Speed and Wall Thickness on Cutting Force Spectrum, Centered Workpiece, Tool Diameter: 65 [mm], Axial Depth Of Cut: 2.9 [mm], K_{tc}=1319 [Mpa], K_{rc}= 788 [Mpa]

$$f_{zc} = \frac{1}{\Delta T} = \left(\frac{\theta_{ex} - \theta_{st}}{\frac{n_S}{60} \cdot 2\pi} \right)^{-1} \cong \left(\frac{L}{\frac{n_S}{60} \cdot \pi \cdot D} \right)^{-1} \tag{2.11}$$

Zero crossing and as a result, the frequency domain to be excited is widened by decreasing the engagement duration which is possible by either increasing angular speed or decreasing the wall thickness, as given in equation (2.11). However, both actions reduce the amplitude of excitation, especially at lower frequencies. This effect is visible on Figure 2.3. At the zero frequency, force calculation with a 4 [mm] wall cut, which is given in black; has twice the force amplitude of force calculation with a 2 [mm] wall cut, which is given in red. However, zero crossing frequency is

also almost halved. Likewise, increasing the angular speed of the cutting tool from 3000 [rpm] to 6000 [rpm] has the same effect.

Frequency values of harmonics are a function of angular speed, equal to revolution per seconds. Changing angular speed from 3000 [rpm] to 6000 [rpm], moves the harmonic peaks from 50 [Hz] to 100 [Hz]. Changing the wall thickness has no visible effect on harmonics.

2.1.2 Spindle and Work Piece Transfer Functions

Cutting tool and workpiece dynamics are represented with transfer functions in X and Y directions. Cutting tool displacement is represented with $\mathbf{x}_2(t)$ and workpiece displacement is represented with $\mathbf{x}_1(t)$. Total displacement $\mathbf{x}(t)$ is given as equation (2.12).

$$\mathbf{x}(s) = [x(t)\ \ y(t)]^T = \mathbf{x_1}(s) + \mathbf{x_2}(s) \tag{2.12a}$$

$$\mathbf{x_1}(s) = \mathbf{G_1}(s) \cdot \mathbf{F}(s) \tag{2.12b}$$

$$\mathbf{x_2}(s) = \mathbf{G_2}(s) \cdot \mathbf{F}(s) \tag{2.12c}$$

Here, $\mathbf{F}(\mathbf{s})$ is Laplace domain representation of $\mathbf{F}(\mathbf{t})$. Cutting tool transfer function $\mathbf{G_2}(s)$ and workpiece transfer function $\mathbf{G_1}(s)$ are given at equation (2.13). How to obtain FRFs and details of modal analysis applied are explained in following chapters.

$$\mathbf{G_1}(s) = \begin{bmatrix} G_{1,xx} & G_{1,xy} \\ G_{1,yx} & G_{1,yy} \end{bmatrix} \tag{2.13a}$$

$$\mathbf{G_2}(s) = \begin{bmatrix} G_{2,xx} & G_{2,xy} \\ G_{2,yx} & G_{2,yy} \end{bmatrix} \tag{2.13b}$$

2.1.2.1 Tap Test and FRF Calculations

Any suitable experimental method for obtaining FRFs, such as hammers or shakers, can be used for this purpose, as long as a desired excitation at a desired spot in a desired direction can be applied. The excitation method applied here is what is selected according to the equipment available. What is critical in this chapter is that FRFs from both directions with at least two sensors placed at two Cartesian directions should be present because FRFs between forces and vibrations at X and Y directions are desired.

For this thesis, FRFs that are to be used to obtain transfer functions to be used in the simulation are obtained through tap tests applied on both workpiece (representing table) and cutting tool (representing spindle). Tap hitting spots and accelerometer positions are given at Figure 2.4a. By hitting point 2 at X direction and measuring the response at points 1 and 3, FRFs P_2P_1 and P_2P_3 are obtained. Similarly, by hitting point 4 in Y direction and measuring the response at the same accelerometers, FRFs P_4P_1 and P_4P_3 are obtained. P_2P_1 and P_4P_3 represents X and Y direction transfer functions while P_4P_1 and P_2P_3 represents cross relation between X and Y directions.

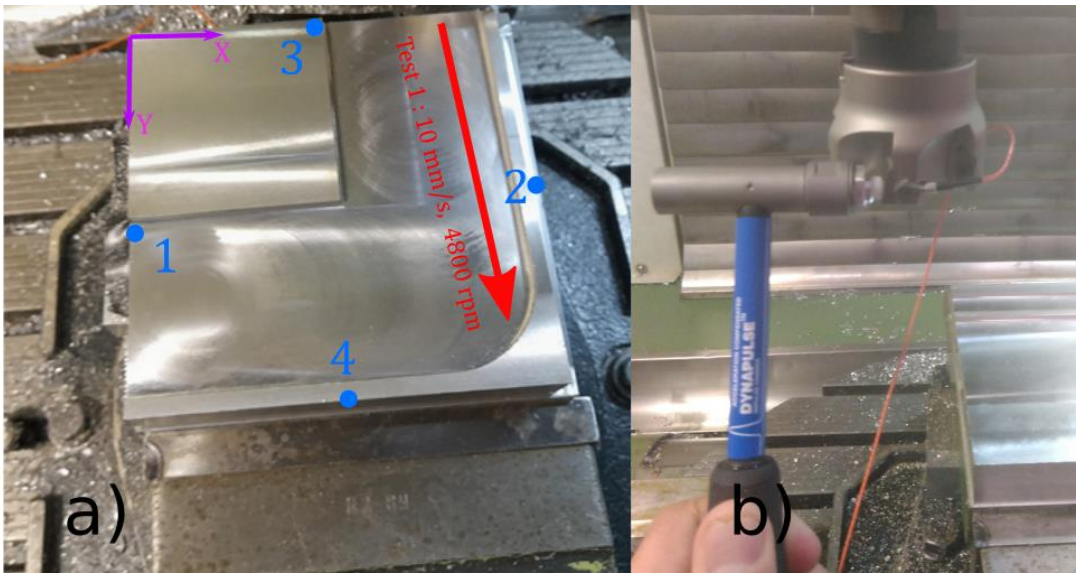

Figure 2.4 a) Work Piece Accelerometer Positions (1-3), Tap Test Tap Spots (2-4) and Test Parameters b) A Representation of Tap Test at Spindle

For spindle, cutting tool to be used during experiments is attached to the spindle and the hammer is hit to the only insert in tangential direction while the response is measured from an accelerometer placed radially and at a 90° distance. This way, the response of tangential force at the same direction is measured. Because spindle is roughly axi-symmetric, a single tap is deemed sufficient and FRF between X and Y directions are not measured. Axi-symmetry is observed from previous tap tests performed at the laboratory. Figure 2.4b gives a description of a hammer test for spindle.

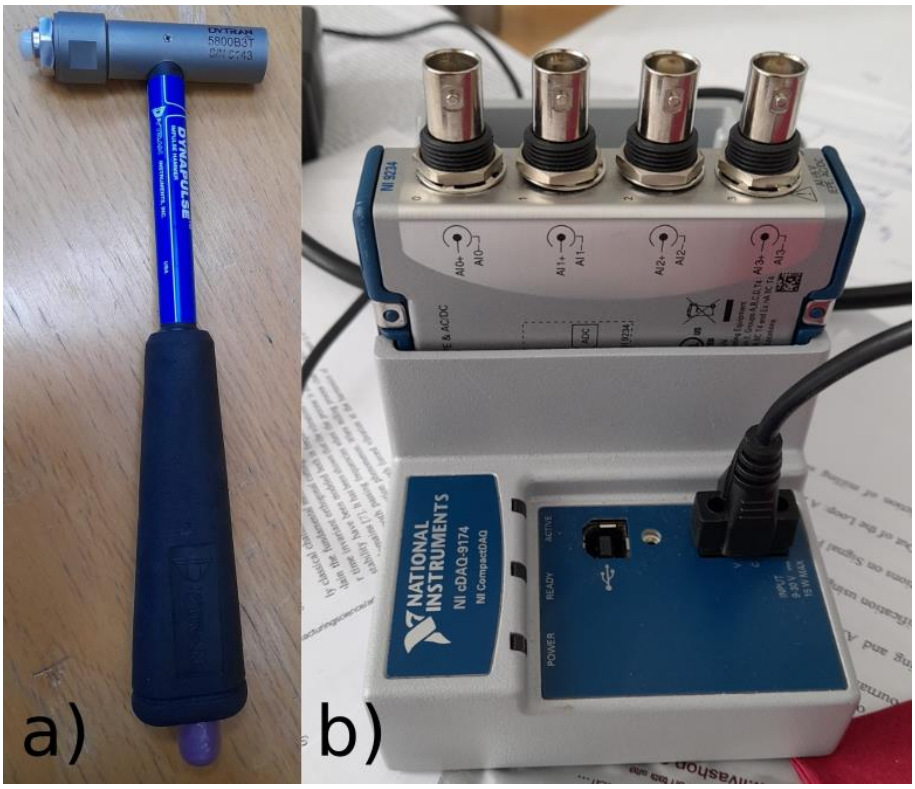

Figure 2.5 a) Hammer Used for Tap Tests. b) NI 9234 Data Acquisition Device Allows 4 BNC Ports That Measures Voltage Difference

As hammer, DYTRAN 5800B3T (Figure 2.5a) and as accelerometers at X and Y directions respectively, PCB 352C23 [5.12mV/g] and DYTRAN 3225F1 [10.23 mV/g] are used. These accelerometers measure at only one direction. For data acquisition, NI 9234 data processing card (Figure 2.5b) is used and the sampling frequency is 51200 [Hz]. This card has 4 BNC ports and takes measurements by

voltage difference obtained by any suitable sensor. This card supports data sampling up to 51200 [Hz] and a voltage difference of 10 [V]. Data is processed with CutPro software.

Two different models that is applied requires different set of transfer functions. MATLAB Simulink model can utilize Laplace Domain transfer functions. Convolution Integral model utilizes Impulse Response Functions (IRF). Figure 2.6, Figure 2.7 and Figure 2.10 provide FRFs and frequency domain representation of transfer functions obtained by them. Figure 2.11 to Figure 2.14 provide IRF's utilized for Convolution Integral model.

2.1.2.1.1 Transfer Functions for MATLAB Simulink Model

Cutpro program is used for modal analysis in this thesis. Tables from Table 2-1 to Table 2-5 give modal parameters obtained by utilizing this program on FRFs obtained. By applying equation (2.14) and modal parameters, transfer functions are found. N gives number of modes selected to construct transfer functions and tables provide number of modes and modal parameters at every mode.

$$G(\omega)_{d,fg} = \sum_{n=1}^{N} \frac{\frac{\omega_n^2}{k_n}}{s^2 + 2\zeta\omega s + \omega_n^2} \quad d \in \{1,2\}, f \in \{x,y\}, g \in \{x,y\} \tag{2.14}$$

Here, k_n gives modal stiffness and ω_n gives mode frequency. ζ gives modal damping. As mentioned at Figure 2.6, Figure 2.7 and Figure 2.10 provide FRFs and frequency domain representation of transfer functions obtained by them. At Figure 2.6, $G_{1,xx}$ and $G_{1,yx}$ gives response of table at X direction by forces applied at X and Y directions as they are constructed from P_2P_1 and P_4P_1 FRFs. Likewise, Figure 2.7 give $G_{1,yy}$ and $G_{1,xy}$ transfer functions as they represent table response at Y direction by forces applied at Y and X directions and they are constructed by P_4P_3 and P_2P_3, all respectively. Finally, Figure 2.10 gives spindle's transfer function at both X and Y directions without a transfer function representing a relation between two

directions. FRF of cutting tool is also given as the FRF used for constructing G_2. Due to axi-symmetry, it is assumed there is no significant transfer function between two directions for cutting tool.

The frequency domain to be analyzed is limited to 300-3000 [Hz]. This is because of two major reasons. At the lower end, force applied is not enough to overcome nonlinearities such as frictions and similar factors to achieve significant coherence at the end result (FRF obtained). At a frequency domain lower than 300 [Hz], coherence values may be lower than 0.5. For higher frequencies, coherence is also low but this is because there is no significant force excitation at such high frequency values due to contact time being too long. Process parameters should be selected according to frequency domain to be analyzed and this is explained in the next chapter with equation (2.18).

By comparing FRFs given at Figure 2.6 and Figure 2.7, it can be observed that the table is more rigid at Y direction compared to X direction. For this reason, the transfer function at XX direction (force at X direction and measurement from X direction) is the dominant transfer function for table. For YX direction, transfer function has significant modes compared to XX direction transfer function at 500-1000 [Hz] and 1500-2000 [Hz] frequency domain (920 and 1750 [Hz], Table 2-9). These mode frequencies are close to XX direction transfer function mode frequencies (896 and 1745 [Hz], Table 2-9). For the frequency where transfer functions representing the relation between two directions (YX) is most dominant, that is 1750 [Hz], the ratio between YX direction transfer function to XX direction transfer function is around 20%. This means that for X direction, the effect of YX direction transfer function should be small if forces at both directions are similar. The situation is different for Y direction as XY direction transfer function is more significant compared to the effect of YX direction transfer function in Y direction. At the frequency domain where the effect of XY direction transfer function is the least significant, the ratio of XY FRF to YY FRF is around 30% and the ratio is higher for transfer functions. At frequency domain around 1700 [Hz], XY direction transfer function is bigger than YY counterpart.

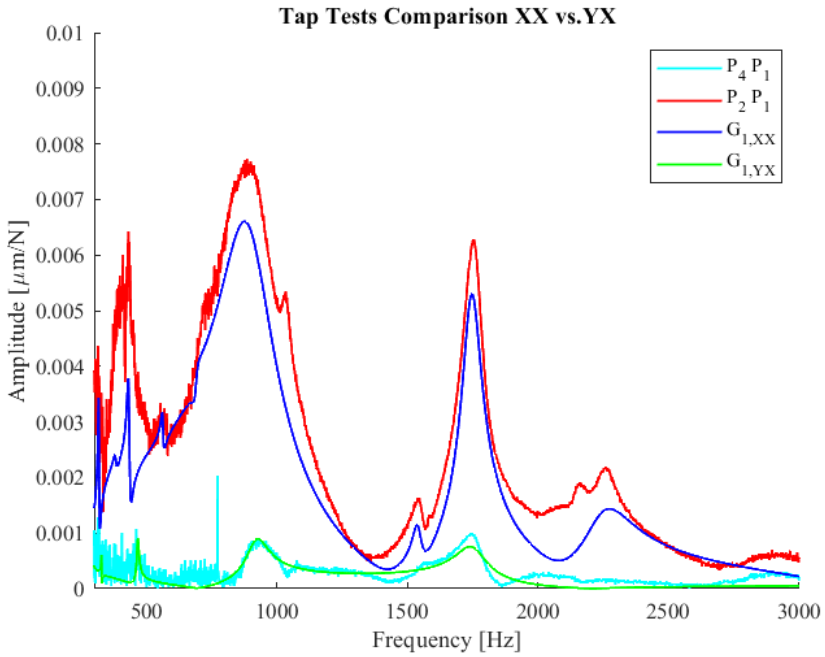

Figure 2.6 Tap Test Comparison with Modal Analysis Outputs, Table (Workpiece) XX vs. YX

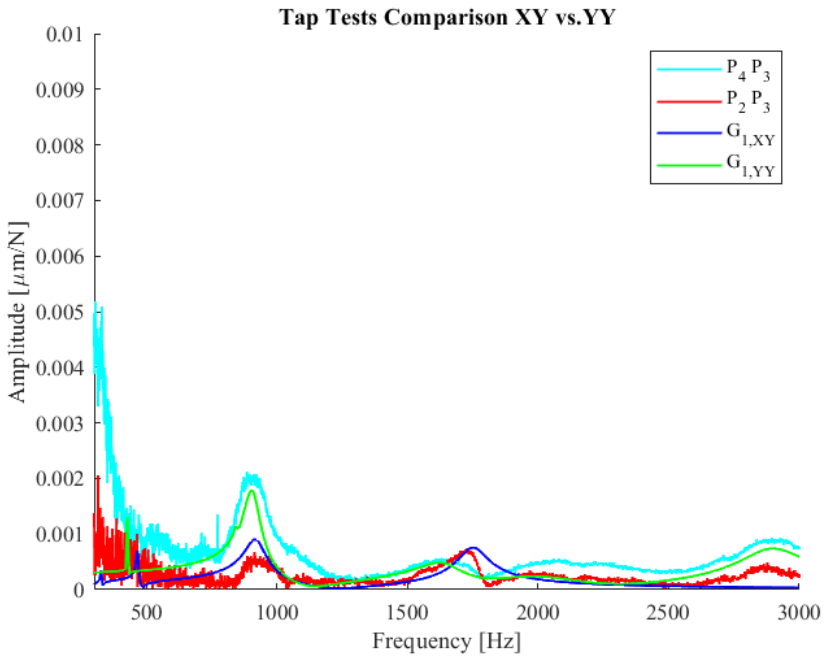

Figure 2.7 Tap Test Comparison with Modal Analysis Outputs, Table (Workpiece) XY vs. YY

Coherence values for two selected tests are given at Figure 2.8 and Figure 2.9. Figure 2.8 gives coherence of P_2P_1 (XX direction transfer function is constructed from) and Figure 2.9 gives coherence of P_2P_3 (XY direction transfer function is constructed from). P_2P_1 gives reliable coherence values but P_2P_3 is only reliable at some selected frequency domain values.

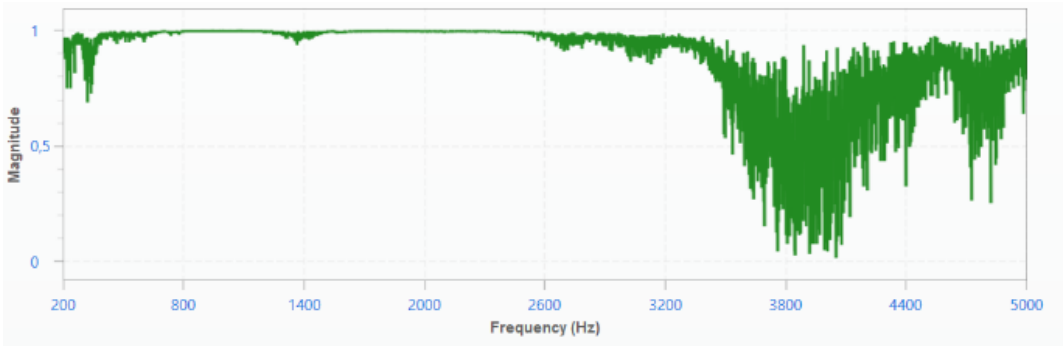

Figure 2.8 Coherence Graphs for Tap Test Comparison XX (P_2P_1)

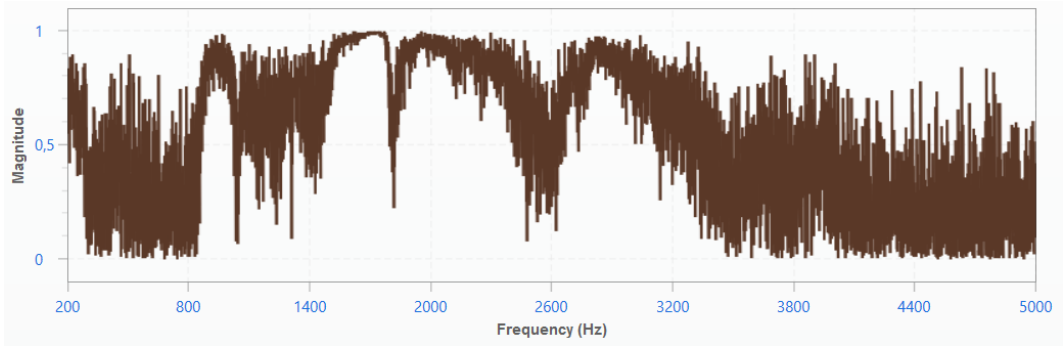

Figure 2.9 Coherence Graphs for Tap Test Comparison XY (P_2P_3)

Finally, cutting tool transfer function is 10 to 100 times bigger than table transfer functions as spindle is significantly less rigid compared to the table.

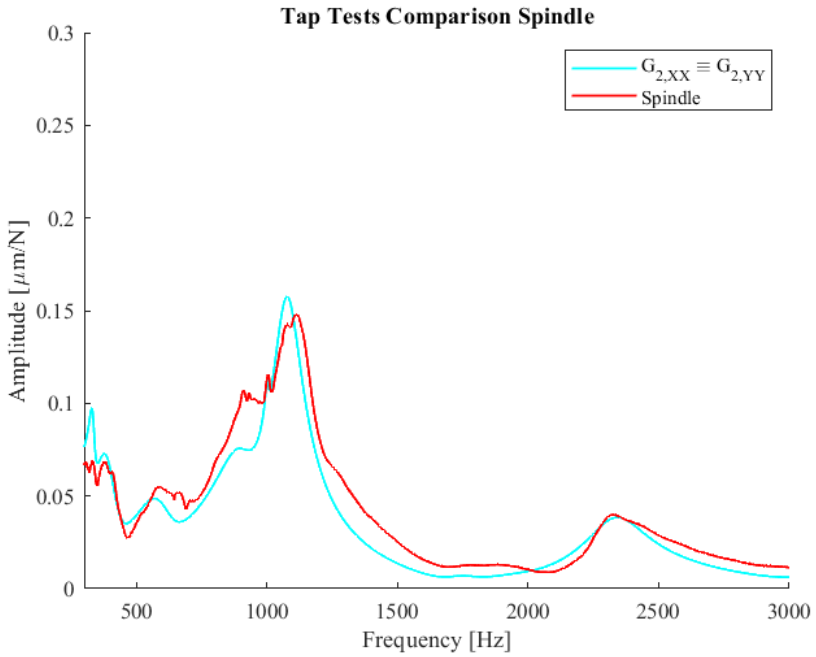

Figure 2.10 Tap Test Comparison with Modal Analysis Output, Spindle

Table 2-1:Modal Parameters of Spindle (Applicable to Both Directions)

Mode	$\omega_n/2\pi$ [Hz]	ξ	k_n [N/m]
1	335.21	5.40e-3	6.09e7
2	396.03	1.85e-2	1.40e7
3	598.73	2.01e-2	2.49e7
4	906.41	1.45e-2	2.41e7
5	1002.41	1.30e-3	5.20e8
6	1078.01	8.70e-3	9.69e6
7	1744.95	7.60e-3	7.11e8
8	1955.62	1.44e-2	3.26e8
9	2336.14	8.30e-3	4.10e7

Table 2-2: XX Modal Parameters for Table

Mode	$\omega_n/2\pi$ [Hz]	ξ	k_n [N/m]
1	286.93	3.60e-3	9.48e8
2	317.87	1.00 e-3	5.25e9
3	383.02	2.50 e-3	1.59e10
4	432.92	1.70 e-3	3.13e9
5	563.05	1.20 e-3	1.45e10
6	689.47	2.50 e-3	9.44e9
7	896.06	1.93 e-2	1.01e8
8	1540.19	1.80 e-3	9.91e9
9	1745.57	3.40 e-3	7.20e8
10	2248.17	6.90 e-3	1.51e9
11	3370.89	4.20 e-3	3.59e9

Table 2-3: YY Modal Parameters for Table

Mode	$\omega_n/2\pi$ [Hz]	ξ	k_n [N/m]
1	427.04	3.15e-5	9.41e10
2	846.03	9.30e-4	7.01e10
3	889.62	5.17e-5	2.28e12
4	907.48	5.90e-3	1.21e9
5	1643.18	9.10e-3	3.50e9
6	2010.65	1.53e-2	4.20e9
7	2896.82	7.20e-3	2.39e9
8	3610.77	1.80e-3	3.48e10

Table 2-4: XY Modal Parameters for Table

Mode	$\omega_n/2\pi$ [Hz]	ξ	k_n [N/m]
1	205.13	1.59e-4	6.23e10
2	917.61	3.20e-3	4.43e9
3	1706.37	4.70e-3	3.75e9
4	2855.61	8.20e-3	3.23e9

Table 2-5: YX Modal Parameters for Table

Mode	$\omega_n/2\pi$ [Hz]	ξ	k_n [N/m]
1	232.46	3.52e-4	2.58e10
2	250.59	4.30e-5	1.61e11
3	270.43	1.07e-4	1.42e11
4	290.05	1.30e-3	2.60e10
5	328.16	2.78e-4	7.86e10
6	467.12	1.30e-3	1.38e10
7	920.77	7.40e-3	1.93e9
8	1750.24	5.50e-3	3.07e9

2.1.2.1.2 Transfer Functions of Convolution Integral Model

Obtaining IRF's can be done quickly by readily available functions. MATLAB IFFT function [42] is used on FRFs shown at Figure 2.6 and Figure 2.7. One important point is that only the selected frequency domain is used for obtaining IRFs. Values of FRFs at other frequencies are taken as zero.

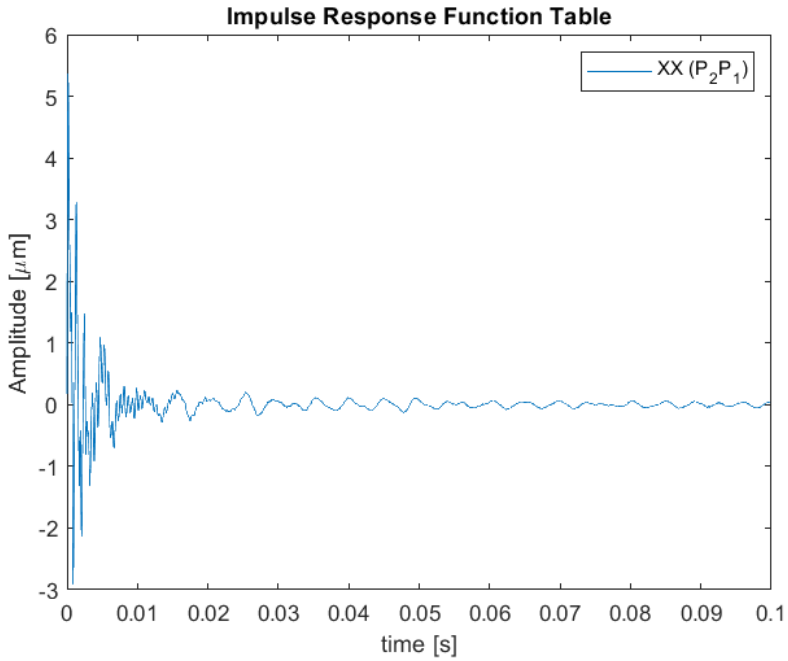

Figure 2.11 Impulse Response Function of (P_2P_1)

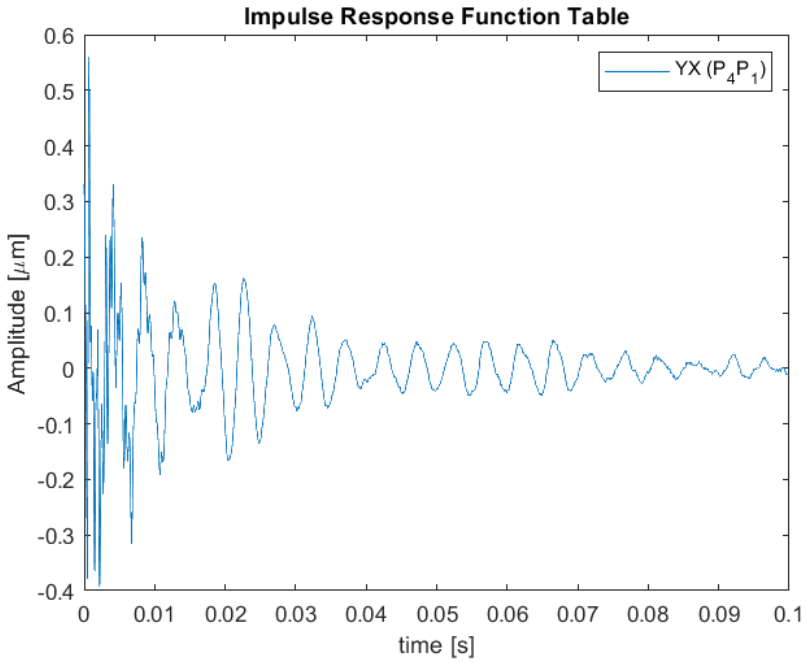

Figure 2.12 Impulse Response Function of (P_4P_1)

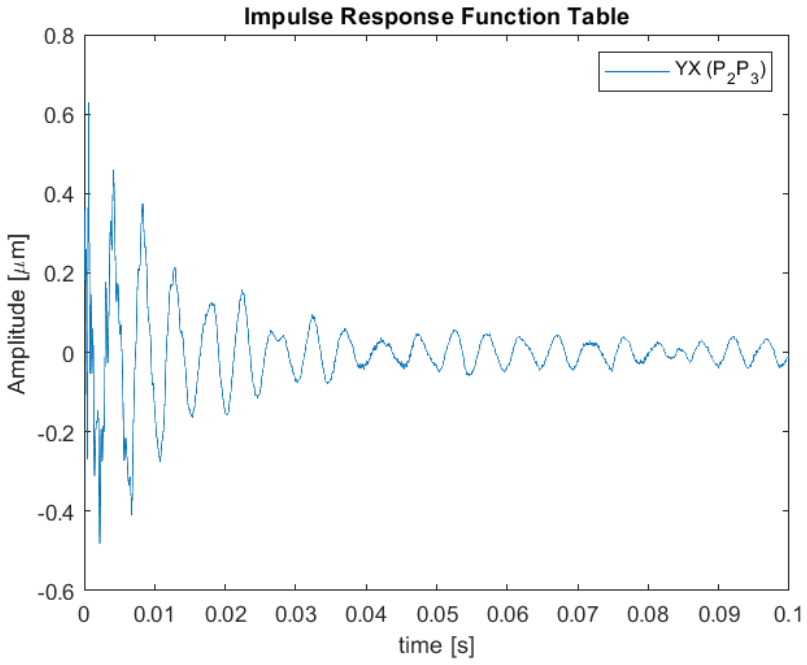

Figure 2.13 Impulse Response Function of (P_2P_3)

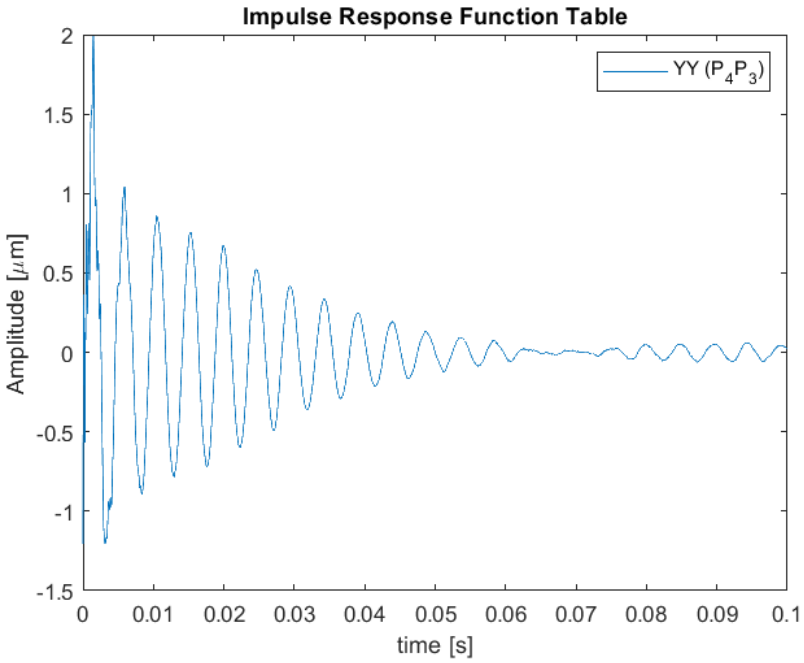

Figure 2.14 Impulse Response Function of (P_4P_3)

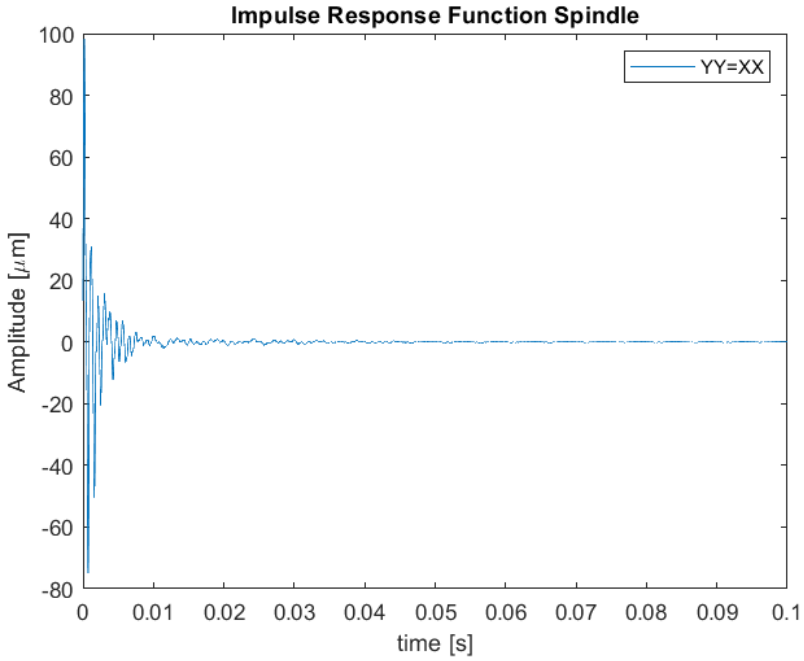

Figure 2.15 Impulse Response Function of Spindle

2.1.3 Merging Models of Force Calculation and Transfer Functions

Block diagram representation of milling process is given at Figure 2.16. Dynamic chip regeneration is represented with feedback. By multiplying chip regeneration with force coefficients and transformation to Cartesian coordinates, $\mathbf{F_d}(\mathbf{s})$ can be calculated. $\mathbf{F_s}(\mathbf{s})$ is consist of two parts. One of them depends on feed per insert, angular position of cutting tool and cutting force coefficients while the other one depends on edge force coefficients and does not depend on chip thickness. Physically, cutting force is a function of chip thickness but for numerical simplicity, it is not calculated in the model and instead, $\mathbf{F_d}(\mathbf{s})$ and $\mathbf{F_s}(\mathbf{s})$ are calculated seperately.

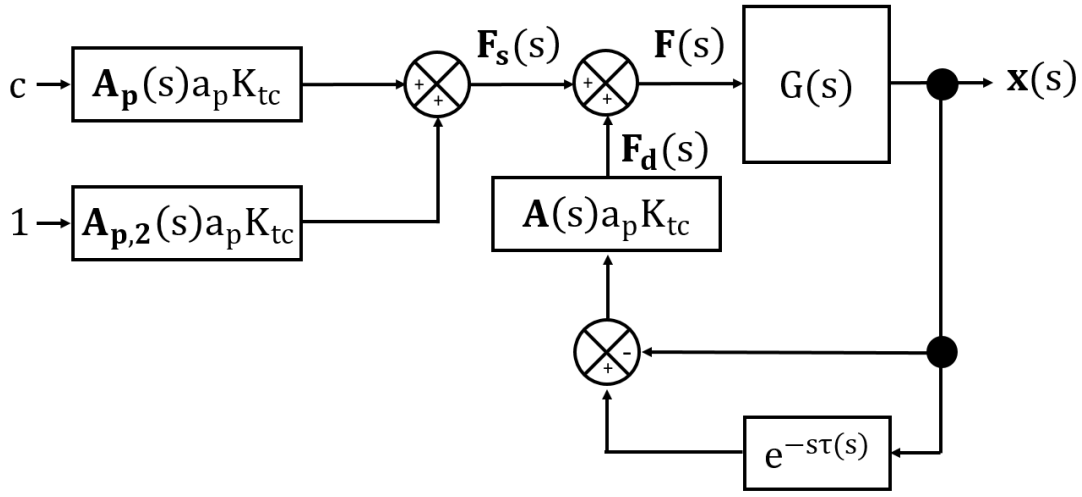

Figure 2.16 Milling Dynamics, Representation of Chip Regeneration

Here, $\mathbf{A}(s)$, $\mathbf{A_p}(s)$ and $\mathbf{A_{p,2}}(s)$ are Laplace domain transformation of $\mathbf{A}(t)$, $\mathbf{A_p}(t)$ and $\mathbf{A_{p,2}}(t)$.

2.2 Simulation Model

Two different approaches have been developed consecutively. The first approach is utilizing MATLAB Simulink. This program offers the advantage of providing off-the-shelf numerical solvers for differential equations and programming is relatively

easy for the simulation of dynamic systems. However, several practical problems has appeared and an alternative approach of convolution integral has been developed for addressing these problems. These problems are mentioned in sections 2.2.2 and 2.3.

2.2.1 MATLAB Simulink Model

Simulation of the entire process is constructed in MATLAB Simulink as shown in Figure 2.17. On the left side force coefficients $(K_{tc}, K_{te}, K_{rc}, K_{re})$, axial depth (a_p), feed per insert (c), $\theta_1(\theta_{st})$ ve $\theta_2(\theta_{ex})$ start and exit angles are given as process parameters. Angular speed of the cutting tool is taken as constant and angular position of cutting tool is calculated with Simulink clock. Window function is performed with "Interval Test" block. At the bottom, a group of blocks representing chip thickness feedback is provided. Constant delay blocks are utilized for delay τ as angular speed of cutting tool is taken as constant. Because there is only one insert, τ is equal to time passed during one turn of the cutting tool. "Chip_Thickness" block given at the very bottom of Figure 2.17 calculates chip thickness given at equation (2.3) with vibrations at X and Y directions.

$G(s)$ subsystem block given at the right side of Figure 2.17 involves transfer functions of workpiece and cutting tool. This subsystem is visible on Figure 2.18. Here, 6 transfer functions of 8 that are given at equation (2.13) are used as for spindle, $G_{2,xy}(s)$ and $G_{2,yx}(s)$ are not used.

For the numerical solver, time step is taken as constant (fixed-step, model settings). ODE solver is picked by Simulink automatically. Time step is a function of angular speed of cutting tool and is given as equation (2.15):

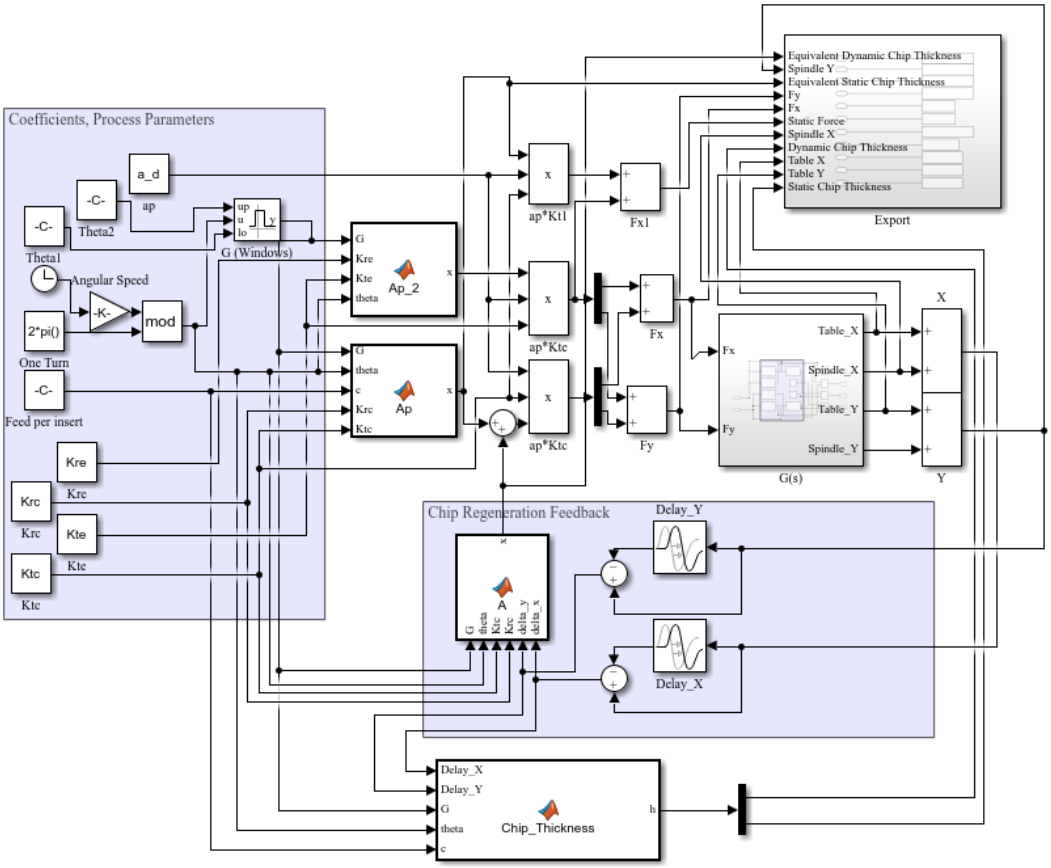

Figure 2.17 Developed Simulink Model

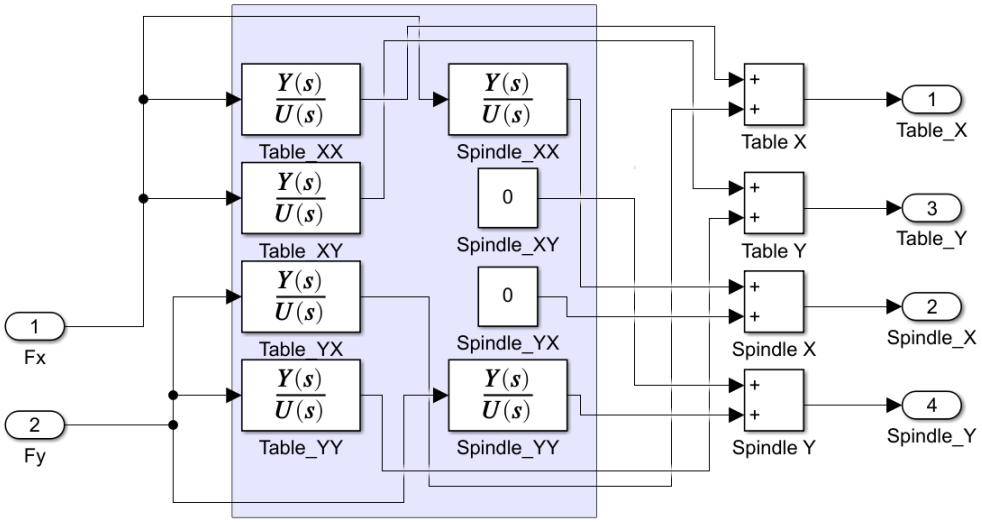

Figure 2.18 G(s) Subsystem of the Developed Simulink Model

$$\Delta T_{sim} = \frac{60}{|n_S|} \cdot \frac{1}{P} \tag{2.15}$$

Here, P gives data points per one turn of cutting tool and is taken as 1000 for this study.

2.2.2 Convolution Integral Model

MATLAB Simulink Model suggested above has several problems as:

1. MATLAB Simulink models utilize time-step solvers. This means that models must be programmed in a way to utilize time-step solvers. This is a limitation compared to a programming language. In this thesis, in order to apply FRFs into MATLAB Simulink model, Laplace domain transfer functions are utilized. In order to obtain transfer functions, Modal Analysis is applied. Modal Analysis requires additional time from researchers. Moreover, it introduces additional uncertainty.
2. MATLAB Simulink does not utilize transfer functions with complex numbers. This means that phase information is lost by utilizing equation (2.14).

The second problem is not a major problem unless dynamic chip thickness becomes significant. The first problem has turned out to be significant during the verification process in Section 2.3.

Alternatively, for cases where modal analysis does not reflect the behavior desirably, a simulation model based on Convolution Integral may be utilized Total chip thickness given in equation (2.3) utilize displacements in Cartesian directions. These displacements are a function of transfer functions. This is where Convolution Integral can be utilized as equation (2.16).

$$\mathbf{x_1}(t) = \begin{bmatrix} x_1(t) \\ y_1(t) \end{bmatrix} = \int_0^t \begin{bmatrix} g_{1,xx}(t-\tau) & g_{1,xy}(t-\tau) \\ g_{1,yx}(t-\tau) & g_{1,yy}(t-\tau) \end{bmatrix} \begin{bmatrix} F_x(t) \\ F_y(t) \end{bmatrix} d\tau \tag{2.16}$$

Here, $g_{1,xx}(t)$ is time domain IRF that can be obtained by IFFT from P_2P_1, XX direction table FRF. Only the frequency domain included for identification purposes is utilized to obtain IRFs.

Utilizing this equation removes the model from MATLAB Simulink in which tools of MATLAB Simulink cannot be used and it makes the calculation significantly slower. In exchange, it removes errors caused by modal analysis and loss of phase information by the MATLAB Simulink model.

Equation (2.16) can be programmed as a summation of discrete arrays as equation (2.17a). This equation addresses time constraints. M is a limit number of array size. $M \cdot \Delta T_{sim}$ indicates past time duration to be included into the calculation. For example, if $M \cdot \Delta T_{sim}$ is equal to 0.1 seconds, only the data from the current time to 0.1 seconds previous is included into the calculation. Equation (2.17c) explains how to obtain M. IRFs dampens out after $M \cdot \Delta T_{sim}$ seconds and so summation after this time is insignificant. In addition, time intervals where force excitation is zero is also omitted as they add zero into the calculation.

$$\mathbf{x_1}(E \cdot \Delta T_{sim}) = \begin{bmatrix} x_1(E \cdot \Delta T_{sim}) \\ y_1(E \cdot \Delta T_{sim}) \end{bmatrix} \cong \sum_{i \in I} \begin{bmatrix} g_{1,xx}(i \cdot \Delta T_{sim}) & g_{1,xy}(i \cdot \Delta T_{sim}) \\ g_{1,yx}(i \cdot \Delta T_{sim}) & g_{1,yy}(i \cdot \Delta T_{sim}) \end{bmatrix} \cdot \begin{bmatrix} F_x((E-i) \cdot \Delta T_{sim}) \\ F_y((E-i) \cdot \Delta T_{sim}) \end{bmatrix} \cdot \Delta T_{sim} \tag{2.17a}$$

$$\begin{bmatrix} g_{1,xx}((M) \cdot \Delta T_{sim}) & g_{1,xy}((M) \cdot \Delta T_{sim}) \\ g_{1,yx}((M) \cdot \Delta T_{sim}) & g_{1,yy}((M) \cdot \Delta T_{sim}) \end{bmatrix} \approx \mathbf{0} \tag{2.17b}$$

$$I = \{i \in N | i \geq \max(E - M, 0), i \leq \mathbf{E}, \mathbf{F}(i \cdot \Delta T_{sim}) \neq \mathbf{0}\} \tag{2.17c}$$

Here, set I gives indexes to include in the equation as equation (2.17c).

2.3 Model Validation

Confirmation of the model is done with a cutting test. Cutting tests are performed on Deckel FP 5CC CNC machine. This milling machine is retrofitted in our laboratory

and it has Beckhoff motor drivers and CNC controllers. The workpiece and cutting tool to be used in tests are shown in Figure 2.4. A thin walled workpiece that is 5 [mm] thickness and 4 [mm] depth is cut in X direction with 2.9 [mm] axial depth and accelerations are measured from points 1 and 3. Wall depth is kept small for preventing wall bending. Acceleration measurements are compared with acceleration estimations obtained from the model with the same process parameters and the model is confirmed. Material selected is AL7075, being a hardened aluminium type used in aerospace applications. Process parameters are given at Table 2-6.

Process parameters are selected according to the frequency domain where the coherence of FRFs are reliable. (300-3000 [Hz] as mentioned in the previous chapter) Cutting tool has one insert and as shown in Figure 2.1, angular speed of cutting tool, feed and start-exit angles of cutting tool during the test (i.e. wall thickness and offset from the center point) are constant.

Given these conditions, the frequency value where excitation amplitude takes the smallest value, zero crossing, can be calculated with equation (2.11). The calculation is shown in equation (2.18). As it can be seen, zero crossing is at 3181 [Hz] with given process parameters which is lower than 3500 [Hz] where tap tests are somewhat reliable. In this equation, ΔT gives time passed during operation and L gives wall thickness.

Table 2-6: Experiment and Models' Process Parameters For Model Verification

Cutting Tool	Diameter 63.3 [mm] , Single Insert
Angular Speed of cutting tool (n_s)	4800 [rpm]
Axial Depth (a_p)	2.9 [mm]
Wall Thickness (L)	5 [mm]
Entry-Exit Angles	Centered Workpiece (Figure 2.2)
Feed	V_x=10 [mm/s] V_y =0
Material	AL7075

$$f_{zc} = \frac{1}{\Delta T} \cong \left(\frac{L}{\frac{n_S}{60} \cdot \pi \cdot D} \right)^{-1} \cong 3181 \text{ [Hz]} \quad (2.18)$$

Start and exit angles can be calculated as below:

$$\theta_{ex} = \frac{\pi}{2} - \sin^{-1}\left(\frac{-L/2}{D/2}\right) = 94.53° \quad \theta_{st} = \frac{\pi}{2} - \sin^{-1}\left(\frac{L/2}{D/2}\right) = 85.46°$$

Workpiece is made of AL 7075 aluminium and cutting coefficients are given at Table 2-7. The method of identification of force coefficients is given at Chapter 3 and the results are from Chapter 5.

Table 2-7: Force Coefficients (Model Input)

K_{tc}=603 [MPa]	K_{rc}=244.10 [MPa]
K_{te}=28.15 [kN/m]	K_{re}=20.08 [kN/m]

Figure 2.19 and Figure 2.20 give Simulink force outputs at X and Y directions respectively and in the frequency domain. Peaks (local maximums) give harmonics and they are integer multiplications of roll per second of the cutting tool that is 80 [Hz]. The frequency content of forces are consistent with equation (2.18) as amplitude of the force is reducing while the frequency of the force is getting closer to the zero crossing frequency. Figure 2.21 gives static force (force caused by static chip thickness) and this graph allows to observe effects of force coefficients and start-exit angles; such as the amplitude of force during contact changes with angular position of cutting tool and contact time are functions of these angles. Amplitude of force is also a function of force coefficients as it can be observed in the figure. In addition, chip thickness obtained from simulation is given at Figure 2.22. As it can be seen, dynamic chip thickness disappears quickly and after 15 [ms], it is insignificant. After this point, calculations performed only with static chip thickness can be considered as total force. This finding is very critical as this clearly shows that dynamic chip thickness can be omitted at certain conditions.

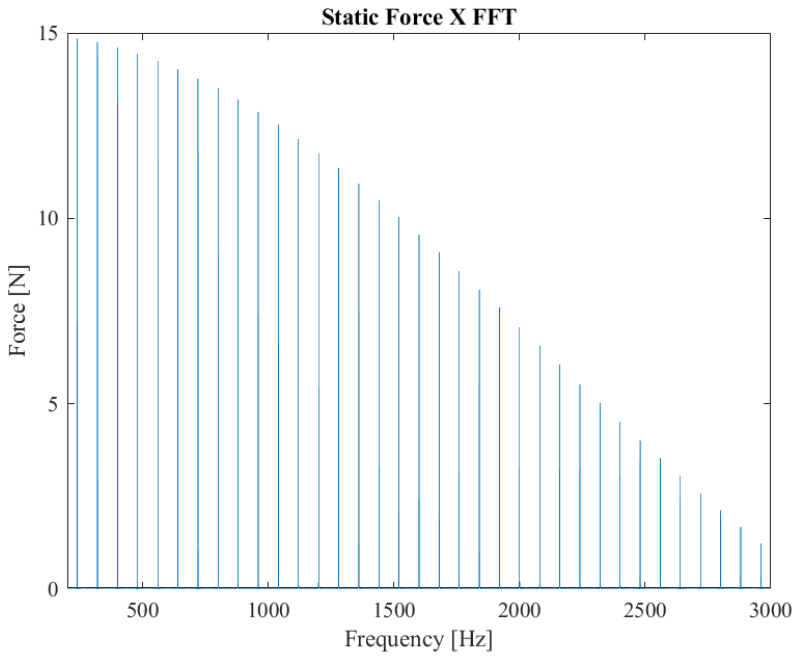

Figure 2.19 Frequency Domain Representation of Static Force in X Direction (MATLAB Simulink)

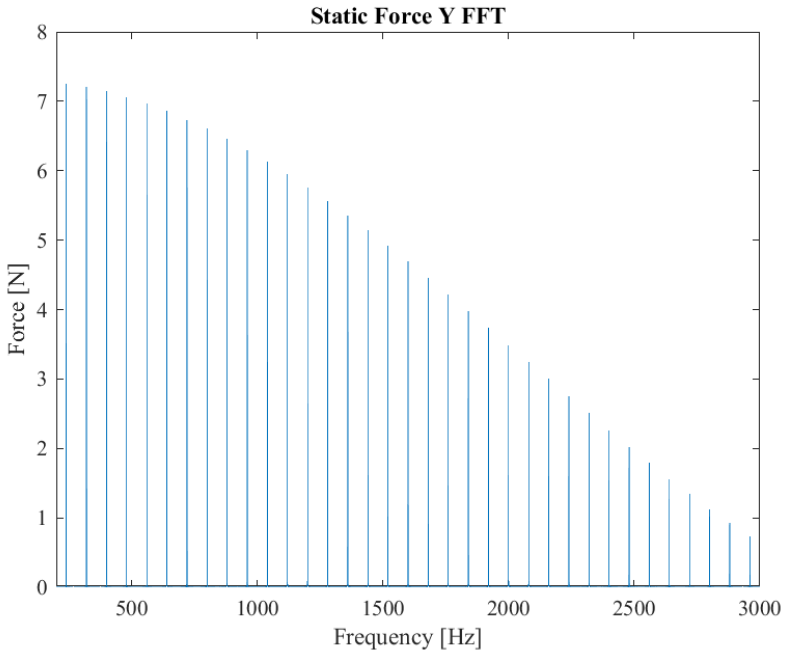

Figure 2.20 Frequency Domain Representation of Static Force in Y Direction (MATLAB Simulink)

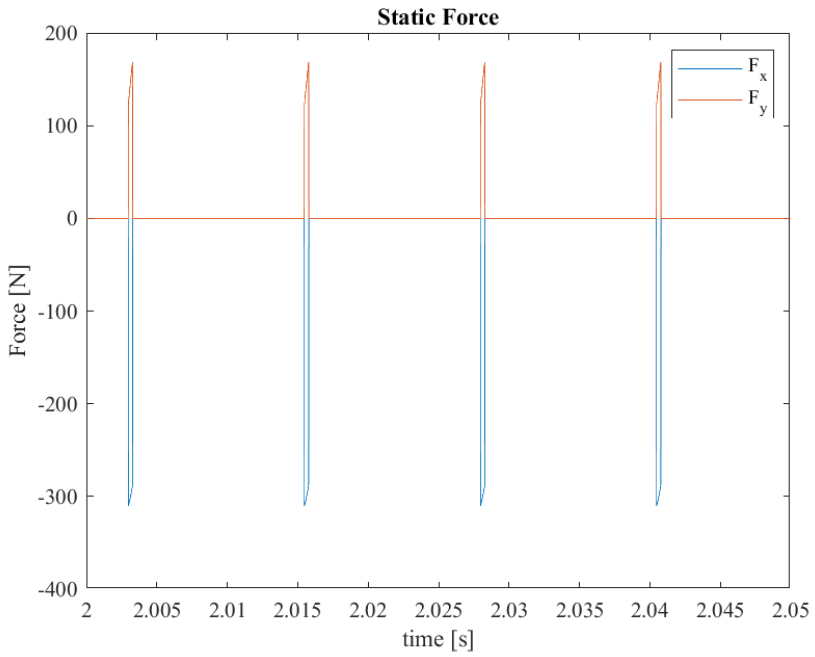

Figure 2.21 Static Forces in Both Directions (MATLAB Simulink)

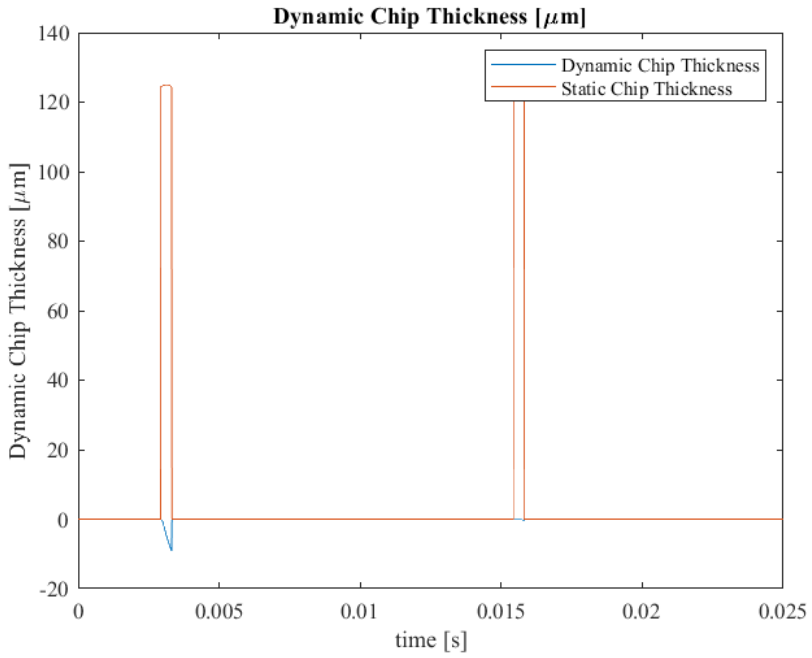

Figure 2.22 Dynamic Chip Regeneration (MATLAB Simulink)

To confirm the model, acceleration measurements are taken during the experiment as accelerometers are placed on points 1 and 3 as shown in Figure 2.4. These acceleration measurements are compared to Simulink acceleration estimations.

Comparison of acceleration is performed at frequency domain. There are several reasons for this selection over comparison at time domain. First of all, vibrations are mostly consist of harmonics and it is easier to compare harmonics at frequency domain. Moreover, not the entirety of frequency domain is used so direct comparison is not possible without filtering. In addition, even small changes like phase shift may cause drastic change in time domain. For those reasons, data and estimations are transferred to frequency domain and model outputs are converted from displacement to acceleration in frequency domain by multiplying with square of frequency in unit of radians. Harmonics with largest local amplitudes are expected to be close to mods of transfer functions as forces are distributed fairly evenly. Comparison is given at the figures below.

For the X direction, as it can be seen at Figure 2.23, experimental acceleration is consistent with both MATLAB Simulink and Convolution Integral model acceleration outputs. To prevent confusion, only harmonics of MATLAB Simulink and Convolution Integral's models' acceleration output are drawn. The highest acceleration value models' acceleration output and experimental value, both in X direction, is observed at 1760 [Hz] and their amplitudes are 4.82 [m/s^2], 4.64 [m/s^2], 5.7 [m/s^2] respectively (The Convolution Integral and then MATLAB Simulink). In addition, peak values are observed at 880 [Hz] and 2240-2320 [Hz]. Checking at Table 2-9, modes 7 and 10 are close. Aside from frequency domain near 2000 [Hz], Simulink output and experimental values are close at or around $\pm 20\%$ and they resembles the character of $G_{1,xx}(i\omega)$. Looking at Figure 2.6, the largest cause of difference is modal analysis and convolution partially helps. Moreover, for frequency domain lower than 500 [Hz], coherence values are too low. Numerical comparisons can be done with Table 2-9 and Table 2-10.

Figure 2.24 gives a comparison for Y direction. Experiment acceleration measurements in Y direction and Simulink acceleration output in Y direction are significantly worse compared to X direction. Convolution Integral is significantly more accurate compared to Simulink for Y direction. This indicates that most of this problem is caused by modal analysis but this is not the only cause of error. Rigidity of Y direction significantly higher it can be seen by comparing Figure 2.7 and Figure 2.6. Results of this situation can be seen by comparing Figure 2.24 (Y direction) and Figure 2.23 (X direction). Highest acceleration value of Y direction for Simulink output is at 1680 [Hz] with 0.54 [m/s^2] and for experiment at 1760 [Hz] with 0.50 [m/s^2] amplitude. Convolution Integral model gives peak at 1680 [Hz] with 0.50 [m/s^2]. High rigidity requires higher force excitation for overcoming nonlinearities and noise factors and this problem is visible with coherence calculations. Moreover, force at X direction is significant at response in Y direction. In summary, in addition to problems observed at X direction; Y direction has poor coherence issues and Y direction acceleration response is significantly affected by X direction force. Removing modal analysis helps partially regarding these problems.

Given amplitude ratios are applicable for data points (or selected frequency values, as in a single acceleration value comparison at the selected frequency), an error indicator for the entire frequency domain selected is desirable. For a comparison based on harmonics, only the harmonics of angular speed of cutting tool that are present at the selected frequency domain can be utilized. In short, all harmonics given at the table can be used for a single error indicator, as called “Batch-Size” in Table 2-8: Batch-Size Error Criteria Calculations. For additional error indicators, Root Mean Square Error (RMSE) and Symmetric Mean Absolute Percentage Error (SMAPE). Calculation of error criterias are explained at equations (2.19) and (2.20).

$$\mathrm{RMSD} = \sqrt{\frac{1}{T}\sum_{t=1}^{T}\left(\widehat{X}(\omega_t) - X(\omega_t)\right)^2} \tag{2.19}$$

$$\text{SMAPE} = \frac{1}{T}\sum_{t=1}^{T}\frac{\left|\widehat{X}(\omega_t) - X(\omega_t)\right|}{\left|\widehat{X}(\omega_t)\right| + |X(\omega_t)|} \tag{2.20}$$

Checking at table Table 2-8, different than the expected result, MATLAB Simulink model provides better estimation for X direction but the difference is insignificant. Estimations of X direction is worse in terms of absolute error that can be observed better with RMSD but SMAPE estimations are significantly better for X direction for both models. For Y direction, the Convolution Integral has provided significantly better outcome both error criterias.

As a result, there are several key points to be taken. The largest source of error is utilizing FRFs with poor coherence. Equipment to be used for tap tests is critically dependent to the frequency domain to be analyzed. Process parameters to be selected should be adjusted to the frequency domain to be analyzed. Modal analysis quality must be sufficient and if not, convolution integral should be utilized. There is no major source of error observed from the process model as long as process parameters are selected correctly and modal analysis is handled well.

Table 2-8: Batch-Size Error Criteria Calculations, Acceleration Outputs Compared to Experimental Data

	RMSD	**SMAPE**
Convolution X	0.4410	0.3572
Convolution Y	0.1030	0.4463
Simulink X	0.3584	0.2680
Simulink Y	0.1668	0.9827

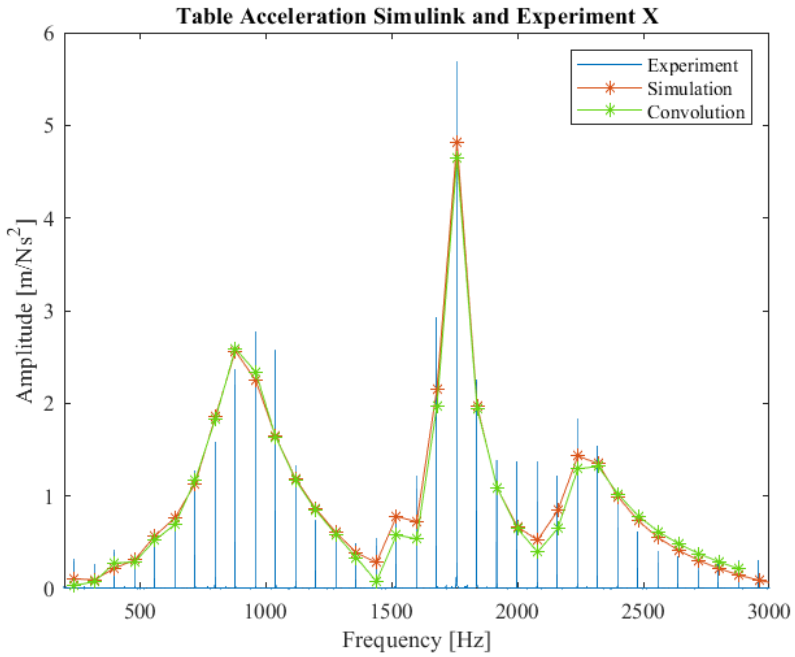

Figure 2.23 Experimental Acceleration in the X Direction Compared to Acceleration Estimation Obtained Through Simulink

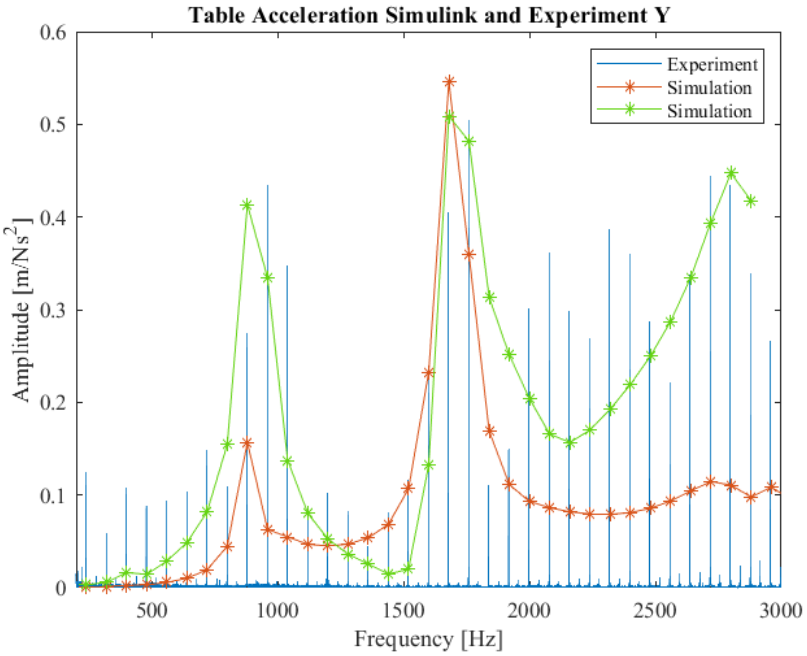

Figure 2.24 Experimental Acceleration in the Y Direction Compared to Acceleration Estimation Obtained Through Simulink

Table 2-9: Comparison of X and Y Direction Accelerations by Harmonics.
(Ratios of Harmonics Are That of Convolution to Experiment)

Frequency [Hz]	Simulink Acceleration Output X	Experiment Acceleration Output X	Simulink Acceleration Output Y	Experiment Acceleration Output Y	Amplitude Ratio X	Amplitude Ratio Y
240	0.0355	0.3222	0.0030	0.1248	0.1104	0.0246
320	0.0732	0.2632	0.0056	0.0591	0.2784	0.0961
400	0.2766	0.4221	0.0162	0.1082	0.6552	0.1503
480	0.2871	0.3591	0.0142	0.0886	0.7994	0.1614
560	0.5228	0.4830	0.0286	0.0931	1.0824	0.3077
640	0.6928	0.6742	0.0486	0.1031	1.0277	0.4720
720	1.1703	1.2675	0.0817	0.1482	0.9233	0.5515
800	1.8295	1.5847	0.1543	0.1084	1.1545	1.4233
880	2.5899	2.3586	0.4131	0.2747	1.0980	1.5037
960	2.3399	2.7667	0.3343	0.4337	0.8457	0.7709
1040	1.6351	2.5710	0.1373	0.3478	0.6360	0.3949
1120	1.1669	1.3314	0.0802	0.0845	0.8764	0.9489
1200	0.8420	0.7454	0.0524	0.0991	1.1297	0.5143
1280	0.5816	0.6406	0.0361	0.0831	0.9080	0.4347
1360	0.3358	0.4812	0.0253	0.0451	0.6980	0.5622
1440	0.0763	0.5463	0.0146	0.0811	0.1398	0.1806
1520	0.5792	0.8500	0.0199	0.0907	0.6814	0.1717
1600	0.5367	1.2203	0.1325	0.2377	0.4398	0.5574
1680	1.9639	2.9256	0.5088	0.4042	0.6712	1.2590
1760	4.6402	5.6957	0.4817	0.5044	0.8146	0.9550
1840	1.9433	2.2515	0.3133	0.1108	0.8631	2.8267
1920	1.0844	1.3858	0.2510	0.1495	0.7825	1.6789
2000	0.6466	1.3659	0.2039	0.3010	0.4734	0.6778
2080	0.3953	1.3741	0.1658	0.3621	0.2877	0.4580
2160	0.6494	1.2116	0.1566	0.2978	0.5360	0.5258
2240	1.2928	1.8323	0.1699	0.2683	0.7055	0.6336
2320	1.3190	1.5360	0.1923	0.3863	0.8587	0.4979
2400	1.0177	1.0130	0.2188	0.3600	1.0046	0.6079
2480	0.7832	0.6069	0.2497	0.2867	1.2905	0.8710
2560	0.6138	0.4020	0.2870	0.2038	1.5271	1.2942
2640	0.4838	0.3431	0.3344	0.3369	1.4102	0.9925
2720	0.3783	0.3251	0.3939	0.4444	1.1635	0.8863
2800	0.2892	0.2683	0.4473	0.4337	1.0781	1.0315
2880	0.2122	0.3074	0.4175	0.2257	0.6902	1.2309
2960	0.3026	0.3028	0.1223	0.2657	0.9994	1.5760

Table 2-10: Comparison of X and Y Direction Accelerations by Harmonics.
(Ratios of Harmonics Are That of Simulink to Experiment)

Frequency [Hz]	Simulink Acceleration Output X	Experiment Acceleration Output X	Simulink Acceleration Output Y	Experiment Acceleration Output Y	Amplitude Ratio X	Amplitude Ratio Y
240	0.1058	0.3222	0.0008	0.1248	0.3285	0.0063
320	0.0951	0.2632	0.0013	0.0591	0.3614	0.0212
400	0.2214	0.4221	0.0026	0.1082	0.5246	0.0240
480	0.3097	0.3591	0.0030	0.0886	0.8623	0.0340
560	0.5684	0.4830	0.0056	0.0931	1.1768	0.0604
640	0.7650	0.6742	0.0101	0.1031	1.1348	0.0979
720	1.1318	1.2675	0.0193	0.1482	0.8929	0.1302
800	1.8531	1.5847	0.0448	0.1084	1.1694	0.4135
880	2.5640	2.3586	0.1568	0.2747	1.0871	0.5709
960	2.2496	2.7667	0.0631	0.4337	0.8131	0.1454
1040	1.6407	2.5710	0.0546	0.3478	0.6381	0.1569
1120	1.1816	1.3314	0.0468	0.0845	0.8875	0.5542
1200	0.8581	0.7454	0.0450	0.0991	1.1513	0.4537
1280	0.6037	0.6406	0.0471	0.0831	0.9424	0.5666
1360	0.3880	0.4812	0.0536	0.0451	0.8063	1.1897
1440	0.2815	0.5463	0.0685	0.0811	0.5154	0.8445
1520	0.7792	0.8500	0.1068	0.0907	0.9167	1.1770
1600	0.7217	1.2203	0.2327	0.2377	0.5914	0.9791
1680	2.1496	2.9256	0.546	0.4042	0.7347	1.3511
1760	4.8154	5.6957	0.3591	0.5044	0.8454	0.7119
1840	1.9632	2.2515	0.1689	0.1108	0.8719	1.5240
1920	1.0806	1.3858	0.1114	0.1495	0.7797	0.7453
2000	0.6675	1.3659	0.0929	0.3010	0.4887	0.3087
2080	0.5238	1.3741	0.0863	0.3621	0.3812	0.2384
2160	0.8424	1.2116	0.0820	0.2978	0.6953	0.2754
2240	1.4305	1.8323	0.0794	0.2683	0.7807	0.2960
2320	1.3508	1.5360	0.0790	0.3863	0.8794	0.2045
2400	0.9899	1.0130	0.0810	0.3600	0.9773	0.2249
2480	0.7294	0.6069	0.0857	0.2867	1.2020	0.2989
2560	0.5483	0.4020	0.0935	0.2038	1.3641	0.4587
2640	0.4122	0.3431	0.1042	0.3369	1.2015	0.3092
2720	0.3042	0.3251	0.1146	0.4444	0.9359	0.2578
2800	0.2171	0.2683	0.1107	0.4337	0.8092	0.2552
2880	0.1461	0.3074	0.0976	0.2257	0.4753	0.4325
2960	0.0887	0.3028	0.1084	0.2657	0.2929	0.4080

CHAPTER 3

IDENTIFICATION OF FORCE COEFFICIENTS

3.1 Overview

As discussed in Chapter 1.4, obtaining force coefficients through an empirical method that is not relying on direct force measurement is a suitable approach for this thesis. In Chapter 2, it has been shown that dynamic chip thickness can become insignificant under stable process and force can be assumed to be only dependent on static chip thickness. This chapter explains how to obtain force coefficients.

The approach this thesis uses relies on FRFs obtained through tap tests, acceleration measurements taken during a milling process with controlled parameters and the force model. A force estimation is performed utilizing acceleration measurements and FRFs obtained through tap tests. Force calculation is performed with the given model in Chapter 2 and an identification procedure between these two are applied. Chapter 3.1 explains the theory and calculations of force estimation along with how to apply force calculation and force estimation for identification. This chapter also addresses various problems to be solved regarding identification of force coefficients. Chapter 3.2 explains the identification calculations, and Chapter 3.3 exemplifies how to apply the method in practice by showing it in simulation in which the effectiveness of the method is shown.

Starting with force calculation, equation (2.9b) should be written in open format in order to emphasize effects of every force coefficients as in equations from (3.1a) to (3.1d).

$$\mathbf{F_s}(t) = a_p K_{tc} c \frac{1}{2}\begin{bmatrix} a_{xx}(t) \\ a_{yx}(t) \end{bmatrix} + a_p K_{te}\begin{bmatrix} a_{xx,2}(t) \\ a_{yx,2}(t) \end{bmatrix} \tag{3.1a}$$

$$\begin{aligned}\mathbf{F_s}(t) = g(t) a_p \Bigg(& K_{tc} c \frac{1}{2}\begin{bmatrix} -\left[\left(\sin 2\theta(t)\right) + \frac{K_{rc}}{K_{tc}}\left(1 - \cos 2\theta(t)\right)\right] \\ \left[\left(1 - \cos 2\theta(t)\right) - \frac{K_{rc}}{K_{tc}}\sin 2\theta(t)\right] \end{bmatrix} \\ & + K_{te}\begin{bmatrix} -\left[\left(\cos\theta(t)\right) + \frac{K_{re}}{K_{te}}\sin\theta(t)\right] \\ \left[\left(\sin\theta(t)\right) - \frac{K_{re}}{K_{te}}\cos\theta(t)\right] \end{bmatrix}\Bigg)\end{aligned} \tag{3.1b}$$

$$\mathbf{F_s}(t) = g(t) a_p \begin{bmatrix} -c\cos(\theta)\sin(\theta) & -c\sin^2(\theta) & -\cos(\theta) & -\sin(\theta) \\ c\sin^2(\theta) & -c\cos(\theta)\sin(\theta) & \sin(\theta) & -\cos(\theta) \end{bmatrix}\begin{bmatrix} K_{tc} \\ K_{rc} \\ K_{te} \\ K_{re} \end{bmatrix} \tag{3.1c}$$

$$\mathbf{F_s}(t) = \begin{bmatrix} H_{tc,x}(t) & H_{rc,x}(t) & H_{te,x}(t) & H_{re,x}(t) \\ H_{tc,y}(t) & H_{rc,y}(t) & H_{te,y}(t) & H_{re,y}(t) \end{bmatrix}\begin{bmatrix} K_{tc} \\ K_{rc} \\ K_{te} \\ K_{re} \end{bmatrix} \tag{3.1d}$$

Here, $H_{mn,d}(t)$ represents force in d direction caused by K_{mn}. For force estimation, total vibrations in frequency domain can be described as a function of force and FRFs as below:

$$\mathbf{x}(\omega) = \begin{bmatrix} x(\omega) \\ y(\omega) \end{bmatrix} = \cdot \underbrace{\begin{bmatrix} G_{xx}(\omega) & G_{xy}(\omega) \\ G_{yx}(\omega) & G_{yy}(\omega) \end{bmatrix}}_{\mathbf{G}(\omega)} \underbrace{\begin{bmatrix} F_x(\omega) \\ F_y(\omega) \end{bmatrix}}_{\mathbf{F_s}(\omega)} \tag{3.2}$$

$$\hat{\mathbf{F}}_\mathbf{s}(\omega) = \begin{bmatrix} G_{xx}(\omega) & G_{xy}(\omega) \\ G_{yx}(\omega) & G_{yx}(\omega) \end{bmatrix}^{-1}\begin{bmatrix} X(\omega) \\ Y(\omega) \end{bmatrix} \tag{3.3}$$

Here, $\hat{\mathbf{F}}_\mathbf{s}(\omega)$ is the force estimation in frequency domain. This is the data that force calculation is supposed to match by identifying force coefficients as equation (3.4) and (3.5).

$$\hat{\mathbf{F}}_\mathbf{s}(\omega) \cong \mathbf{F_s}(\omega) \tag{3.4}$$

$$\underbrace{\begin{bmatrix} G_{xx}(\omega) & G_{xy}(\omega) \\ G_{yx}(\omega) & G_{yx}(\omega) \end{bmatrix}^{-1}\begin{bmatrix} X(\omega) \\ Y(\omega) \end{bmatrix}}_{\hat{\mathbf{F}}_\mathbf{s}(\omega)} \cong \underbrace{\begin{bmatrix} H_{tc,x}(\omega) & H_{rc,x}(\omega) & H_{te,x}(\omega) & H_{re,x}(\omega) \\ H_{tc,y}(\omega) & H_{rc,y}(\omega) & H_{te,y}(\omega) & H_{re,y}(\omega) \end{bmatrix}}_{\mathbf{H}(\omega)}\begin{bmatrix} K_{tc} \\ K_{rc} \\ K_{te} \\ K_{re} \end{bmatrix} \tag{3.5}$$

Here, $\mathbf{H}(\omega)$ provides set of multipliers for force coefficients in the given set of linear equations.

Equation (3.5) could be used for a least squares method application. However, there are several problems preventing a direct application.

1. As shown in Figure 2.3, Figure 2.19, Figure 2.23 etc…, frequency domain of both acceleration data and force calculation is dominated by harmonics. Moreover, because calculation must be time-synched to the data and there can be shifts of angular speed, feed etc…, direct application of equation (3.5) ends up with a zero accuracy, meaningless result due to dividing by too small numbers during calculation.
2. As mentioned in the introduction, this thesis develops a method for local identification because local variations of FRF is expected. Utilizing entire data in one shot does not serve this purpose.
3. Cross FRFs G_{xy} and G_{yx} are small and their coherence is comparably poor. An option of removing them can be ideal.
4. Contrary to above two points, applying $\mathbf{H}(\omega)$ returns ill-conditioned matrice without accommodations and as a result, it cannot be directly used [Appendix B].

The first and the second problem is handled with utilizing individual cutting tool-workpiece contacts as "engagements." Figure 3.1 illustrates the force and acceleration response of a sampled engagement. As seen from the figure, the cut is equivalent to a single tap test, as it involves one force excitation caused by a single tool-workpiece contact and response in its' entirety until it dampens out. Different from the tap test, here the force is calculated theoretically. Hence its time axis has to be synchronized with the experimentally measured acceleration signal. In order to synchronize the two, an acceleration threshold of 6 [m/s^2] is utilized to place the force date. Note that since the tool has one cutting insert there exists a single excitation in one spindle revolution and the harmonics disappear till the second engagement, as it can be seen from Figure 3.2. However, a single test can offer multiple, even hundreds of engagements sampled at the spot that can be calculated.

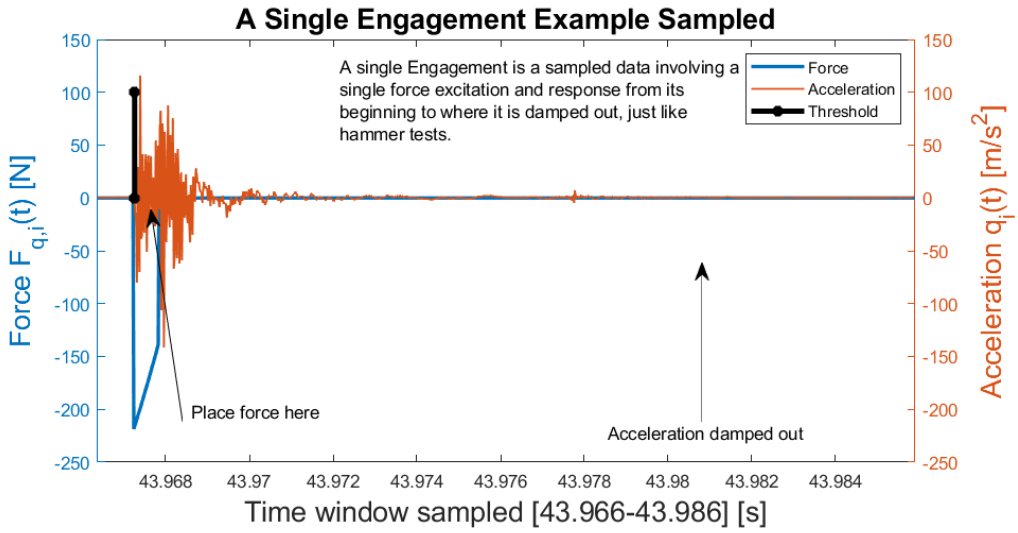

Figure 3.1 A Sampled Engagement Example

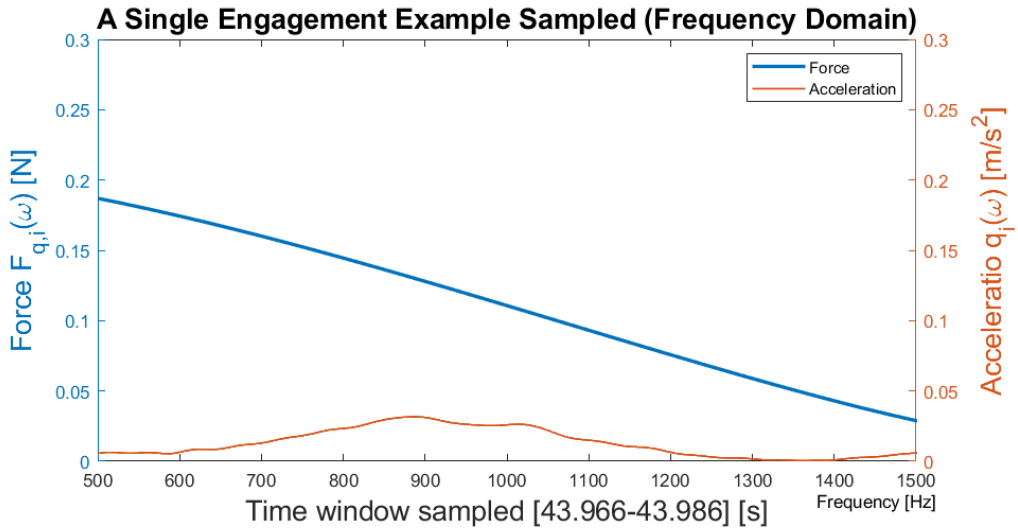

Figure 3.2 A Sampled Engagement Example in Frequency Domain

The third problem is resolved by simply ignoring $G_{xy}(\omega)$ and $G_{yx}(\omega)$ as shown in equation (3.6b) Depending on how major a difference this is, it is expected to a slight under-estimation or force coefficients compared to adding $G_{xy}(\omega)$ and $G_{yx}(\omega)$ into calculation. **Values obtained by not ignoring cross FRF are shown in this thesis as 2D force coefficients' identification as this option can lead to better force coefficients' estimation given in a case when cross FRF cannot be ignored and**

coherence is higher. Together with this knowledge equation (3.5) can be used to obtain equations from (3.6a) to (3.6d).

$$\boldsymbol{\omega}_{n\times 1} = [\omega_1, \omega_2, , \dots, \omega_i, \dots \omega_n]^T \tag{3.6a}$$

$$\hat{\mathbf{F}}_{\mathbf{s}}(\omega_i)_{\mathbf{2}\times 1} = \begin{bmatrix} G_{xx}^{-1}(\omega_i)X(\omega_i) \\ G_{yy}^{-1}(\omega_i)Y(\omega_i) \end{bmatrix} \tag{3.6b}$$

$$\mathbf{H}(\omega_i)_{\mathbf{2}\times 4} = \begin{bmatrix} H_{tc,x}(\omega_i) & H_{rc,x}(\omega_i) & H_{te,x}(\omega_i) & H_{re,x}(\omega_i) \\ H_{tc,y}(\omega_i) & H_{rc,y}(\omega_i) & H_{te,y}(\omega_i) & H_{re,y}(\omega_i) \end{bmatrix} \tag{3.6c}$$

$$\left|\hat{\mathbf{F}}_{\mathbf{s}}(\boldsymbol{\omega})_{2n\times 1}\right| \cong a_p \mathbf{H}(\boldsymbol{\omega})_{2n\times 4} \begin{bmatrix} K_{tc} \\ K_{rc} \\ K_{te} \\ K_{re} \end{bmatrix} \tag{3.6d}$$

H in equation (3.6c) provides set of multipliers for force coefficients in given set of linear equations. **ω** is a set of frequency values sampled and ω_i is one selected frequency.

The fourth problem is resolved by splitting the problem into segments. The first point to figure out is that instead of finding all force coefficients at the same time, force can be approximated by assuming only one of coefficients is non-zero. Starting with representing Cartesian force calculations separately:

$$F_x(\omega, K_{tc}, K_{rc}, K_{te}, K_{re}) = \begin{bmatrix} H_{tc,x}(\omega) & H_{rc,x}(\omega) & H_{te,x}(\omega) & H_{re,x}(\omega) \end{bmatrix} \begin{bmatrix} K_{tc} \\ K_{rc} \\ K_{te} \\ K_{re} \end{bmatrix} \tag{3.7}$$

$$F_y(\omega, K_{tc}, K_{rc}, K_{te}, K_{re}) = \begin{bmatrix} H_{tc,y}(\omega) & H_{rc,y}(\omega) & H_{te,y}(\omega) & H_{re,y}(\omega) \end{bmatrix} \begin{bmatrix} K_{tc} \\ K_{rc} \\ K_{te} \\ K_{re} \end{bmatrix} \tag{3.8}$$

Here, $F_y(\omega, K_{tc}, K_{rc}, K_{te}, K_{re})$ is force calculation in Y direction that is obtained with given force coefficients.

In this step, force calculation can be assumed to be only obtained with a single force coefficient as below:

$$F_x(\omega, K_{tc}, K_{rc}, K_{te}, K_{re}) =$$
$$a_p cH_{tc,x}(\omega)K_{Xtc} = a_p cH_{rc,x}(\omega)K_{Xrc} = a_p H_{te,x}(\omega)K_{Xte} = a_p H_{re,x}(\omega)K_{Xre} \quad (3.9)$$

$$F_y(\omega, K_{tc}, K_{rc}, K_{te}, K_{re}) =$$
$$a_p cH_{tc,y}(\omega)K_{Ytc} = a_p cH_{rc,y}(\omega)K_{Yrc} = a_p H_{te,y}(\omega)K_{Yte} = a_p H_{re,y}(\omega)K_{Yre} \quad (3.10)$$

Such an assumption is not always accurate but that is not necessary. What is desired is to see the effects of force coefficients used as input on the force coefficients obtained with the assumption. In addition, there is a linear relation between force coefficients used as input on force calculation and force coefficients obtained after the assumption. In other words, force coefficients obtained with the assumption are linear function of input force coefficients. *Applying the same principle into **force estimation**, force coefficients obtained with the assumption as the force being represented with only one force coefficient is a linear function of real force coefficients.* This allows equations from (3.11) to (3.16) to be written. By taking force calculation and replacing one force coefficient with 1(one) and the rest zero, assumption ratio matrices $\mathbf{X_{Fmatr}}$ and $\mathbf{Y_{Fmatr}}$ can be obtained.

$$\mathbf{X_{Fmatr}} = \begin{bmatrix} X_{tc_{tc}} & X_{tc_{rc}} & X_{tc_{te}} & X_{tc_{re}} \\ X_{rc_{tc}} & X_{rc_{rc}} & X_{rc_{te}} & X_{rc_{re}} \\ X_{te_{tc}} & X_{te_{rc}} & X_{te_{te}} & X_{te_{re}} \\ X_{re_{tc}} & X_{re_{rc}} & X_{re_{te}} & X_{re_{re}} \end{bmatrix} \quad (3.11)$$

$$a_p H_{\alpha\beta,x}(\omega)X_{\alpha\beta_{nm}} = a_p H_{nm,x}(\omega) \cdot 1 \quad (3.12)$$

$$\mathbf{Y_{Fmatr}} = \begin{bmatrix} Y_{tc_{tc}} & Y_{tc_{rc}} & Y_{tc_{te}} & Y_{tc_{re}} \\ Y_{rc_{tc}} & Y_{rc_{rc}} & Y_{rc_{te}} & Y_{rc_{re}} \\ Y_{te_{tc}} & Y_{te_{rc}} & Y_{te_{te}} & Y_{te_{re}} \\ Y_{re_{tc}} & Y_{re_{rc}} & Y_{re_{te}} & Y_{re_{re}} \end{bmatrix} \quad (3.13)$$

$$a_p H_{\alpha\beta,y}(\omega)Y_{\alpha\beta_{nm}} = a_p H_{nm,y}(\omega) \cdot 1 \quad (3.14)$$

$$\begin{bmatrix} K_{Xtc} \\ K_{Xrc} \\ K_{Xte} \\ K_{Xre} \end{bmatrix} = \mathbf{X_{Fmatr}} \begin{bmatrix} K_{tc} \\ K_{rc} \\ K_{te} \\ K_{re} \end{bmatrix} \quad (3.15)$$

$$\begin{bmatrix} K_{Ytc} \\ K_{Yrc} \\ K_{Yte} \\ K_{Yre} \end{bmatrix} = \mathbf{Y_{Fmatr}} \begin{bmatrix} K_{tc} \\ K_{rc} \\ K_{te} \\ K_{re} \end{bmatrix} \tag{3.16}$$

For a centered workpiece with small wall thickness (a single thin walled workpiece with centerline aligned with X axis), this equation returns roughly (not exactly but approximately) a simple relation with chip thickness as below:

$$\mathbf{X_{Fmatr}} \cong \begin{bmatrix} 1 & 0 & \frac{1}{c} & 0 \\ 0 & 1 & 0 & \frac{1}{c} \\ c & 0 & 1 & 0 \\ 0 & c & 0 & 1 \end{bmatrix} \tag{3.17}$$

$$\mathbf{Y_{Fmatr}} \cong \begin{bmatrix} 1 & 0 & \frac{1}{c} & 0 \\ 0 & 1 & 0 & \frac{1}{c} \\ c & 0 & 1 & 0 \\ 0 & c & 0 & 1 \end{bmatrix} \tag{3.18}$$

Under these conditions, for centered workpiece, equation (3.19) can be written.

$$\begin{aligned} \hat{\mathbf{F}}_{\mathbf{s}}(\boldsymbol{\omega})_{2n\times 1} &= \begin{bmatrix} \hat{F}_x(\boldsymbol{\omega})_{n\times 1} \\ \hat{F}_y(\boldsymbol{\omega})_{n\times 1} \end{bmatrix} \\ &\cong a_p \begin{bmatrix} \mathbf{0}_{n\times 1} & \left|H_{rc,x}(\boldsymbol{\omega})_{n\times 1}\right| & \mathbf{0}_{n\times 1} & \left|H_{rc,x}(\boldsymbol{\omega})_{n\times 1}\right| \\ \left|H_{tc,y}(\boldsymbol{\omega})_{n\times 1}\right| & \mathbf{0}_{n\times 1} & \left|H_{tc,y}(\boldsymbol{\omega})_{n\times 1}\right| & \mathbf{0}_{n\times 1} \end{bmatrix} \begin{bmatrix} K_{tc} \\ K_{rc} \\ K_{te} \\ K_{re} \end{bmatrix} \end{aligned} \tag{3.19}$$

Equation (3.19) is given as amplitude format. With given reduction, phase information is not needed for identification. This equation can be reduced as follows:

$$\mathbf{H}(\boldsymbol{\omega})_{2n\times 2} = \begin{bmatrix} \left|H_{rc,x}(\boldsymbol{\omega})_{n\times 1}\right| & \mathbf{0}_{n\times 1} \\ \mathbf{0}_{n\times 1} & \left|H_{tc,y}(\boldsymbol{\omega})_{n\times 1}\right| \end{bmatrix} \tag{3.20}$$

$$\hat{\mathbf{F}}_{\mathbf{s}}(\boldsymbol{\omega})_{n\times 1} = \begin{bmatrix} \hat{F}_x(\boldsymbol{\omega})_{n\times 1} \\ \hat{F}_y(\boldsymbol{\omega})_{n\times 1} \end{bmatrix} \cong a_p \mathbf{H}(\boldsymbol{\omega})_{2n\times 2} \begin{bmatrix} K_A \\ K_B \end{bmatrix} \tag{3.21}$$

Here K_A and K_B are the intermediate coefficients and are defined as equations (3.22a) and (3.22b).

$$K_A = K_{Xrc} = cK_{rc} + K_{re} \tag{3.22a}$$

$$K_B = K_{Ytc} = cK_{tc} + K_{te} \tag{3.22b}$$

3.2 Identification of Coefficients

Merging three solutions to three problems and utilizing the calculation given in Chapter 3.1, a two-part least squares approach to calculate force coefficients is utilized. In the first part; since multiple sample engagements are available, a recursive least squares approach is applied. Recursive least squares method is selected because force coefficients are expected to converge to a value with more sampled engagement are added into the calculation. This acts as a proxy for quality of the estimation. As a weight matrice, amplitude of known FRF itself is utilized so the results are expected to be more accurate during FRF identification. The second part is simply utilizing the least squares method to separate K_A and K_B into cutting and edge coefficients based on chip thickness.

The recursive least square algorithm is given in equation (3.24). The subscript 'i' is used to count the tool and the workpiece engagements. The response vectors is of size $n \times 1$ and are defined for the frequency array $\boldsymbol{\omega}$. Recursive matrice and regression matrice are given at equation (3.23).

$$\begin{gathered}\mathbf{H} = H_{nm,D}(\boldsymbol{\omega})_{n\times 1} \\ \mathbf{W} = \mathbf{G}_{DD}(\boldsymbol{\omega})_{n\times 1}\end{gathered} \tag{3.23}$$

$$\begin{gathered}\mathbf{P}_i = ([\mathbf{H} \circ \mathbf{W}]^T\mathbf{H})^{-1} \\ [K_{Dnm}]_i = \mathbf{P}_i[\mathbf{H} \circ \mathbf{W}]^T\left[\hat{F}_{D,i}(\boldsymbol{\omega})_{n\times 1}\right] \\ \mathbf{P}_{i+1} = \left(\mathbf{P}_i^{-1} + [\mathbf{H} \circ \mathbf{W}]^T\mathbf{H}\right)^{-1} \\ \mathbf{J}_{i+1} = \mathbf{P}_{i+1}[\mathbf{H} \circ \mathbf{W}]\end{gathered} \tag{3.24}$$

$$[K_{Dnm}]_{i+1} = [K_{Dnm}]_i + \mathbf{J_{i+1}}\left(\left[\widehat{H}_{D,i}(\boldsymbol{\omega})_{n\times 1}\right] - \mathbf{H}[K_{Dnm}]_i\right)$$

Here, $\circ$ symbol in $[\mathbf{H} \circ \mathbf{W}]$ indicates piecewise multiplication as equation (3.25).

$$[\mathbf{H} \circ \mathbf{W}]_{uq} = \mathbf{H}_{uq}\mathbf{W}_{uq} \quad uq \rightarrow \text{index} \tag{3.25}$$

For centered workpiece, recursive least squares equation is given below:

$$\begin{gathered}
\mathbf{P_i} = ([\mathbf{H} \circ \mathbf{W}]^T\mathbf{H})^{-1} \\
\begin{bmatrix} K_A \\ K_B \end{bmatrix}_i = \mathbf{P_i}[\mathbf{H} \circ \mathbf{W}]^T \begin{bmatrix} \mathbf{G_{xx}}(\boldsymbol{\omega})_{n\times 1}{}^{-1}\mathbf{x_i}(\boldsymbol{\omega})_{n\times 1} & \mathbf{0_{n\times 1}} \\ \mathbf{0_{n\times 1}} & \mathbf{G_{yy}}(\boldsymbol{\omega})_{n\times 1}{}^{-1}\mathbf{y_i}(\boldsymbol{\omega})_{n\times 1} \end{bmatrix} \\
\mathbf{P_{i+1}} = \left(\mathbf{P_i^{-1}} + [\mathbf{H} \circ \mathbf{W}]^T\mathbf{H}\right)^{-1} \\
\mathbf{J_{i+1}} = \mathbf{P_{i+1}}[\mathbf{H} \circ \mathbf{W}] \\
\begin{bmatrix} K_A \\ K_B \end{bmatrix}_{i+1} = \begin{bmatrix} K_A \\ K_B \end{bmatrix}_i + \mathbf{J_{i+1}}\left(\begin{bmatrix} \mathbf{G_{xx}}(\boldsymbol{\omega})_{n\times 1}{}^{-1}\mathbf{x_i}(\boldsymbol{\omega})_{n\times 1} & \mathbf{0_{n\times 1}} \\ \mathbf{0_{n\times 1}} & \mathbf{G_{yy}}(\boldsymbol{\omega})_{n\times 1}{}^{-1}\mathbf{y_i}(\boldsymbol{\omega})_{n\times 1} \end{bmatrix} - \mathbf{H}\begin{bmatrix} K_A \\ K_B \end{bmatrix}_i\right)
\end{gathered} \tag{3.26}$$

Here, P_i is the covariance matrice (alternatively called information matrice) at i_{th} sampled engagement. In this application matrice size is 2×2. $\mathbf{H}_{2n\times 2}$ is the regressor matrice (alternatively called basis matrice) which comes from a set of linear equations which in this case are equation (3.20). J_{i+1} is referred as Kalman gain because recursive least squares work in the same principle as Kalman filter. Finally, the intermediate coefficients $[K_A \quad K_B]^T_{i+1}$ is calculated and the cycle repeats with i increasing by one until all selected sampled engagements are used, finalizing the calculation. Note $[\mathbf{H} \circ \mathbf{W}]$ utilizes element-wise multiplication (3.25) for memory efficiency. This is for saving memory as diagonal weight matrices are sparse. In order to increase the quality of the estimations a weight matrice $\mathbf{W}_{2n\times 2}$, which consists of the amplitude of known FRF itself is utilized.

$$\mathbf{W} = \begin{bmatrix} |\mathbf{G_{xx}}(\omega)_{n\times 1}| & \mathbf{0_{n\times 1}} \\ \mathbf{0_{n\times 1}} & |\mathbf{G_{yy}}(\omega)_{n\times 1}| \end{bmatrix} \tag{3.27}$$

The reason to utilize such a weight matrice is to give more importance into frequency domain with higher excitation values as such regions are more likely to have better signal to noise ratio.

In the second part, with the help of various tests with different feed per insert, force coefficients are separated into edge and shear components, as explained equation (3.28) and (3.29), completing identification of force coefficients.

$$\mathbf{K_{Dnm}} = \begin{bmatrix} K_{Dnm,1} \\ \vdots \\ K_{Dnm,n} \end{bmatrix} \quad \mathbf{H_{Dnm}} = \begin{bmatrix} D_{nm_{tc},1} & D_{nm_{te},1} & D_{nm_{rc},1} & D_{nm_{re},1} \\ \vdots & \vdots & \vdots & \vdots \\ D_{nm_{tc},n} & D_{nm_{tc},n} & D_{nm_{tc},n} & D_{nm_{tc},n} \end{bmatrix} \tag{3.28}$$

n → Number of tests with different proces parameters

$$\begin{bmatrix} K_{tc} \\ K_{te} \\ K_{rc} \\ K_{re} \end{bmatrix} = \left(\mathbf{H_{Dnm}^T} \cdot \mathbf{H_{Dnm}}\right)^{-1} \cdot \mathbf{H_{Dnm}^T} \mathbf{K_{Dnm}} \tag{3.29}$$

For centered workpiece, the second least squares can be simplified as below:

$$\mathbf{K_A} = \begin{bmatrix} K_{A,1} \\ \vdots \\ K_{A,n} \end{bmatrix} \quad \mathbf{K_B} = \begin{bmatrix} K_{B,1} \\ \vdots \\ K_{B,n} \end{bmatrix} \quad \mathbf{H_1} = \begin{bmatrix} c_1 & 1 \\ \vdots & \vdots \\ c_n & 1 \end{bmatrix} \tag{3.30}$$

n → Number of tests with different feed per tooth

$$\begin{bmatrix} K_{tc} \\ K_{te} \end{bmatrix} = \left(\mathbf{H_1^T} \cdot \mathbf{H_1}\right)^{-1} \cdot \mathbf{H_1^T} \mathbf{K_A} \quad \begin{bmatrix} K_{rc} \\ K_{re} \end{bmatrix} = \left(\mathbf{H_1^T} \cdot \mathbf{H_1}\right)^{-1} \cdot \mathbf{H_1^T} \mathbf{K_B} \tag{3.31}$$

3.3 Application on the Model

The approach this thesis uses relies on FRF obtained through tap tests and acceleration measurements taken during a cutting process with controlled parameters. Figure 3.3 explains the approach of how to obtain force coefficients. Explaining the basic framework of the method step by step:

A. Given as “Point FRF”, an FRF representing behavior of the machine-tool structure in which measurement is to be taken is needed for force estimation in the following steps. This FRF is obtained through tap tests in this thesis.
B. Measured acceleration is data obtained during operation with an accelerometer. Every window with boundaries are a sample data such as $x_i(t)$ or $y_i(t)$. As it can be seen, there are slight variations at data in different time sections, as this is also the case in the real system. In total, the data are sampled with 7 windowed time chapters. Selection of time sections are determined so that when acceleration response to the force occurred during one contact is in the windowed time frame, from when acceleration starts to rise until acceleration dampens out.
C. The same acceleration at the previous step that has been sampled with 7 windows are represented in frequency domain. For this description, sampling provides 7 separate acceleration measurements; for example for X direction, it is $x_i(t)$ $i \in \{1,2,\dots,7\}$, which were resulted from 7 tool contacts, converted to frequency domain as $x_i(\omega)$ $i \in \{1,2,\dots,7\}$, as i represents a sample data.
D. For every sample data, force estimation $\left(F_{x,i}(\omega), F_{y,i}(\omega)\right)$ is obtained thought equation (3.6b) point FRF and sampled data $x_i(t)$.
E. Together with the force model (given in Chapter 2), curve fitting force estimation with force coefficients is applicable. $K_{A,i}$ and $K_{B,i}$ intermediate force coefficients are estimated with this curve fitting. Calculations of curvefit is explained in this chapter, on the following paragraphs.
F. Repeating the first 5 steps for various tests with different feed per insert values, Recursive Least Squares Method is applied to obtain K_A and K_B and

a second least squares method with chip thickness is used to obtain 4 force coefficients.

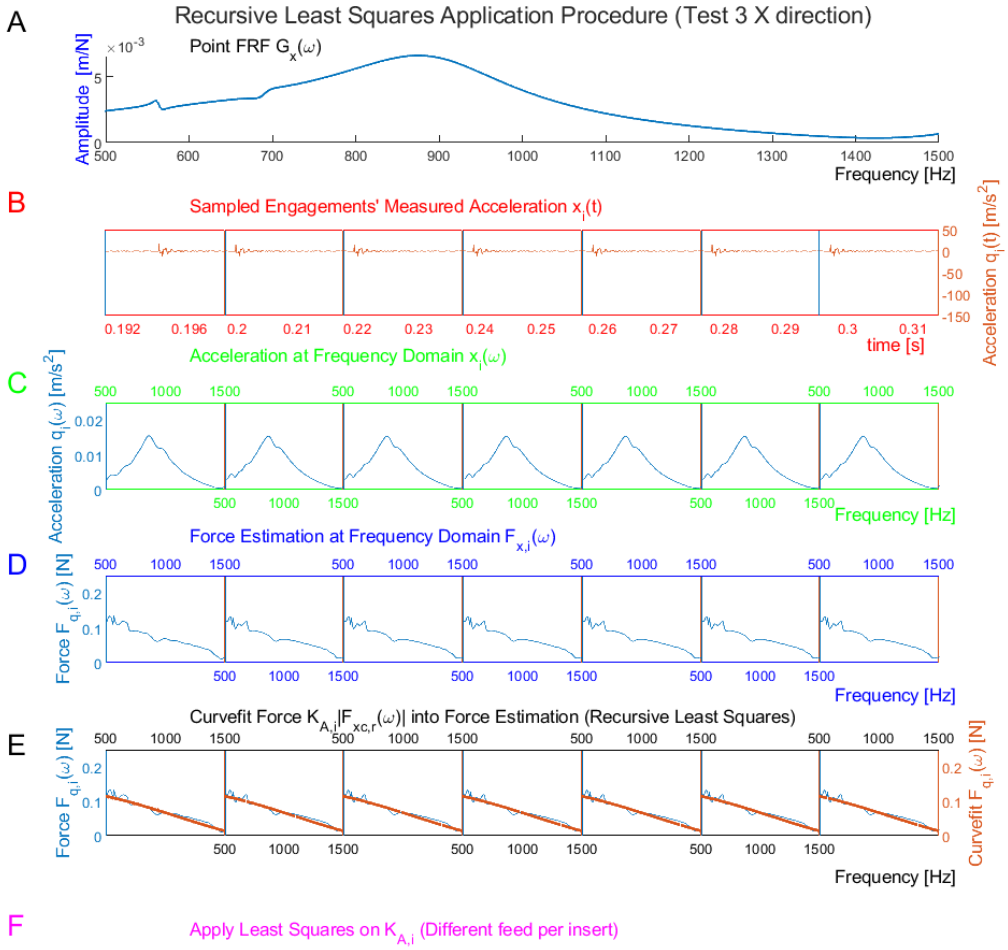

Figure 3.3 Explanation of Cutting Coefficients Identification (Simulation Test 3)

Simulation is designed for testing identification methods. For force coefficients, 3 tests have been performed. Process parameters of the 3 mentioned tests are detailed in Table 3-1. Force coefficients are taken from Table 2-7 and the same force coefficients are identification outputs obtained at Chapter 5. FRFs are substituted from modal analysis outputs shown in Figure 2.6 and Figure 2.7 for simulation. 500-1500 [Hz] frequency domain has been selected for identification. The reason for this selection is because the same frequency domain is selected for identification with

experiment data and the choice explained in the experiment chapter. Those reasons cannot be observed in simulation.

Table 3-1: Test Parameters of Cutting Force Identification (Simulation Demonstration) D=63.3 [mm], ap=2.9 [mm]

Test	V_x [mm/min]	n_s [rpm]	L [mm]	Workpiece Type
1	600	3072	6	Centered
2	450	3072	6	Centered
3	300	3072	6	Centered

In Table 3-1, feed and angular speed parameters are selected to achieve different chip thickness values because in order to apply equations (3.28) and (3.29) multiple chip thickness values are needed. Zero crossing value that is calculated with equation (2.11) is 3181 [Hz] for three "tests" and this is sufficient for 3000 [Hz] maximum value for frequency domain that is limited by the tap test applied. Wall depth is constant and higher than axial depth, which is also constant.

Step E of identification of force coefficients is shown with test 3 simulation output in Figure 3.4. Force estimations are calculated according to equation (3.6b) and given in blue color for every data sampled, as numbered from 1 to 7. With progressing recursive least squares method, $K_{A,i}$ are calculated according to equation (3.26) and $K_{A,i}$ are used for force curvefit as shown in the figure.

Engagements sampled and obtained from the figure above are as shown in Figure 3.6. Acceleration data at Figure 3.6 has been used to obtain force estimations of Figure 3.4. Figure 3.4 is equivalent to Step E of FRF identification method given at Figure 3.3 with the exception that force at every engagement sampled was calculated with $K_{A,i}$ instead of a single value through. If this was experimental data, the amplitude of force at every engagement sampled was going to be slightly different. An important point to be seen is that as mentioned several times before amplitude of acceleration dampens out quickly, which is necessary for the quality of results being sufficient.

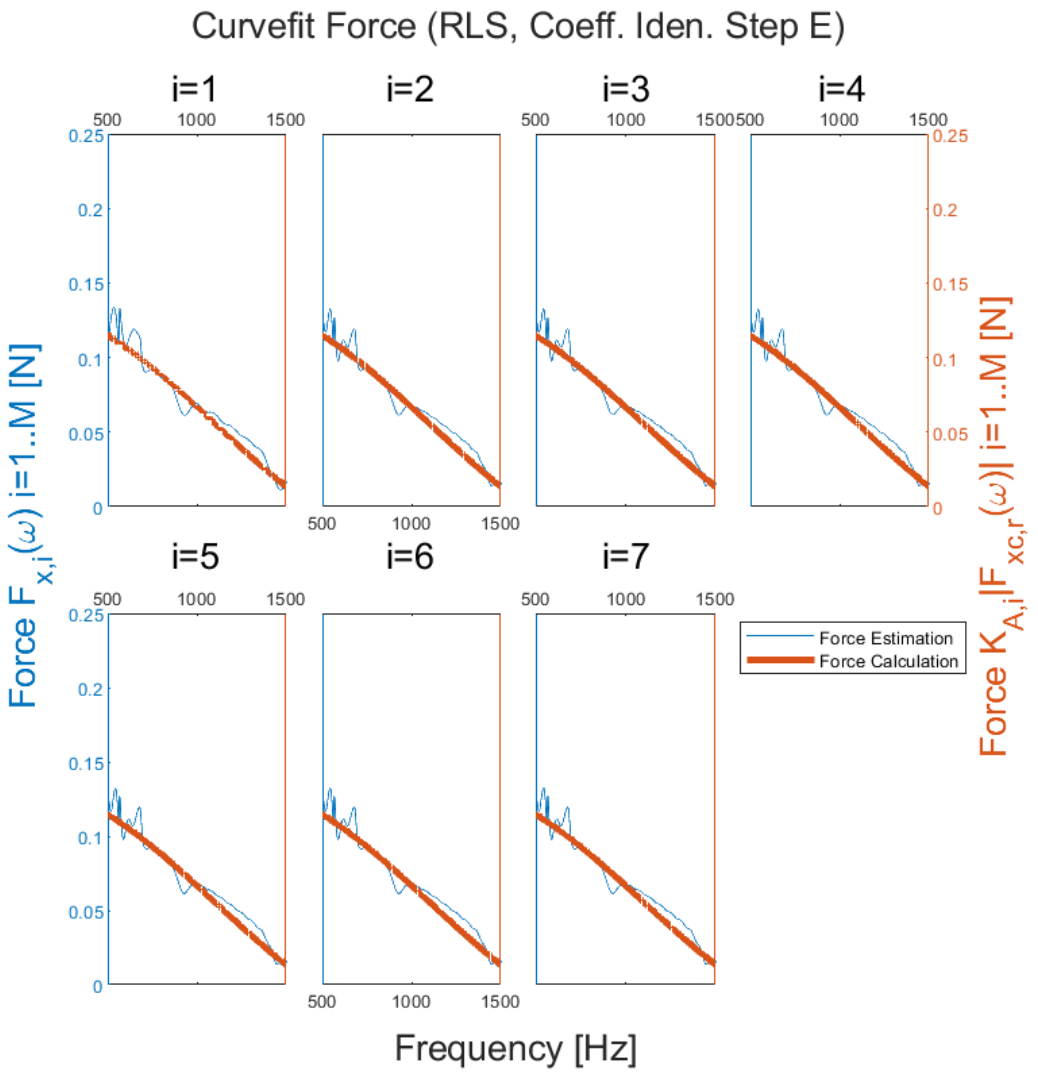

Figure 3.4 Test 3, Recursive Least Squares Application Of Calculating $K_{A,i}$ (Simulation Version Of Step E of Calculation of Force Calculation From Chapter 3.2)

For all coefficients at all tests, Figure 3.5 gives the recursive calculation of $(K_{A,i}, K_{B,i})$ for all 3 tests. As it is shown in Figure 3.5, $(K_{A,i}, K_{B,i})$ converges into a value.

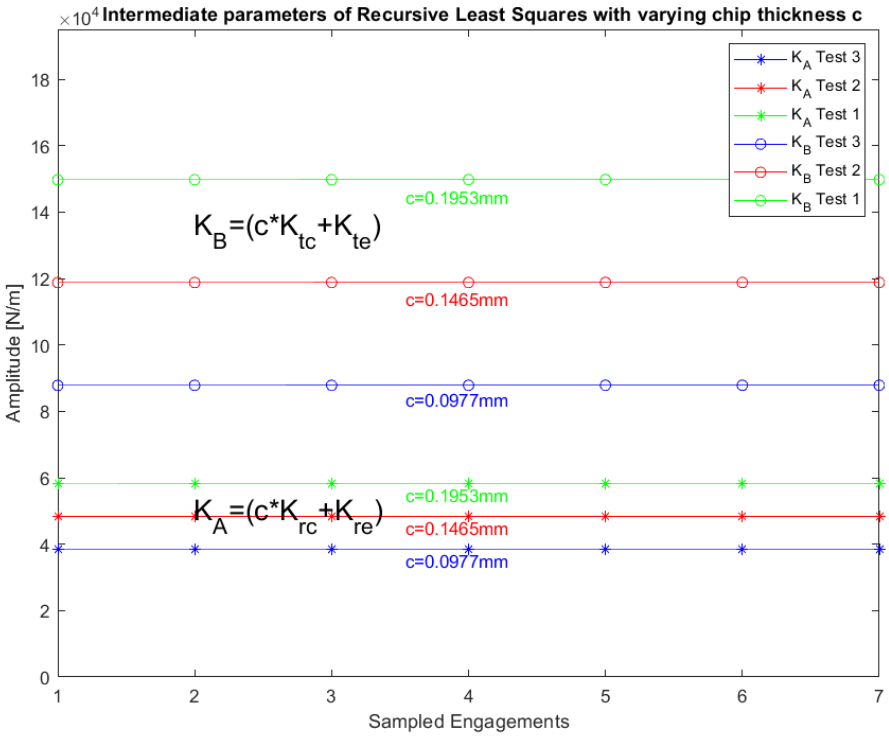

Figure 3.5 Variations of Force Coefficients During Recursive Least Squares, Simulation

Table 3-2 gives identified K_A and K_B for every test. Values on this table are simply the end value of the previous table as end result of recursive least squares method is taken as final value of K_A and K_B. As it is expected, chip thickness being smaller results in larger values for K_A and K_B. Resulting FRF identification outputs (FRFs identified by obtaining Step E of FRF identification method as shown in Figure 3.6 for every test and applying a suitable FRF calculation method like it is suggested at equations (4.1) to (4.4) while at the same time applying K_A and K_B as K_{tc} and K_{rc} respectively) can be seen in Figure 3.7 and Figure 3.8. Y direction provides less accurate results as the effect of cross FRF is higher. FRF identification method is given in Chapter 4.

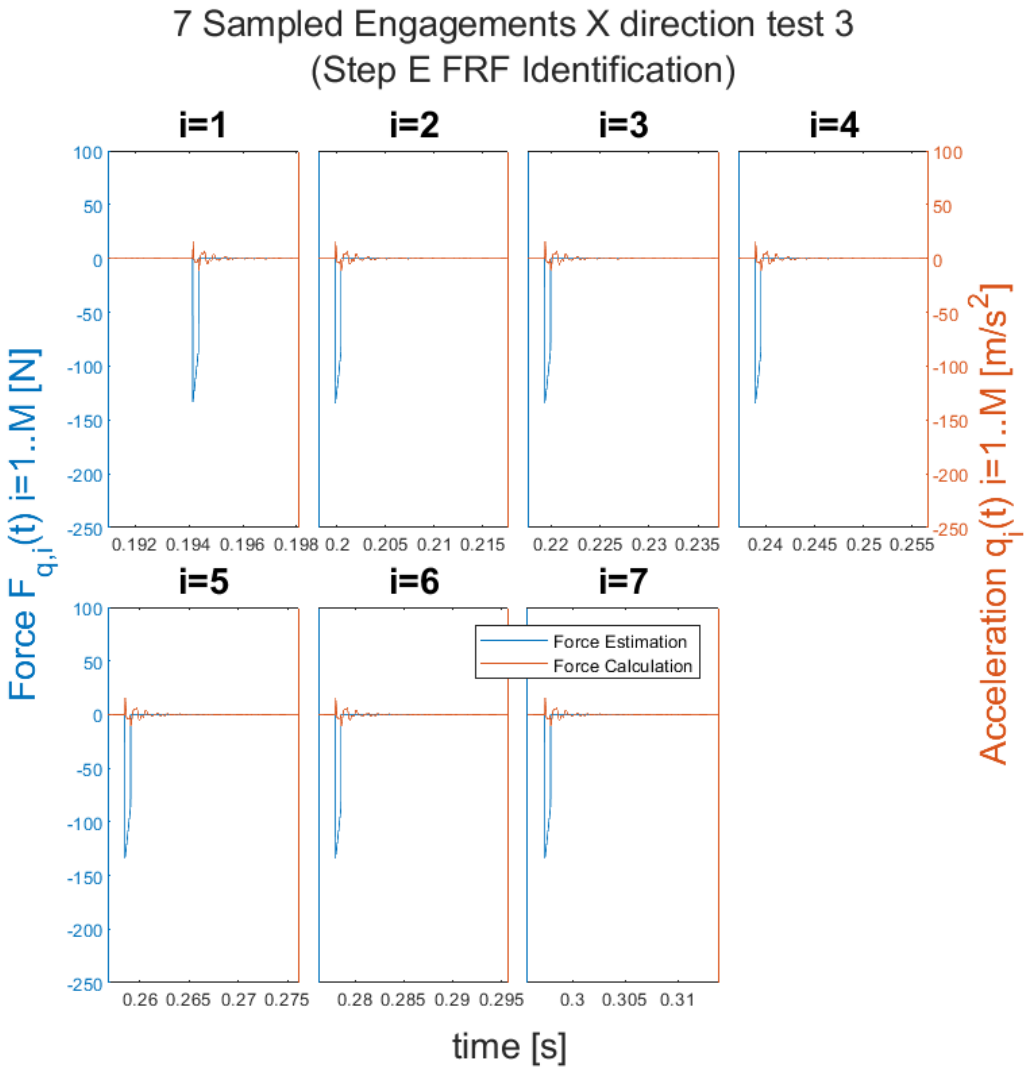

Figure 3.6 7 Engagements Sampled from X Direction Test 3 (Step E FRF Identification) Simulation

Table 3-2: Intermediate Force Coefficients Identified. (Simulation)

	Recursive Least Squares Output	
Test	**K_B [N/m]**	**K_A [N/m]**
3	149.74e3	58.34e3
2	118.79e3	48.33e3
1	87.83e3	38.32e3

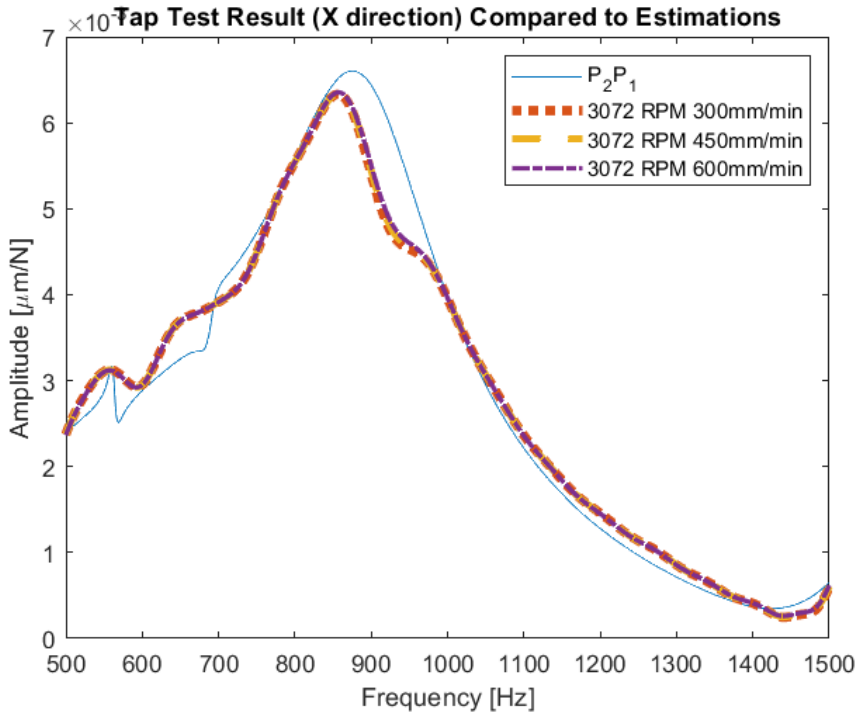

Figure 3.7 Tap Test Result (X direction) Compared to FRF Identification (Simulation)

Since K_A and K_B are obtained and their accuracy is controlled qualitatively with several approaches, applying the second part of identification of force coefficients is available. Three tests with different chip thickness values offered three sets of K_A and K_B. Using equation (3.28) and (3.29) on Table 3-2, force coefficients are identified in Table 3-3. Original coefficients have not been exactly obtained but the results are accurate. If cross FRFs are not omitted, results slightly shift for

coefficients obtained from Y direction changes more significantly for X direction. Values obtained are slightly smaller.

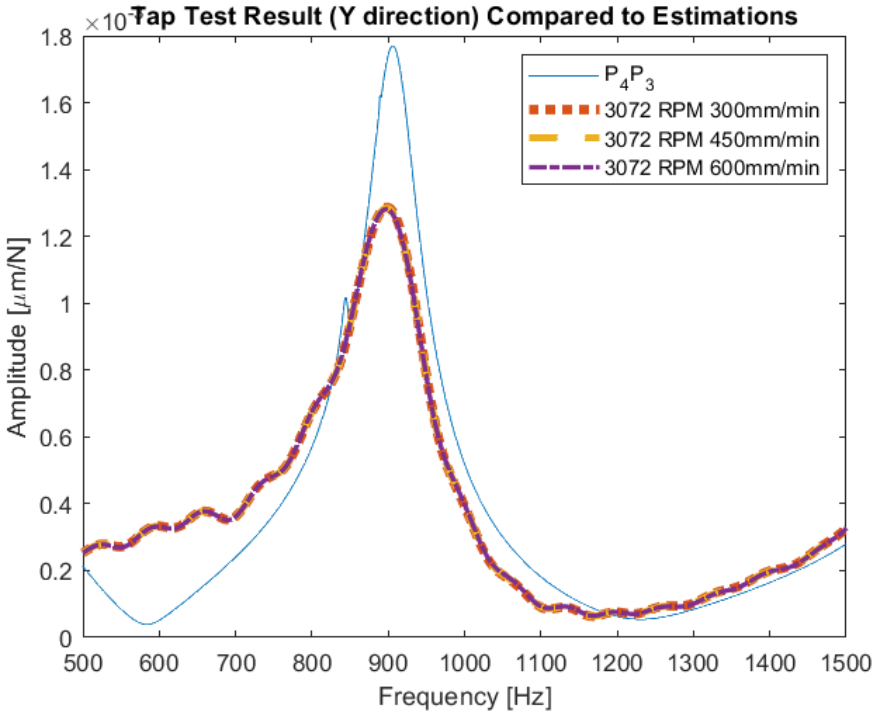

Figure 3.8 Tap Test Result (Y direction) Compared to FRF Identification (Simulation)

Table 3-3: Force Coefficients (Cross FRF Omitted)

K_{tc}=634 [MPa]	K_{rc}=205.07 [MPa]
K_{te}=25.92 [kN/m]	K_{re}=18.29 [kN/m]

Table 3-4: Force Coefficients (Cross FRF Included)

K_{tc}=581 [MPa]	K_{rc}=175.37 [MPa]
K_{te}=20.58 [kN/m]	K_{re}=17.01 [kN/m]

CHAPTER 4

FRF IDENTIFICATION WITH SELECTED ENGAGEMENTS

This section explains FRF identification procedures utilized in this thesis. It is assumed that procedures at the previous chapter are followed or force coefficients of the workpiece to be processed is determined. In addition, practical solutions applied in the previous chapter for identification of force coefficients are used in this chapter, such as utilizing individual engagements and omitting cross FRF from the calculation. Details are presented at their respective sections. Section 4.1 explains the theory of the approach followed without calculations. Section 4.2 provides calculations. Section 4.3 presents application of the method at the simulation, along with discussion of the results. Section 4.4 provides a separate, two dimensional FRF identification approach.

4.1 FRF Calculation Method with Selected Engagements

Since acceleration measurements and force calculation shows harmonic peaks as dominant in the frequency domain, direct application of FRF calculation is inaccurate in practice. Moreover, since this thesis uses calculated force, placement of force with time is not as accurate as measuring force simultaneously with response. This issue is mentioned at Chapter 3.1 for identification of force coefficients while explaining the application of equation (3.5).

FRF identification method offered here relies on the fact that noise is low and damping is relatively high for this system (machine tool and workpiece together), the very same thing that identification of force coefficients method relies on. This means that table acceleration measurements can be sampled out with individual force

excitations as sampled engagements given at Figure 3.1. The fundamental principle of the method is that since every engagement is a time section of a singular impulse and a singular response from contact moment to the damping out of the response, every engagement can be regarded as a single tap test. Moreover, given cross FRFs are small and unreliable, they are omitted just like equation (3.6b). Figure 4.1 describes the method from top to bottom.

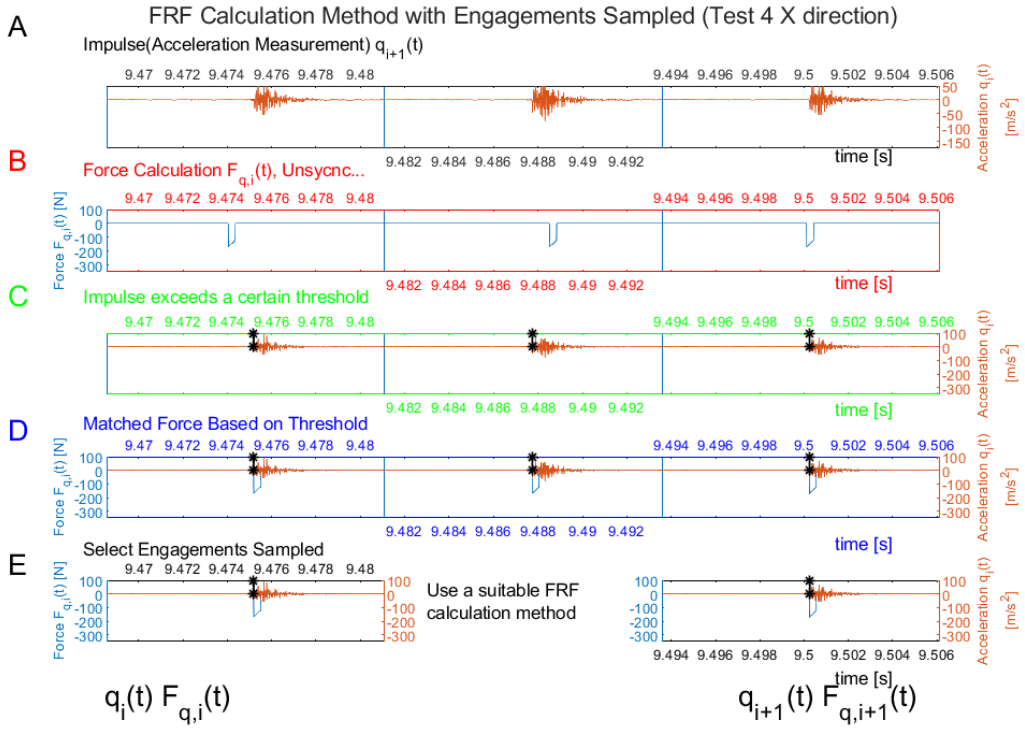

Figure 4.1 FRF Identification Method Described with Synchronization Based on Threshold (Experiment Data)

A. Acceleration measurement is performed and data are given.

B. Based on process parameters (axial depth, force coefficients etc…), force is calculated. Due to variations in angular speed and angular positions of cutting tool changes in feed and tolerances of workpiece, calculated force may not be synchronized to the measurement.

C. Force calculation is synchronized according to the absolute value of acceleration values. Calculated forces per tool contact is placed right after magnitude of acceleration exceeds a certain value.

D. Application of first three steps provides a force calculation synchronized onto acceleration measurement obtained.

E. Time sections around forces and their responses are windowed, obtaining engagements sampled.

Synchronization procedure is especially critical in cases where angular speed of cutting tool is hard to pinpoint as in experiment phase, since force calculation is not automatically synchronized with table response like in a measurement, the method used to match force calculation with measurements are described in Figure 4.1 is one of the factors makes this technique possible. Force calculated is placed in the moment amplitude of measurement value exceeds a threshold. This method is introduced at Figure 3.1.

4.2 FRF Calculation

After obtaining engagements, any suitable method of obtaining FRF from tap tests can also be used in this case. For this thesis, the spectral density function is used for the calculation of FRF. Defining $F_{q,i}(\omega)$ as frequency domain version of force excitation at i_{th} engagement sampled and $q_i(\omega)$ as frequency domain version of workpiece response at i_{th} engagement sampled, equations (4.1a) to (4.1d) are written.

$$S_{qq,i}(\omega) = q_i(\omega) \cdot q_i(\omega)^T \tag{4.1a}$$

$$S_{qF,i}(\omega) = q_i(\omega) \cdot F_{q,i}(\omega)^T \tag{4.1b}$$

$$S_{Fq,i}(\omega) = F_{q,i}(\omega) \cdot q_i(\omega)^T \tag{4.1c}$$

$$S_{FF,i}(\omega) = F_{q,i}(\omega) \cdot F_{q,i}(\omega)^T \tag{4.1d}$$

Functions given at equations (4.1a) to (4.1d) are spectral density functions. $q_i(\omega)'$ indicates conjugate of $q_i(\omega)$.

The average of spectral density functions are taken as equation (4.2a).

$$S_{qq}(\omega) = \sum_{i=1}^{N} \frac{S_{qq,i}(\omega)}{N} \tag{4.2a}$$

$$S_{qF}(\omega) = \sum_{i=1}^{N} \frac{S_{qF,i}(\omega)}{N} \tag{4.2b}$$

$$S_{Fq}(\omega) = \sum_{i=1}^{N} \frac{S_{Fq,i}(\omega)}{N} \tag{4.2c}$$

$$S_{FF}(\omega) = \sum_{i=1}^{N} \frac{S_{FF,i}(\omega)}{N} \tag{4.2d}$$

N is the number of engagements selected. FRF is calculated as equation (4.3). Coherence is be calculated as equation (4.4).

$$G(\omega) = \frac{S_{qq}(\omega)}{S_{qF}(\omega)} \equiv \frac{S_{Fq}(\omega)}{S_{FF}(\omega)} \tag{4.3}$$

$$C(\omega) = \frac{|S_{qF}(\omega)|}{\sqrt{S_{qq}(\omega) S_{FF}(\omega)}} \tag{4.4}$$

4.3 Application on the Model

The method needs to be demonstrated with simulation before testing because testing is expensive and cumbersome. Table 4-1 provides process parameters. Force parameters are taken from Table 2-7.

Table 4-1: Test Parameters of FRF identification (Simulation) D=63.3 [mm], a_p=2.9 [mm]

Test	V_x [mm/min]	n_s [rpm]	L [mm]
4	600	4800	6

To demonstrate the method better, Step E from Figure 4.1 is visualized with experiment data as shown in Figure 4.2. 7 engagements obtained from simulation are given in the figure. Data is sampled according to angular speed of cutting tool and synchronization based on threshold has been utilized for matching force calculations to accelerations measured. Data and force estimation are zero padded to reach 1 [Hz] in frequency domain.

After obtaining results shown in Figure 5.12, any method applicable to multiple tap test measurements can be used for this case. Equations from (4.1) to (4.4) explain the method for this paper.

Figure 4.3 and Figure 4.4 provide the end results of FRF identification method based on simulation. Result for X direction is sufficient. X direction proves more successful due to $G_{1,yx}(\omega)$ being insignificant compared to $G_{1,xx}(\omega)$. In other words, Figure 4.4 results are comparably worse due to significant cross FRF effect compared to X direction.

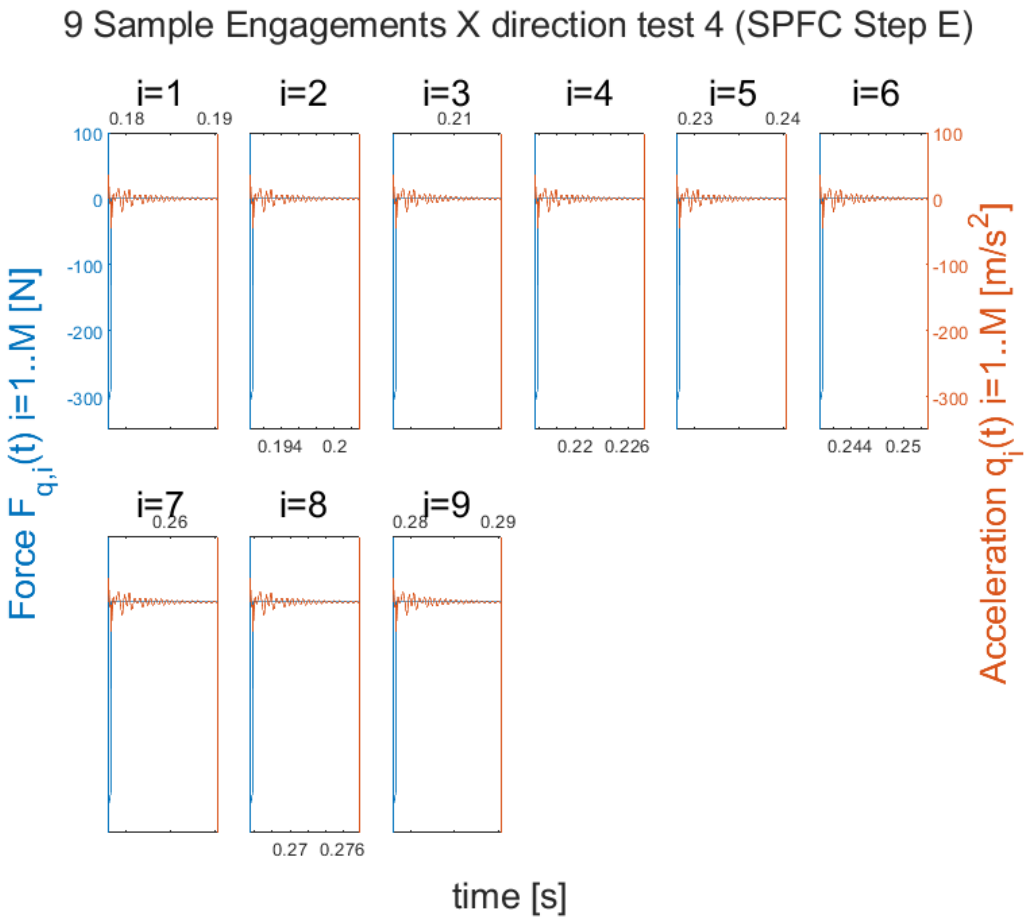

Figure 4.2 FRF Identification Step E with Simulation (Test 4)

The method obtains better results under these conditions:

1. Lack of sufficient damping to completely settle transient response is observed to be a more significant issue at lower frequency domain. Lower frequency domain region benefits from lower angular speed.
2. Since the method is 1D, systems with insignificant cross FRFs return results that are more accurate.
3. Window used to obtain engagements sampled should start from as close as to when the cutting tool-workpiece contact happened to prevent interference from the previous contact.

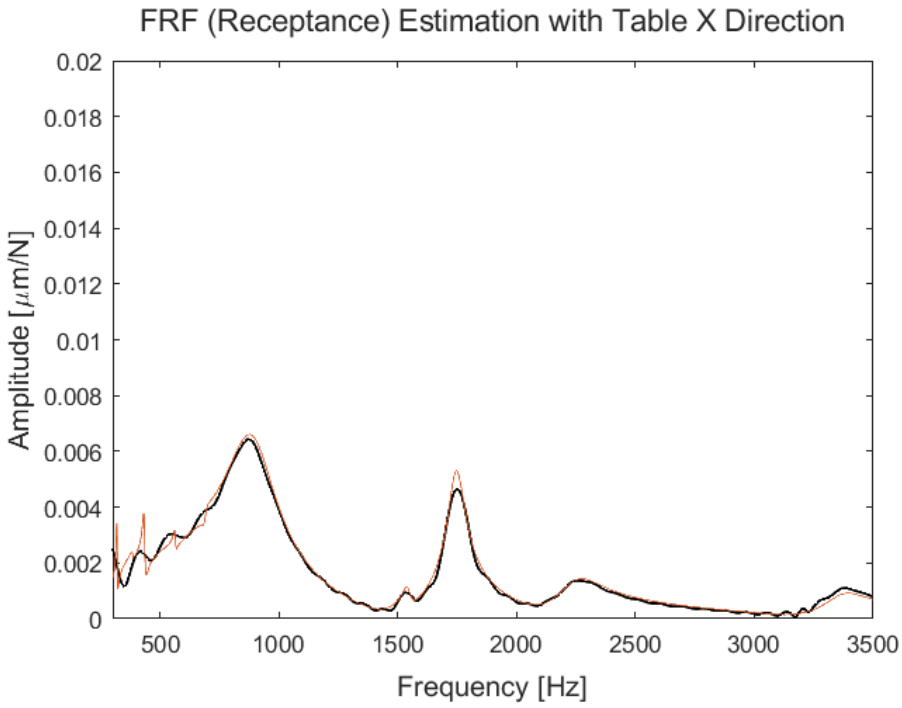

Figure 4.3 FRF Identification Results from Simulation for X Direction

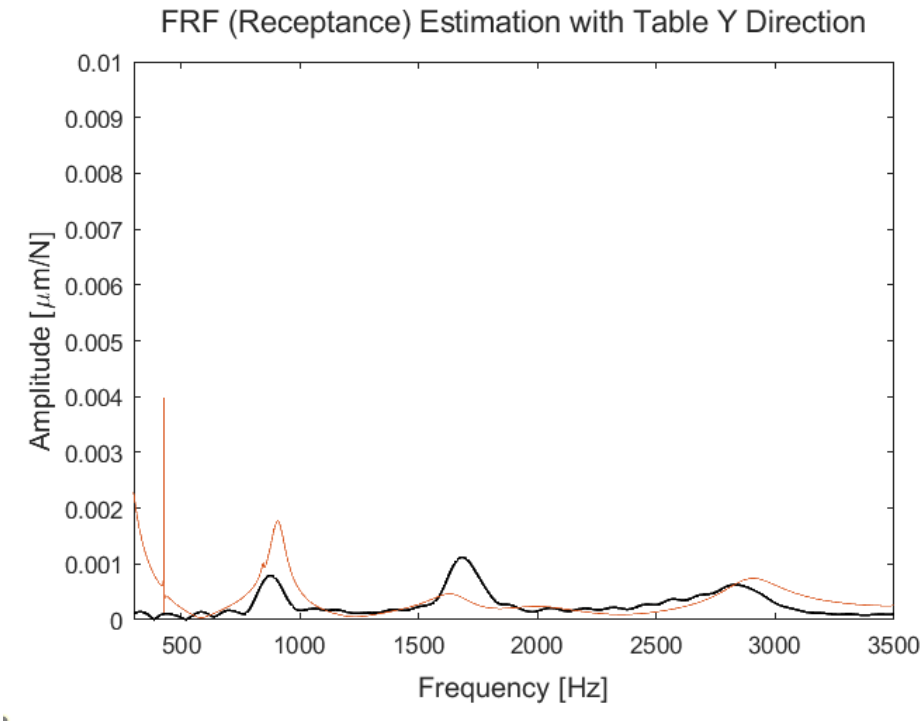

Figure 4.4 FRF Identification Results from Simulation for Y Direction

4.4 Two Dimensional FRF Identification

The reader is suggested to read the rest of Chapter 4 before reading this section.

Since it is visible that one dimensional method failed to obtain accurate results for Y direction under perfect transfer function conditions (FRF of transfer functions used for simulation is known because the researcher determines it exactly.) and X direction provides an accurate result in the given frequency domain, the weight of cross FRF is deemed critical enough that it makes FRF identification by omitting it difficult. Given this factor, it should be investigated whether an identification method including cross FRF is possible.

For two dimensional FRF identification, the fundamental challenge is that acceleration at both Cartesian directions (X and Y direction) are affected by both Cartesian forces (Force in X direction has response at both X and Y directions). This means that identification cannot be reduced to a single engagement sampled and

alternatively multiple engagements should be used. This situation creates two problems for the application of the method. The first one is that identification of cross FRF can require a wide physical region (the distance on the workpiece) and for this reason, local identification can be challenging. The second one is that an alternative quality measurement method to coherence can be needed.

The identification method starts with collecting every engagement sampled in frequency domain. $X_i(\boldsymbol{\omega})_{n\times 1}$ $Y_i(\boldsymbol{\omega})_{n\times 1}$ are responses at i_{th} engagement given $i \in \{1, \dots, N\}$ and $F_{x,i}(\omega)$ $F_{y,i}(\omega)$ are Forces at i_{th} engagement. A collected set of engagements in frequency domain enables identification per frequency points selected as equation (4.7) gives the identification result below:

$$\mathbf{YY_n} = \begin{bmatrix} X_1(\omega_n) \\ \vdots \\ X_D(\omega_n) \\ Y_1(\omega_n) \\ \vdots \\ Y_D(\omega_n) \end{bmatrix} \tag{4.5}$$

$$\mathbf{F_{\omega_n}} = \begin{bmatrix} F_{x,1}(\omega_n) & 0 & F_{y,1}(\omega_n) & 0 \\ \vdots & \vdots & \vdots & \vdots \\ F_{x,i}(\omega_n) & 0 & F_{y,i}(\omega_n) & 0 \\ 0 & F_{x,1}(\omega_n) & 0 & F_{y,1}(\omega_n) \\ \vdots & \vdots & \vdots & \vdots \\ 0 & F_{x,i}(\omega_n) & 0 & F_{y,i}(\omega_n) \end{bmatrix} \tag{4.6}$$

$$\begin{bmatrix} G_{xx}(\omega_n) \\ G_{xy}(\omega_n) \\ G_{yx}(\omega_n) \\ G_{yy}(\omega_n) \end{bmatrix} = \left(\mathbf{F_{\omega_n}^T} \cdot \mathbf{F_{\omega_n}}\right)^{-1} \cdot \mathbf{F_{\omega_n}^T YY_n} \tag{4.7}$$

Here, $\mathbf{YY_n}$ indicates all acceleration values at $\omega_n$frequency point sampled. $\mathbf{F_{\omega_n}}$ indicates all force calculations at $\omega_n$frequency point sampled. Equation (4.7) should be repeated for all frequency points selected.

For a quality indicator, acceleration data utilized for identification can be compared to the acceleration that can be calculated with obtained transfer functions.

$$\begin{bmatrix} X_1(\omega_n) \\ \vdots \\ X_D(\omega_n) \\ Y_1(\omega_n) \\ \vdots \\ Y_D(\omega_n) \end{bmatrix} \cong \begin{bmatrix} G_{xx}(\omega_n) \\ G_{xy}(\omega_n) \\ G_{yx}(\omega_n) \\ G_{yy}(\omega_n) \end{bmatrix} \mathbf{F}_{\boldsymbol{\omega_n}} \tag{4.8}$$

For identification, two tests that are in close proximity and in perpendicular direction are selected. Variations between force calculations are desired as effects of cross FRF should be contrasted by applying various excitations. In other words, effects of cross FRFs should be observable with given excitation for identification. The optimal excitation profile is uncertain and requires more research and for this reason, excitation must be tested with simulation. If this set of parameters provides good identification results with simulation, they can be utilized for testing. However, experimenting with simulation has shown that tests performed in perpendicular feed directions offer more accurate results compared to tests performed in the same direction. This knowledge should be used as a guideline.

Table 4-2: Test Parameters for Two Dimensional FRF Identification (Simulation Demonstration) D=63.3 [mm], a_p=2.9 [mm]

Test	**V_x [mm/min]**	**n_s [rpm]**	**L [mm]**	**Workpiece Type**	**Direction of Cut**
1	600	3072	6	Centered	X
4	600	4800	5	Centered	Y

Force coefficients utilized for testing is the same from Table 2-7.

Force excitations sampled are given at Figure 4.5 and Figure 4.6 below:

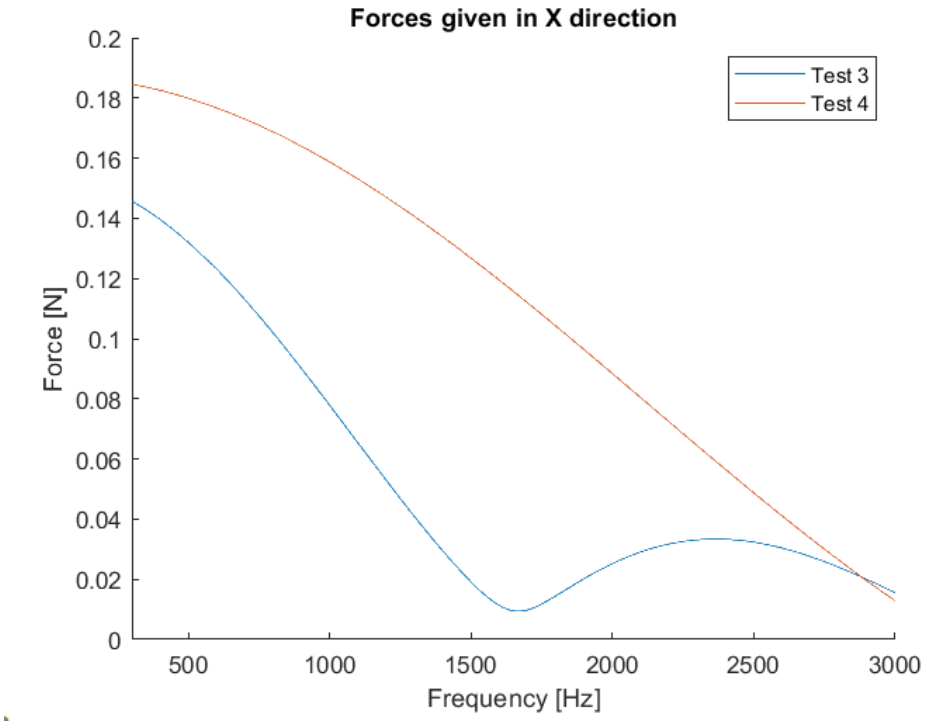

Figure 4.5 Force Calculations for X direction (Two Dimensional FRF Calculation)

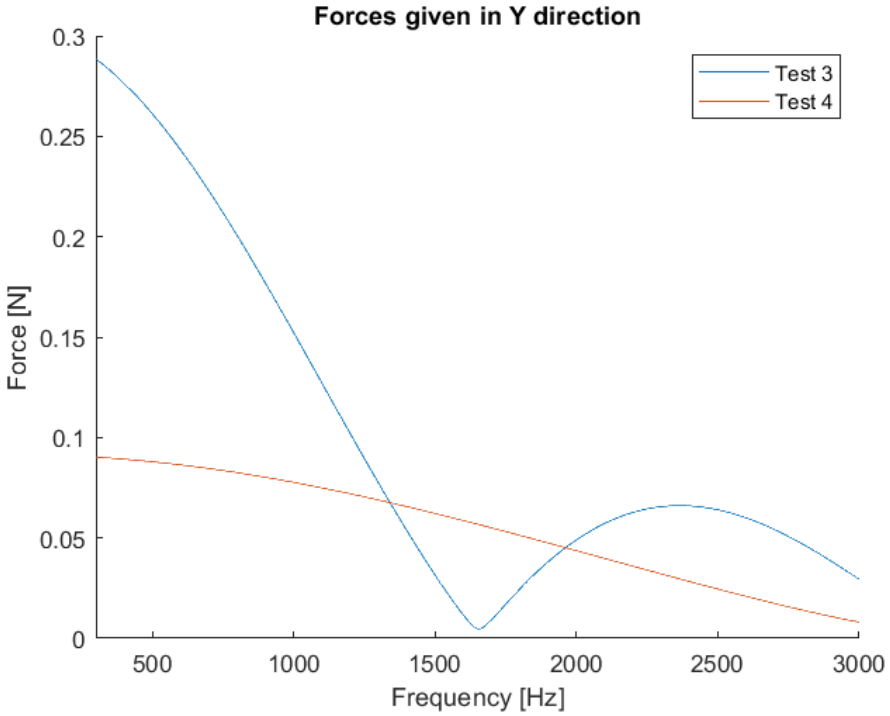

Figure 4.6 Force Calculations for Y direction (Two Dimensional FRF Calculation)

From force profile, frequency values close to zero crossings can be inaccurate. Otherwise, there are variations between profiles for identification. Acceleration outputs that are sampled from the simulation are provided together with acceleration calculations that are done with equation (4.7); at Figure 4.7 and Figure 4.8. FRFs obtained are used to obtain accelerations used for identification successfully.

It can be concluded that two dimensional FRF identification (i.e. including cross FRF) is possible with the given method but results are always more accurate at the dominant FRF.

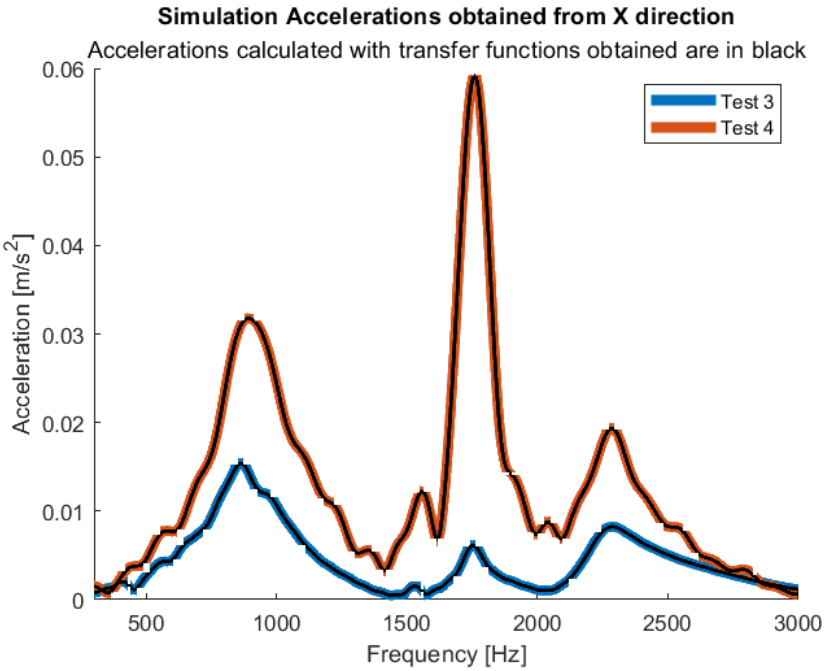

Figure 4.7 Simulation Accelerations Obtained from X Direction (Two Dimensional FRF Calculation)

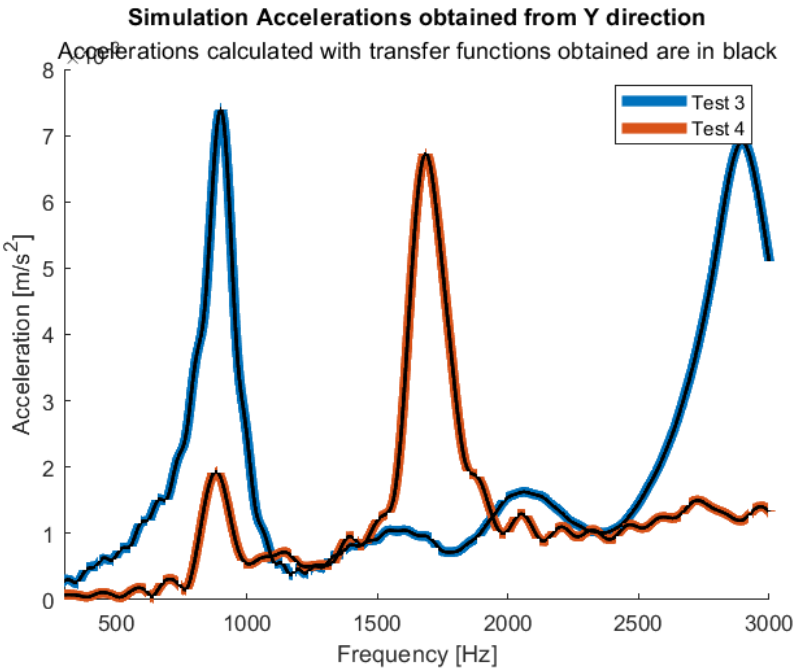

Figure 4.8 Simulation Accelerations Obtained from Y Direction (Two Dimensional FRF Calculation)

FRFs obtained with the method is provided in Figure 4.9 and Figure 4.10. The method is shown to be accurate for G_{xx} and in mode frequencies for other FRFs identified. Inaccuracies are observed in frequency points where reference FRFs have low amplitude compared to the same reference FRF at different frequency points. This is not a major problem as mode amplitudes and mode characteristics are the most important characteristics of FRF. FRFs obtained with the method at frequency domains where zero crossings (Figure 2.3) of force excitation resides are less accurate compared to the frequency domain where the force excitation is sufficient.

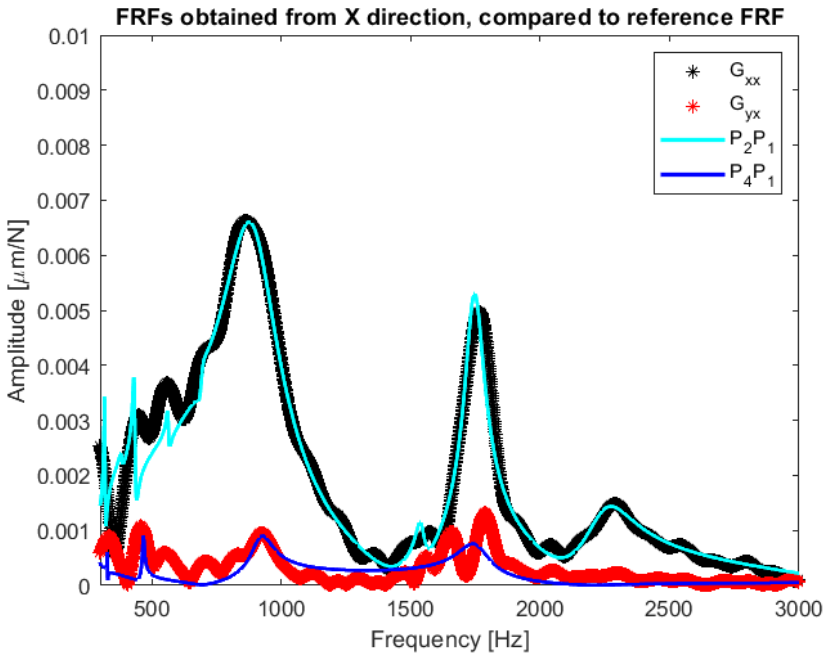

Figure 4.9 FRFs Obtained from X Direction, Compared to Reference FRF (Two Dimensional FRF Calculation)

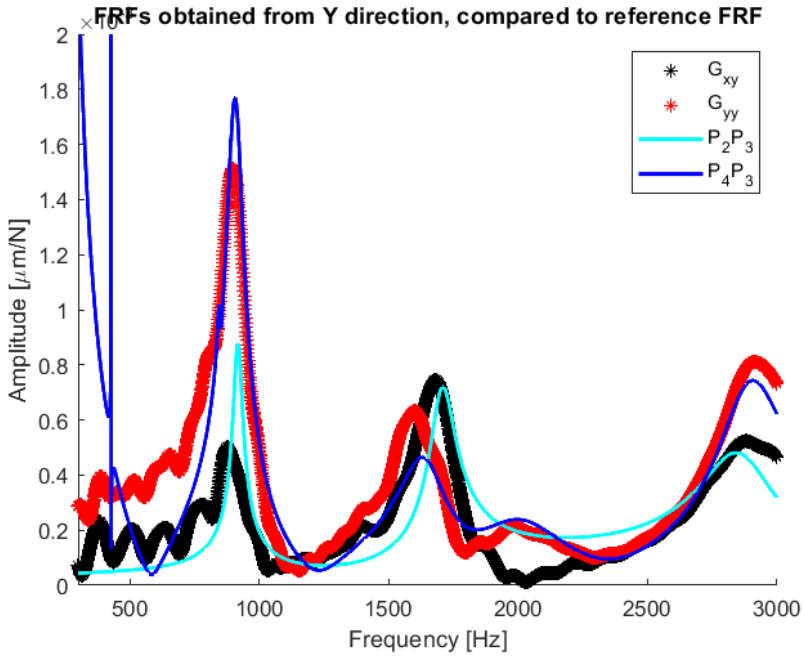

Figure 4.10 FRFs Obtained from Y Direction, Compared to Reference FRF (Two Dimensional FRF Calculation)

CHAPTER 5

EXPERIMENTS AND DISCUSSION

In this chapter, identification methods offered in this thesis are tested and confirmed with experimental data. These methods are demonstrated with simulation in their respective chapters and this chapter follows the same template offered with simulation, except practical considerations that had not been addressed are included here. Chapter 5.1 explains experimental setup and preparations. Chapter 5.2 gives calculation of force coefficients. Chapter 5.3 provides FRF identification.

5.1 Setup of the Experiment and FRFs to be Used for Identification

Starting with machine-tool, Deckel FP5CC, 5 axis CNC milling machine retrofitted with Beckhoff electronics was readily available for the process. A very important detail regarding this machine is that Y axis movement is controlled by spindle head and so Y-axis direction in table (where workpiece is placed) is very stiff compared to X direction of table. This makes omitting non-diagonal members of transfer function easier. Cutting tool used is EM90 63X6 022 EDPT 140408 (MBC cutting tools, Figure 5.2) which is a square shoulder face milling tool with 63.3 [mm] diameter (with inserts) placed on it. It allows 6 inserts but only one of them is used and neither the cutting tool nor insert has significant helix angle. Insert used is EDPX 140420-CKN20M (Rapid Maxtools).

Table 5-1: Test Format

Test:1,2,3,4	Sampling: 51200 [Hz]	Deckel FP5CC
D=63.3 [mm]	a_p=2.9 [mm]	Wall Depth=4 [mm]
Point 1 Accelerometer	Point 3 Accelerometer	Centered Workpiece
5.12 [mV/g]	10.23 [mV/g]	Insert: Single

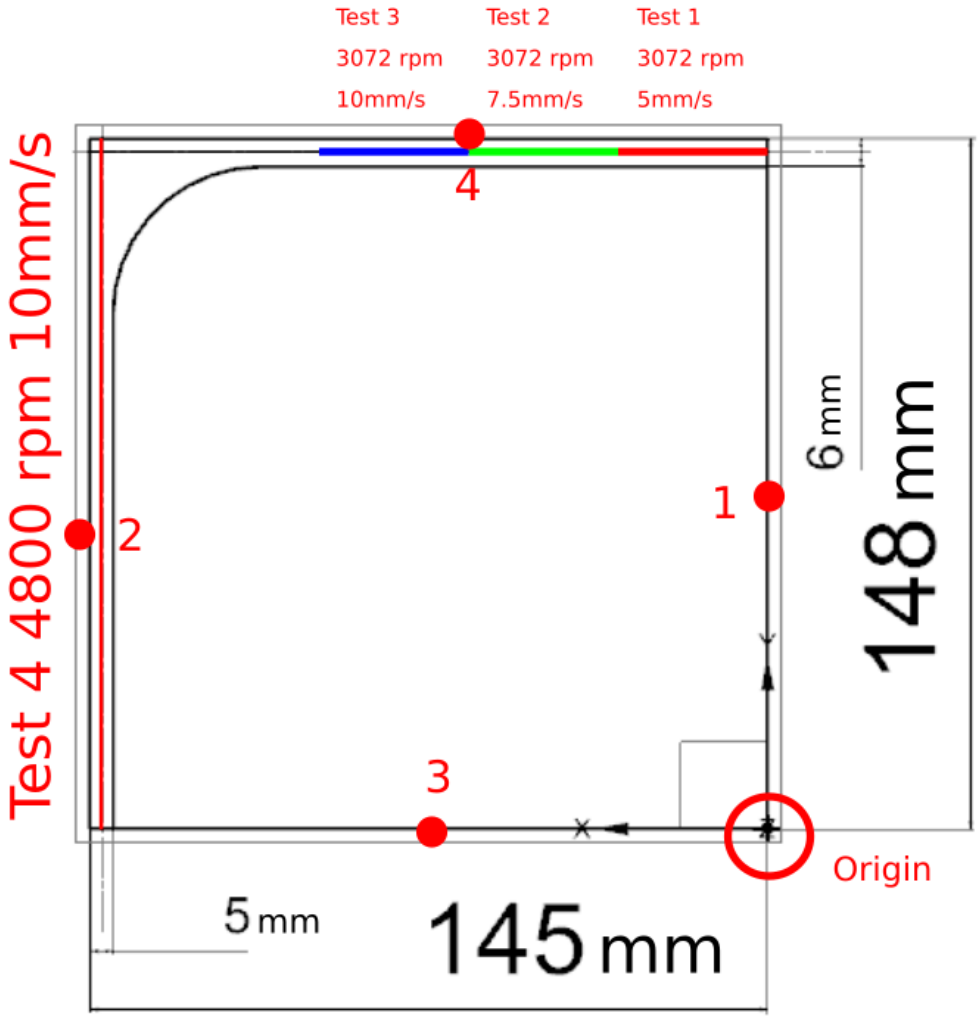

Figure 5.1 Identification Test: Accelerometers Points 1 and 3, Tap Test Spots 2 and 4; along with Test Positions

Measurement setup is the exact same on the Chapter 2. For refreshing the memory: As hammer, DYTRAN 5800B3T (Figure 2.5a) and as accelerometers at X and Y directions PCB 352C23 [5.12mV/g] and DYTRAN 3225F1 [10.23 mV/g] are used respectively. These accelerometers take data from single direction only. Regarding hammer, measurements have been shown to have coherence value consistently above 0.8 at frequency domain from 500 [Hz] to 3000 [Hz] which limits frequency domain to be analyzed. (Figure 5.5 and Figure 5.6) Data collection is done through NI 9234 processing card (Figure 2.5b). Figure 5.1 provides tool paths of tests with parameters varied between tests. Point 1 and 3 gives acceleration positions and points 2 and 4 gives tap test spots and Figure 5.2 gives a picture of the workpiece.

Figure 5.3 and Figure 5.4 provides tap test results. The same FRFs used in Chapter 2 are used in this chapter. For refreshing the memory: The results of machine tool structure mentioned above is obvious. As it is visible from Figure 5.3, P_4P_1, cross FRF representing XY direction is comparably lower than P_2P_1, FRF in XX direction. This same statement is not true for Y direction as in Figure 5.4, cross and diagonal FRFs (P_2P_3 vs. P_4P_3) are comparable to each other. P_2P_1 is the most significant FRF for table. Additional details are given in Appendix 1. Detailing workpiece, AL7075 aluminum alloy is the material workpiece is made of and Figure 5.1 and Figure 5.2 present the workpiece dimensions. 3 tests are performed. The first 3 tests are used for the identification of force coefficients and test 4 is used for FRF Identification. Conditions applying all tests are given in Table 5-1 and details regarding tests are presented in their related chapters, including design decisions on the workpiece regarding zero crossing and cutting path.

Figure 5.5, Figure 5.6 gives coherence examples. As it can be seen, cross FRF has comparably poor coherence values.

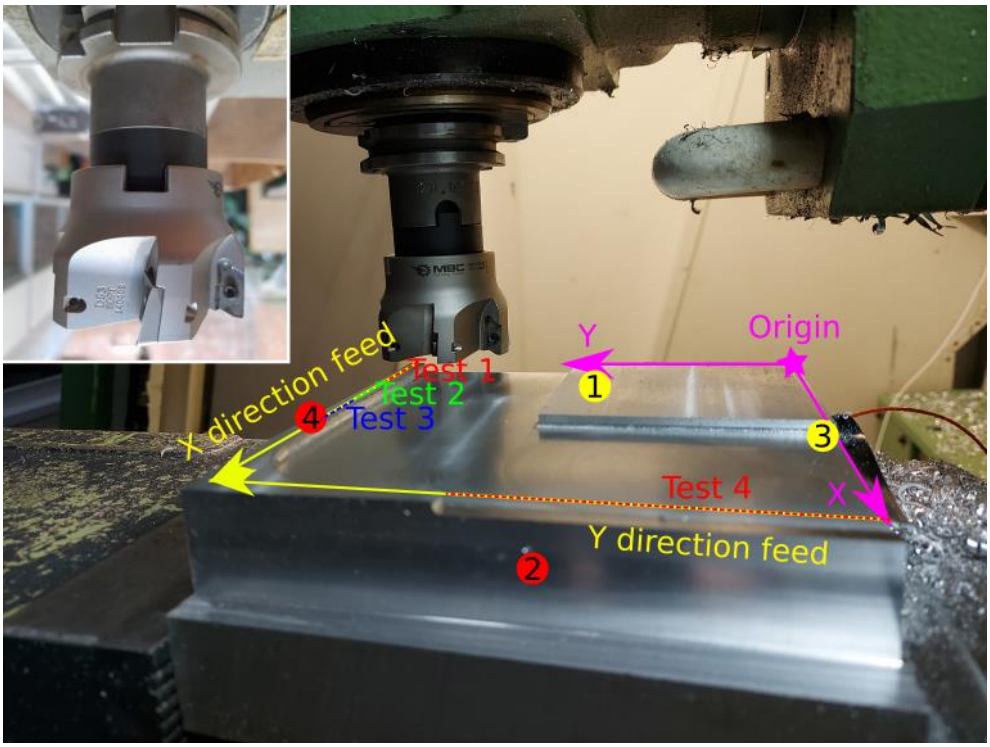

Figure 5.2 Workpiece and Cutting Tool

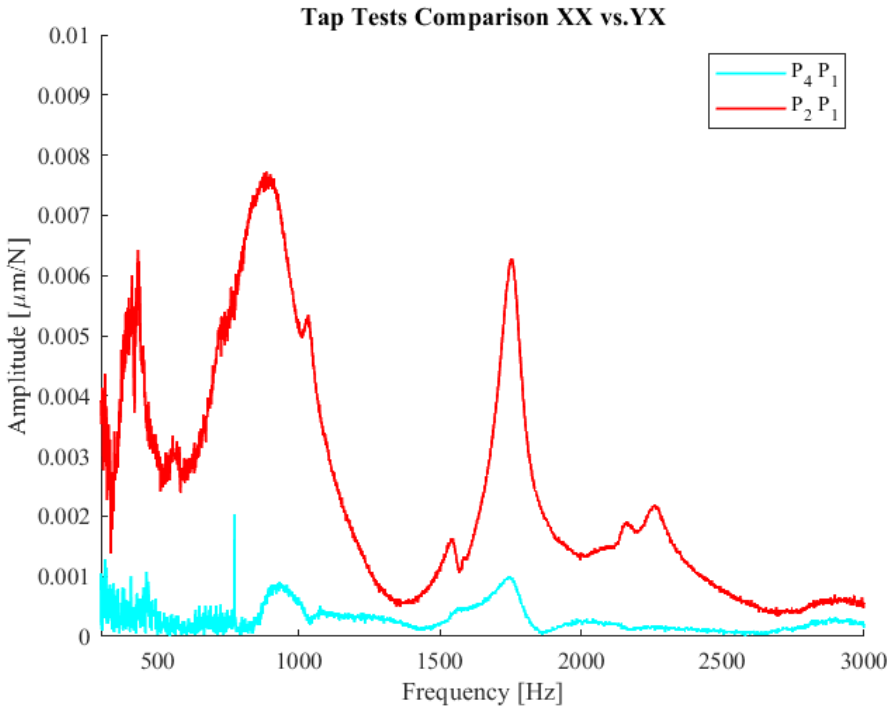

Figure 5.3 Tap Tests Comparison XX vs. YX

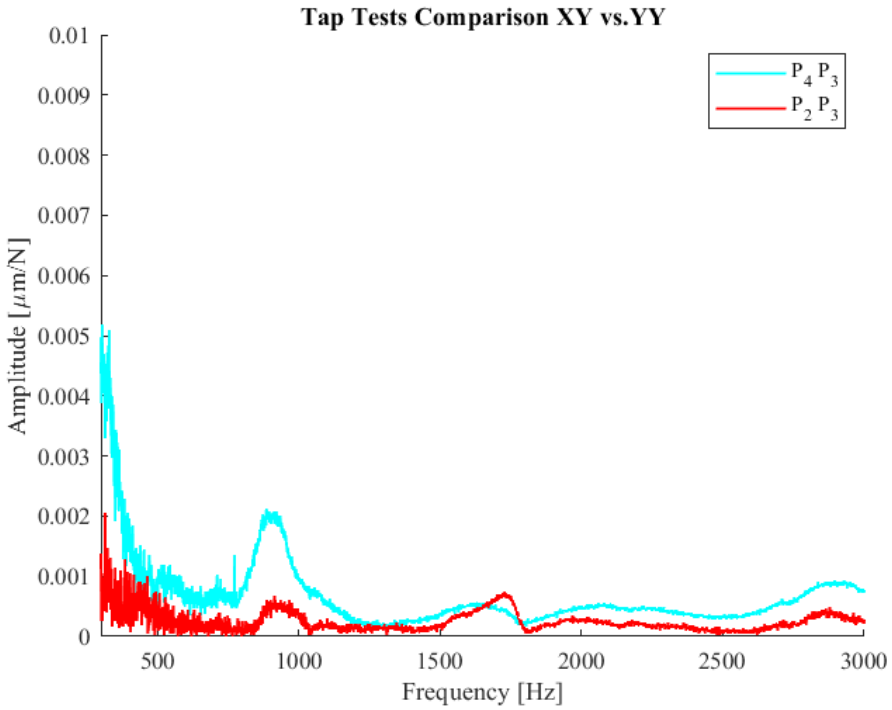

Figure 5.4 Tap Tests Comparison XY vs. YY

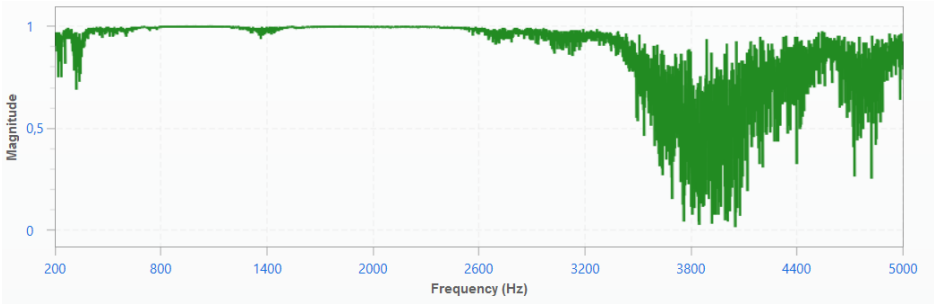

Figure 5.5 Coherence of XX

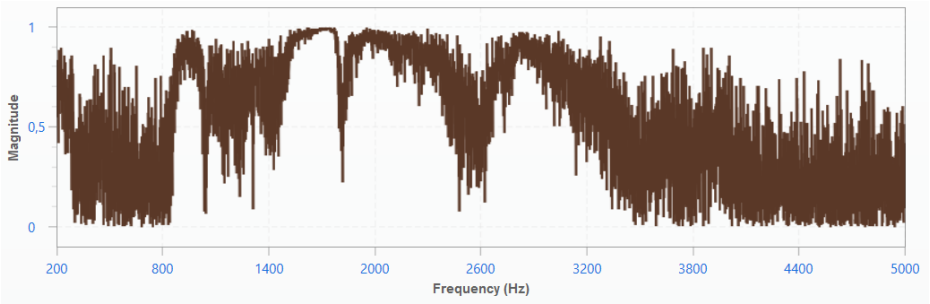

Figure 5.6 Coherence of YX

5.2 Calculation of Force Coefficients

Three tests that have been detailed in Figure 5.1 and detailed in Table 5-2 have been performed for force coefficients. As explained at Chapter 5.1, tap tests have been performed at two points on the table of machine-tool, representing X and Y directions. The placement of the table was as close as possible to the cutting tool for representing cutting conditions accurately because FRFs are expected to be position dependent. Figure 5.1 and Figure 5.2 give the workpiece and tap test points. Despite knowing the fact that FRFs can be position dependent, a single tap test point from one Cartesian side is utilized for directional reference. This is because tap tests from previous experiments have already shown that the distance travelled during the experiment is not enough to change transfer functions significantly at the frequency domain of 500 to 1500 [Hz] in X direction (Appendix 1). This frequency domain is selected for identification of force coefficients due to multiple reasons, the first one being already mentioned in the previous sentence. Amplitude of FRFs at lower frequency domain show vast difference between operational transfer function (transfer function of the machine-tool (table-workpiece) during operation) and tap test results. This is not necessarily a problem for the application of the method offered here but for confirmation of the method, frequency domain that the tap test offers good coherence must be used. Amplitude of FRFs at frequencies higher than 5000 [Hz] during operation show local variations in amplitude based on proximity to the accelerometer and just like low frequencies, tap test returns poor coherence for such high frequency domain. The frequency domain of 1500-3000 [Hz] is where it is expected to find regional variations as previous tap tests indicated and this frequency domain that the method offered in this thesis reveals. 500-1500 [Hz] frequency domain has none of these issues while it gives a dominant mode on Figure 5.3 and it is still a frequency domain where force excitation can be adjusted to be as high in all tests (…which is determined by milling process parameters but this frequency domain can be comfortably excited).

Table 5-2: Test Parameters of Identification of Force Coefficients, D=63.3 [mm], a_p=2.9 [mm], Wall Depth=4 [mm]

Test	V_x [mm/min]	n_s [rpm]	L [mm]	Sample Position [mm]	Sample Length [mm]	Workpiece Type
1	300	3072	6	20	1	Centered
2	450	3072	6	20	1	Centered
3	600	3072	6	20	1	Centered

In Table 5-2, angular speed and feed parameters are selected to obtain different static chip thickness values since in order to apply equations (3.28) and (3.29) multiple chip thickness values are needed. The zero crossing value which is calculated with equation (2.11) is 3181 [Hz] for the first three tests and this is sufficient for 3000 [Hz] maximum value for frequency domain that is determined by the researchers with the help of tap tests as shown in coherence graphs. During the first 3 tests, the cutting tool center has travelled 32 [mm] in each test. This value is longer than sufficient enough for dynamic chip thickness to disappear which it is expected to happen in first couple impacts. The estimation of dynamic chip thickness disappearing is a conservative estimation as the exact process parameters are used for Chapter 2 and dynamic chip thickness disappeared. This is one of the purposes of simulation. The sample position is taken as 20 [mm] from the start of every individual test and a region of 1 [mm] has selected for sampling. Ideally, less distance from the start and less total cutting distance could be used to keep the identification region minimal but as mentioned in the previous paragraph, the frequency domain of 500-1500 [Hz] offers stable known FRF. Wall depth is constant and higher than axial depth, which is also constant.

Results of application of identification of force coefficients are provided below. Step E of identification of force coefficients is shown with test 3 data in Figure 5.7. Force estimations are calculated according to equation (3.3) for every engagement sampled, as numbered from 1 to 8. With progressing recursive least squares method,

$K_{A,i}$ are calculated according to equation (3.26) and $K_{A,i}$ are used for force curvefit. As it can be seen in the figure, there are variations even between consecutive force estimations and this shows one small benefit of recursive least squares application as it allows observing such variations, even though it evens out eventually. One drawback is that force estimations around a frequency domain closer to 500 [Hz] does not necessarily keep the trend of force curvefit. This is an undesirable situation as the force calculation does not reflect force estimation for this region. However, this situation is not evidence against the method because multitude of reasons such as poor tap test results to poor signal-to-noise ratio and low excitation can cause such issues. In this case, amplitude of FRFs at given the frequency domain is small and so signal to noise ratio can be expected to be poor.

Sampled engagements obtained from Figure 5.7 are as shown in Figure 5.9. Acceleration data at Figure 5.9 has been used to obtain force estimations of Figure 5.7. Figure 5.9 is equivalent to Step E of FRF Identification method given at Chapter 4.1, with the exception that force at every engagement was calculated with $K_{A,i}$ instead of a single value through.

This can be seen from the figure as the amplitude of force at every engagement is different. Another important point to be seen is that as mentioned several times before amplitude of acceleration dampens out quickly and there is very limited background noise, which both necessary for the quality of results are being sufficient. For all coefficients at all tests, Figure 5.8 gives recursive calculation of $(K_{A,i}, K_{B,i})$ for all 3 tests. As it is shown in Figure 5.8, $(K_{A,i}, K_{B,i})$ converges into a value.

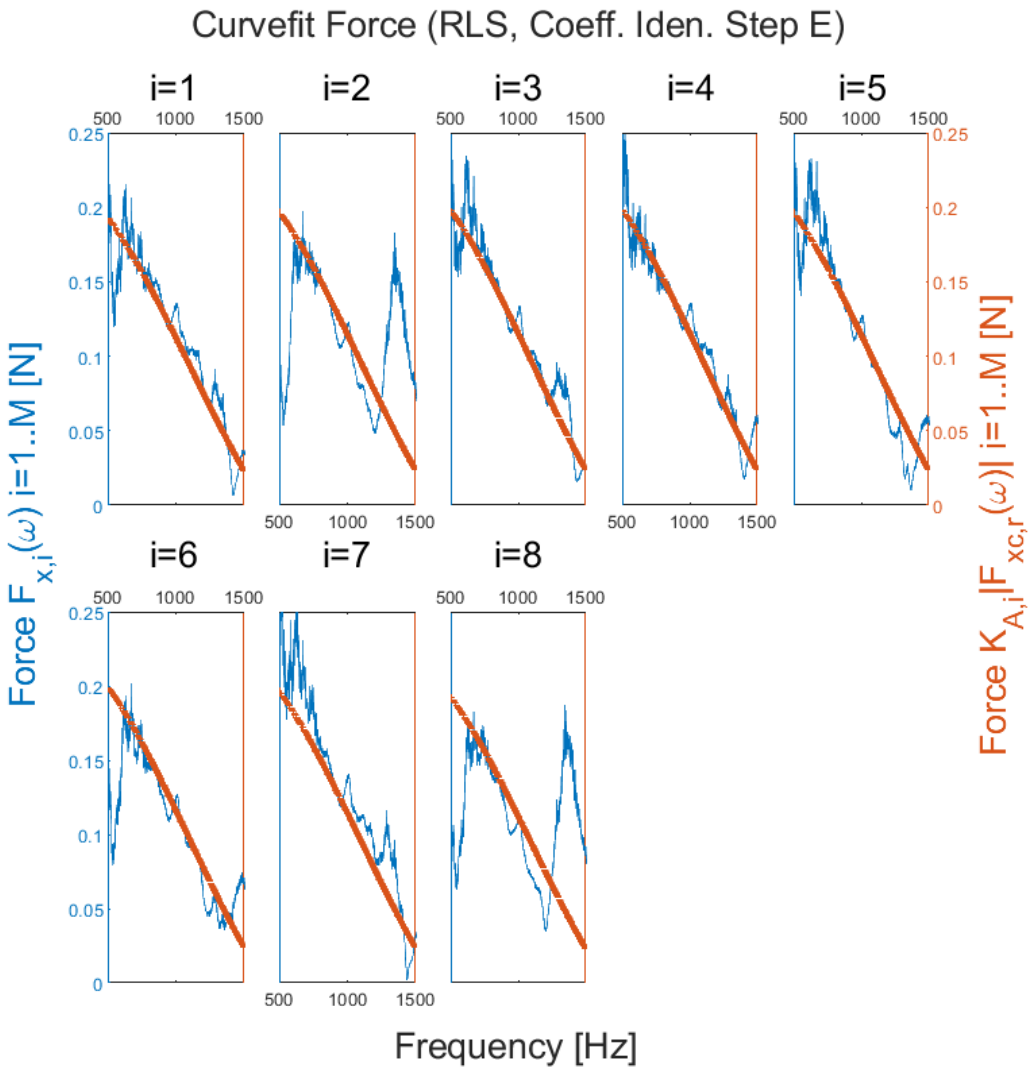

Figure 5.7 Test 3, Recursive Least Squares Application of Calculating $K_{A,i}$ (Real Data Version of Step E of Calculation of Force Coefficients From Chapter 3.3)

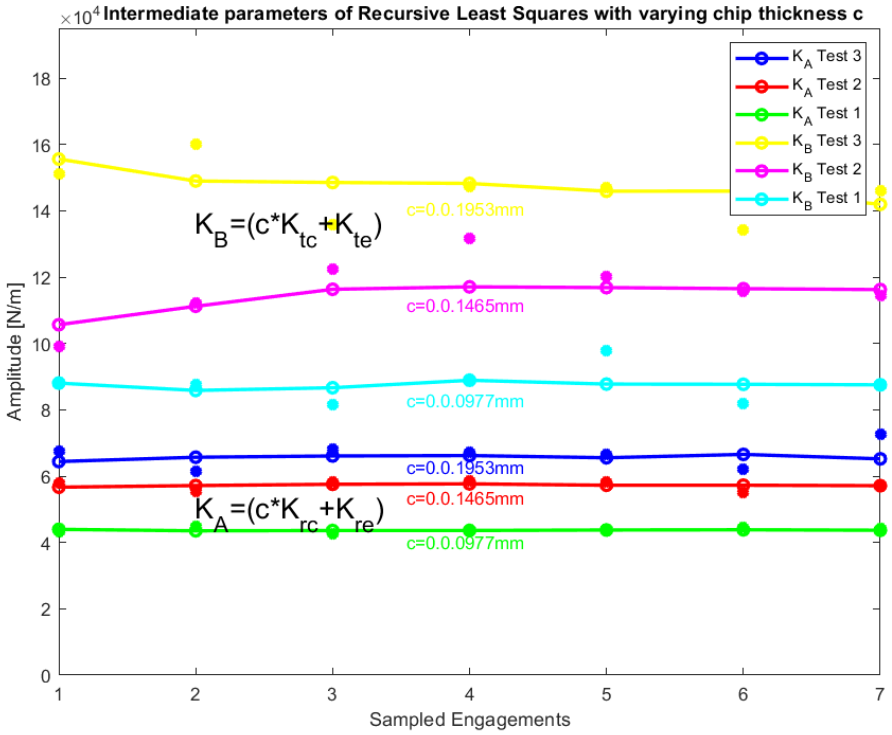

Figure 5.8 Variations of Force Coefficients during Recursive Least Squares

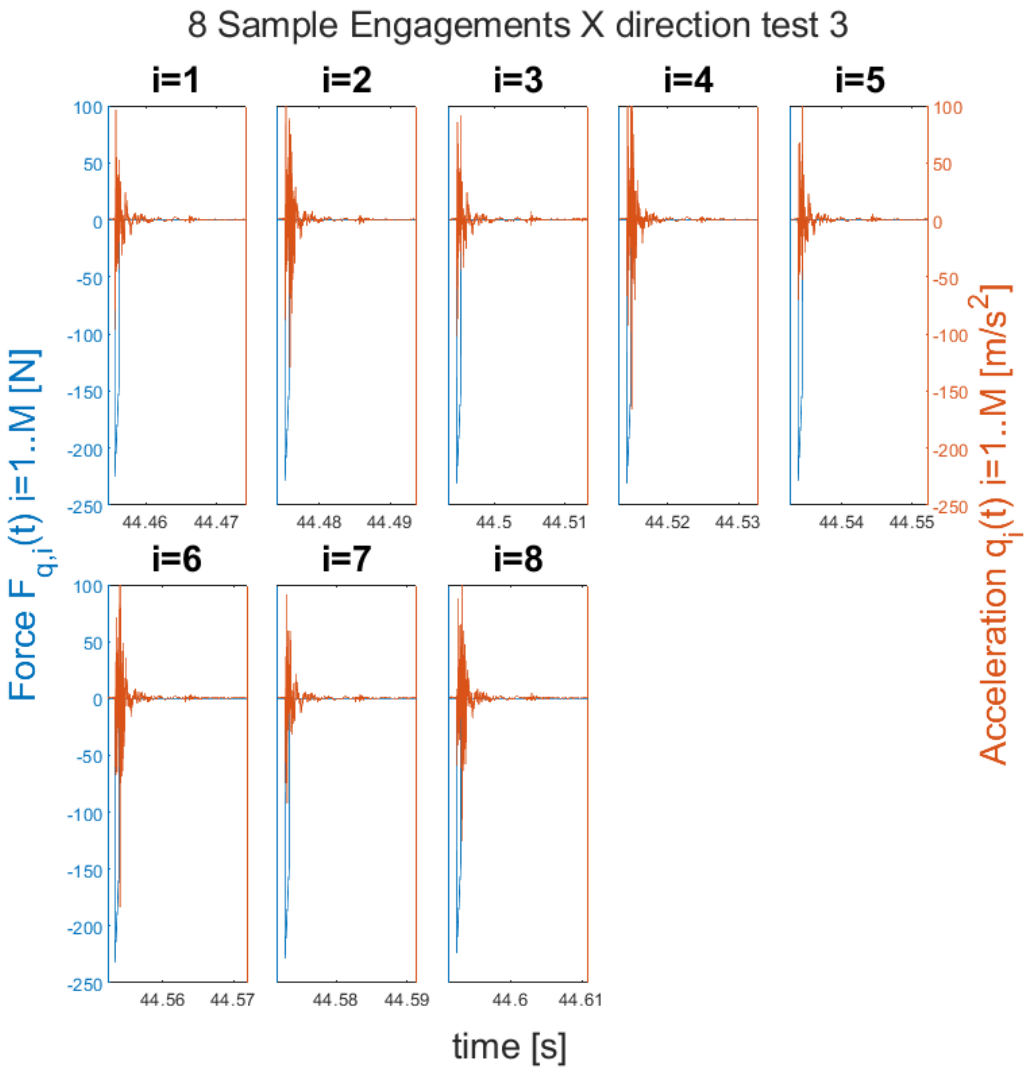

Figure 5.9 7 Engagements Sampled from X direction Test 3 (FRF Identification Step E)

Intermediate force coefficients obtained with a single sampled engagement instead of recursive least squares are also provided in the figure as individual stars. This indicates a variation of force coefficients.

Table 5-3: Intermediate Force Coefficients Identified

	Recursive Least Squares Output	
Test	**K_B [N/m]**	**K_A [N/m]**
1	87.03e3	43.62e3
2	116.50e3	57.25e3
3	145.92e3	66.54e3

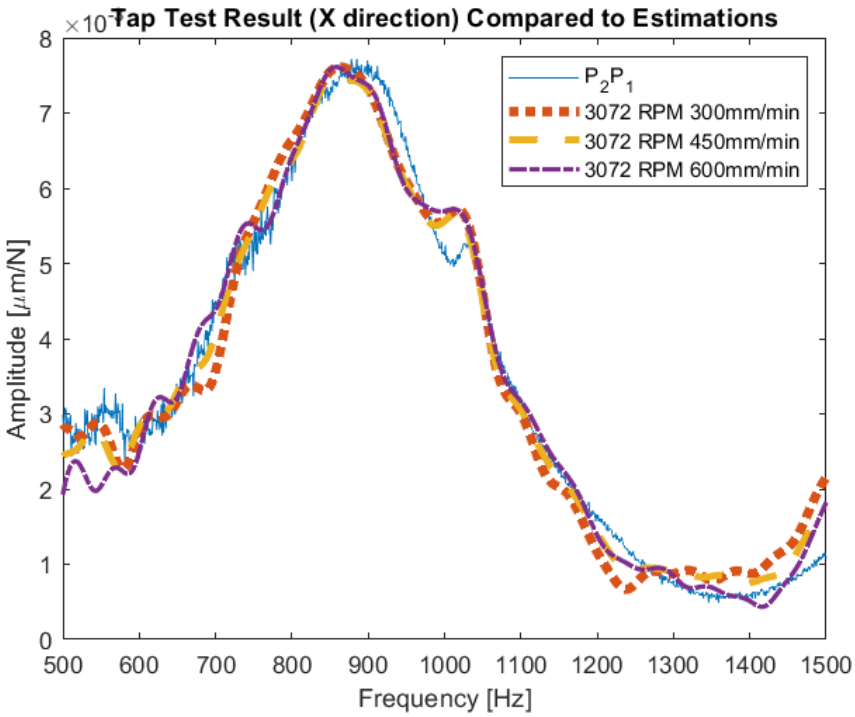

Figure 5.10 Tap Test Result (X Direction) Compared to FRF Identification

If what is shown in two figures (Figure 5.7 and Figure 5.9) above and recursive least squares calculation shown in Chapter 3 are applied for the first 3 tests, Table 5-3 gives identified K_A and K_B for every test. Values on this table are simply the end value of the previous table as the end result of recursive least squares method is taken

as final value of K_A and K_B. As it is expected, chip thickness being smaller results in larger values for K_A and K_B.

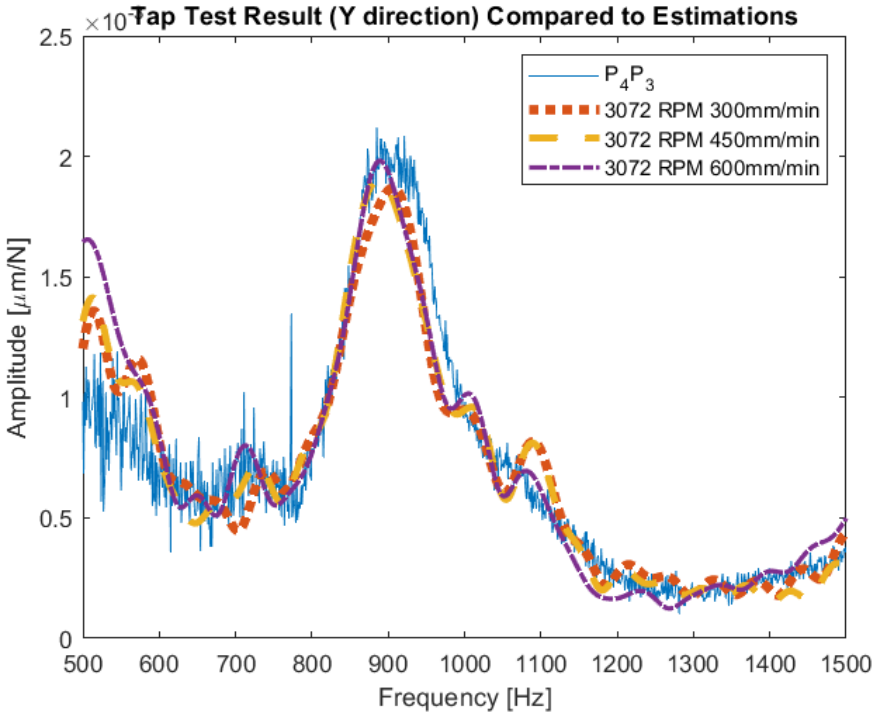

Figure 5.11 Tap Test Result (Y Direction) Compared to FRF Identification

Resulting FRF Identification outputs (FRFs identified by obtaining Step E of FRF Identification method as shown in Figure 5.9 for every test and applying a suitable FRF calculation method like it is suggested at equations (4.1) to (4.4) while at the same time applying K_A and K_B as K_{tc} and K_{rc} respectively) can be seen in Figure 5.10 and Figure 5.11. These figures function as quality control.

Three tests with different chip thickness values offered 3 sets of K_A and K_B. Using equation (3.28) and (3.29), force coefficients are identified as Table 5-4**. These force coefficients are used for simulation throughout the entire thesis.** These force coefficients are final. This value can be compared to values obtained from the literature [16].

Table 5-4: The Identified Force Coefficients (Cross FRF Omitted)

K_{tc}=603 [MPa]	K_{rc}=244.21 [MPa]
K_{te}=28.15 [kN/m]	K_{re}=20.08 [kN/m]

If cross FRFs are not omitted, results slightly shift for coefficients obtained from X direction change more significantly for Y direction. However, the values obtained are larger.

Table 5-5: The Identified Force Coefficients (Cross FRF Included)

K_{tc} =666 [MPa]	K_{rc} =254.85 [MPa]
K_{te} =35.12 [kN/m]	K_{re} =20.51 [kN/m]

Table 5-6 gives a set of force coefficients taken from a milling force review paper [6]. It is seen that the values found in this thesis are comparable to the results of the research papers. It should be noted that some of the listed research papers experiment with extreme conditions such as composite material and very small chip thickness.

Table 5-6 A Set of Force Coefficients from [6]

Cutter Material	**Lubrication**	**Workpiece**	**K_{tc} [MPa]**	**K_{te} [kN/m]**	**K_{rc} [MPa]**	**K_{re} [kN/m]**
Cemented Carbide	Dry	AL7075-T6	767.01	27.7	168.80	26.6
			600.46	17.9	180.96	20.42
High Speed Steel		AL7075	951.36	11.11	262.59	11.31
Cemented Carbide			1319.4	19.65	788.83	26.77

5.3 FRF Identification

Force coefficients obtained are utilized for FRF identification with test 4. The tool path of test 4 is shown in Figure 5.1. Table 5-7 provides process parameters of the

test.Some important decision factors must be listed. A long path in Y direction at a different side of workpiece is selected to achieve position dependent difference in FRF and to display the effectiveness of the method by applying it at a different spot than where force coefficients are identified. Process parameters are selected to be close to the process parameters in which force coefficients are identified. The only major difference is that angular speed is increased to identify a wider frequency domain. For confirmation purposes, a tap test comparison is performed but there is no reason to stick to frequency domain where force coefficients are identified. Force coefficients obtained can be used outside of the frequency domain where tap tests are used. The experiment setup has not changed from the first three tests to keep variations to a minimum. The same cutting tool, workpiece and the same accelerometer positions are utilized.

Table 5-7: Test Parameters of FRF Identification, D=63.3 [mm], a_p=2.9 [mm], Wall Depth=4 [mm]

Test	**V_y [mm/min]**	**n_s [rpm]**	**Wall Thickness [mm]**	**Sample Position [mm]**	**Sample Length [mm]**	**Workpiece Type**
4	600	4800	5	10,70,140	1	Centered

For identification, X direction is selected because as mentioned in Chapter 2 and Chapter 5.1, the table in this direction is significantly less rigid compared to Y direction and non-diagonal members of transfer function ($G_{yx}(s)$ compared to $G_{xx}(s)$ vs.$G_{xy}(s)$ compared to $G_{yy}(s)$). (Figure 5.3) As visible on Table 5-7, 3 regions are selected for sampling from this test, considering that distance can show the change of transfer function with distance, demonstrating the method and its advantages.

By utilizing workpiece length and feed per insert, around length over feed per insert engagements sampled are expected. This value is equal to 1184 for 4800 [rpm] and they are all at different spots. This is a significantly high number compared to tap

tests or shakers. However, due to both variations at the initial position of the workpiece, given tolerances, variations at the angular position and angular speed of cutting tool, an accurate value of contact time cannot be reliably calculated to express the entire frequency measurement domain, which is 25600 [Hz] (half of the sampling rate). This is where placing force calculation to the time where acceleration exceeds a certain value is critical as this method automatically handles the problem of force timing.

The cutting distance of test 4 is 148 [mm]. In this 148 [mm] distance the cutting tool has taken, the data that are obtained from cutting first 10 and last 7 [mm] of the cutting path is rejected for eliminating possible transient effects and from the rest of the data, mentioned 3 desired regions are sampled. Both force calculations and acceleration measurements has been zero padded to reach 1 [Hz] frequency resolution. Finally, FRF identification method has been applied.

Step E from Chapter 4.1 is visualized with experiment data as shown in Figure 5.12. 9 sampled engagements obtained from 10-11 [mm] region from 148 [mm] tool path during test 4 are given in the figure for demonstration purposes. Acceleration has been measured during cutting, data is sampled according to the angular speed of cutting tool and synchronization has been utilized for matching force calculations to accelerations measured. Data and force estimation are zero padded to reach 1 [Hz] in frequency domain.

After obtaining the results shown in Figure 5.12, any method applicable to multiple tap test measurements can be used for this case. Equations from (4.1) to (4.4) explain the method for this thesis.

Figure 5.14 gives FRF identification results together with P_2P_1 tap test results as a reference and Figure 5.13 gives the coherence value of identified FRFs. Coherence values are consistently higher than 0.8 for the given frequency domain. Tap test results and FRF identification outputs match quite well, except for the frequency domain that changes which is between 1500-2000 [Hz] domain.

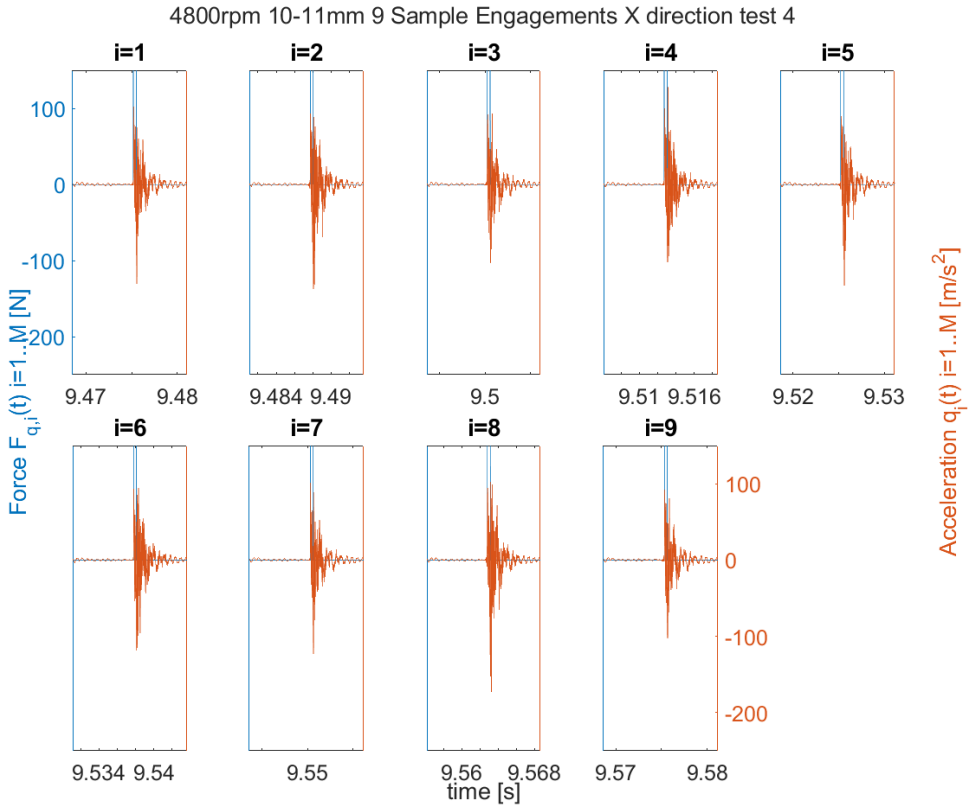

Figure 5.12 FRF Identification Step E with Real Data. (Test 4, 4800 rpm and 10-11 [mm] Sampled Tool Path)

The amplitude of FRF at the frequency domain between 1500-2000 [Hz] domain shows variations among the path and these variations are visible in Figure 5.14 to Figure 5.16. Figure 5.15 shows that during the experiment, the amplitude of FRF in this frequency domain changes more than amplitudes of FRF at any other frequency domain. Figure 5.16 shows that local FRF identification results match with their respective tap test results (Appendix 1). This means that not just the method accurately predicts FRF, but it also detects local variations.

Finally, for estimations offered at Figure 5.16, batch-size error criterias can be applied.

Table 5-8: Batch-Size Error Criteria Calculations

	RMSD	SMAPE
Measurement 4	3.3e4	0.0013
Measurement 8	4.7e4	0.0019

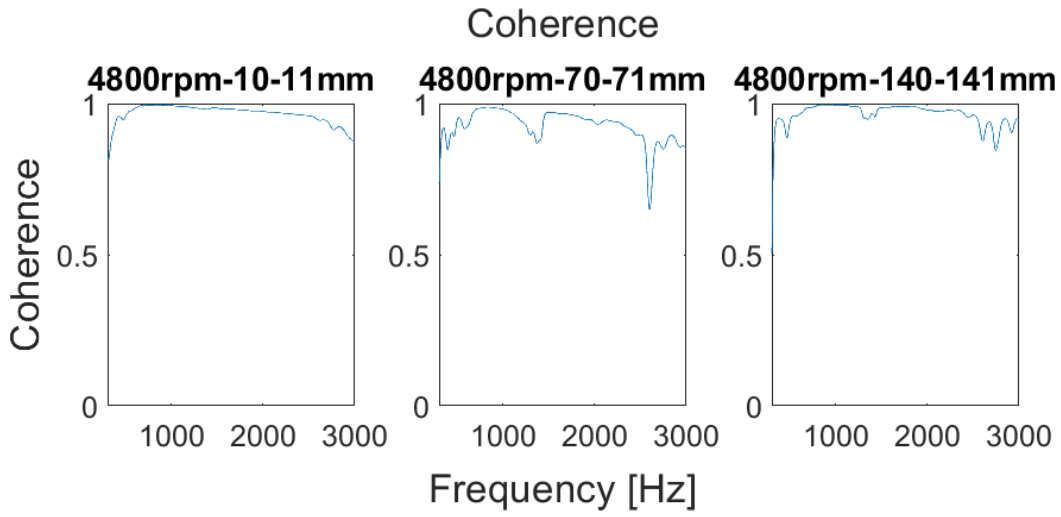

Figure 5.13 Coherence Values of Identified FRFs

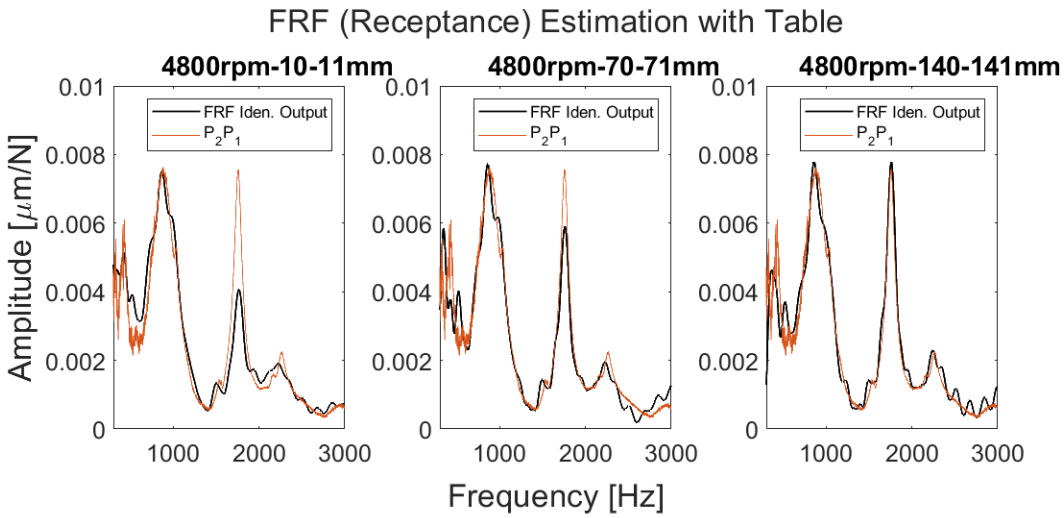

Figure 5.14 FRF Identification Results of Selected Regions

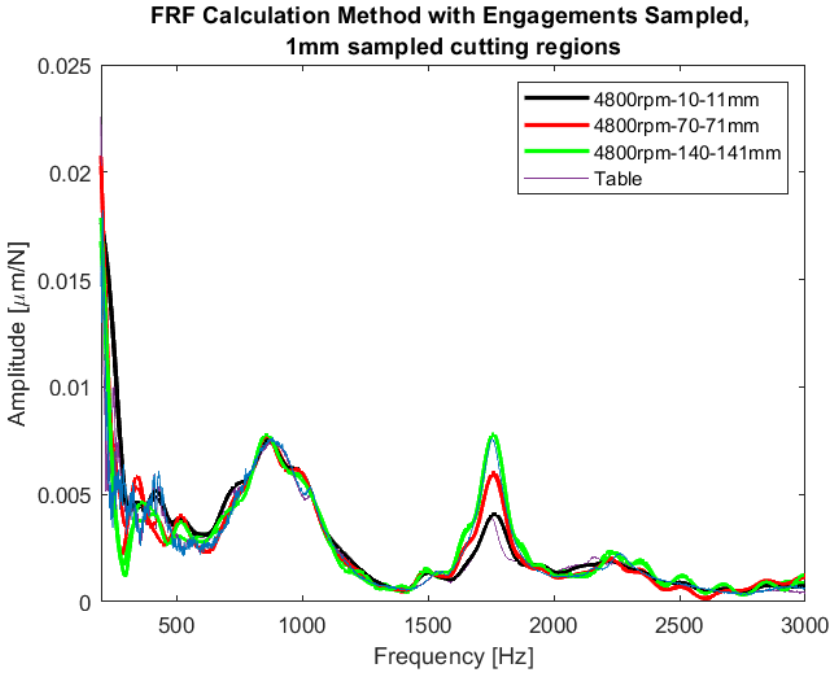

Figure 5.15 FRF Identification Results Compared on Top of Each Other

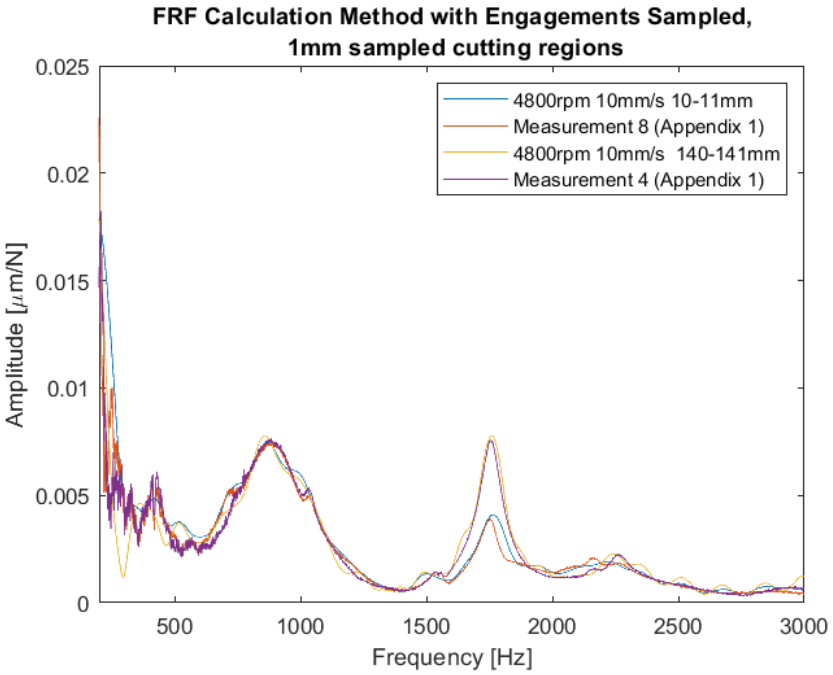

Figure 5.16 FRF Identification Results With Tap Tests of The Same Position (Appendix 1)

5.4 Two Dimensional FRF Identification

Just like in Chapter 4, two tests on close proximity has been selected for two dimensional FRF identification.

Table 5-9: Test Parameters of Two Dimensional FRF Identification, D=63.3 [mm], a_p=2.9 [mm], Wall Depth=4 [mm]

Test	V [mm/min]	n_s [rpm]	Wall Thickness [mm]	Sample Position [mm]	Sample Length [mm]	Workpiece Type
3	600 (X)	3072	6	20	1	Centered
4	600 (Y)	4800	5	140	1	Centered

Starting from force profile, force calculations representing force excitation are given below:

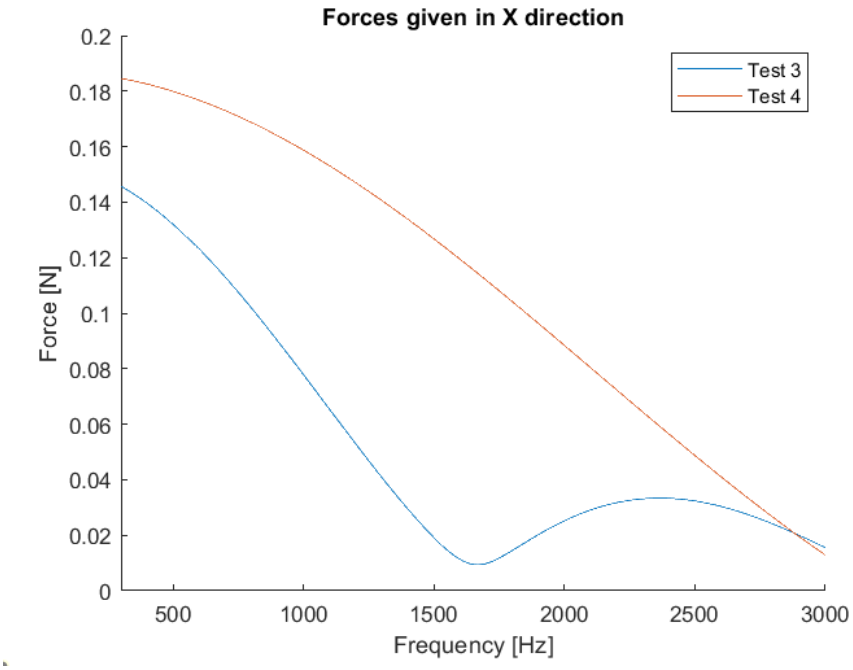

Figure 5.17 Forces Given in X Direction (Experiment, Test 3 and 4)

Different than simulation, there is a variation between acceleration measurements sampled as shown below. Figure 5.22 returns wildly various acceleration measurements.

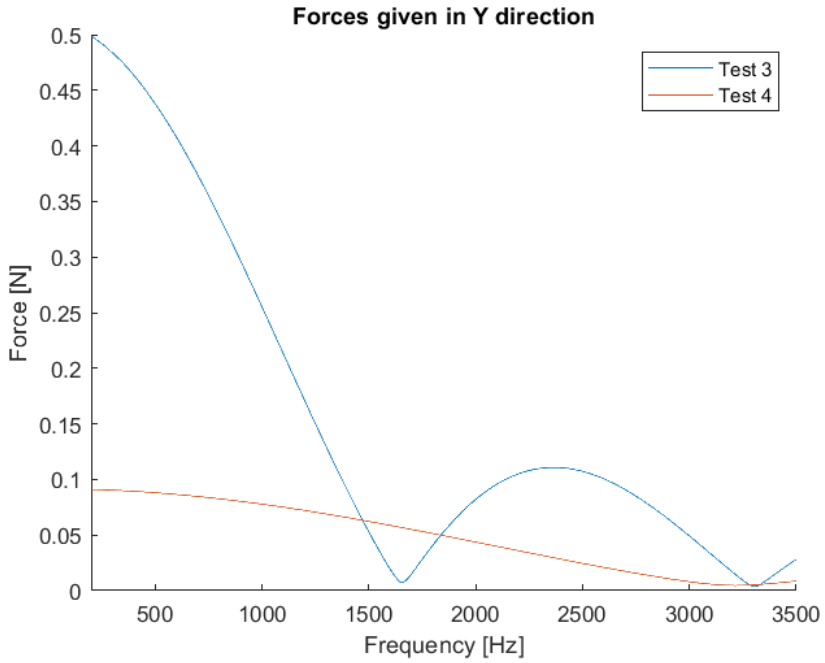

Figure 5.18 Forces Given in Y Direction (Experiment, Test 3 and 4)

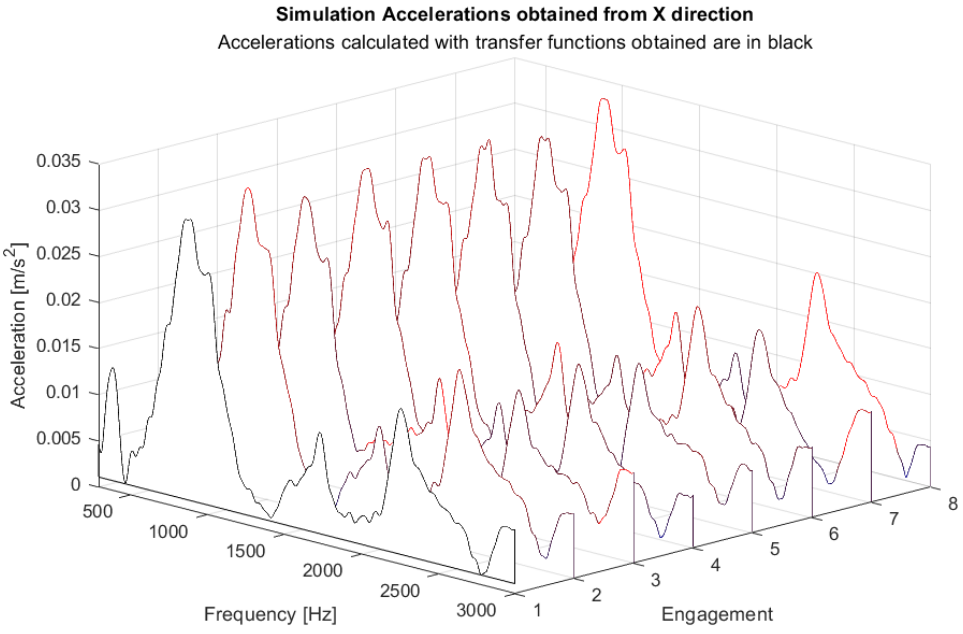

Figure 5.19 Acceleration Sampled from Test 3, X Direction

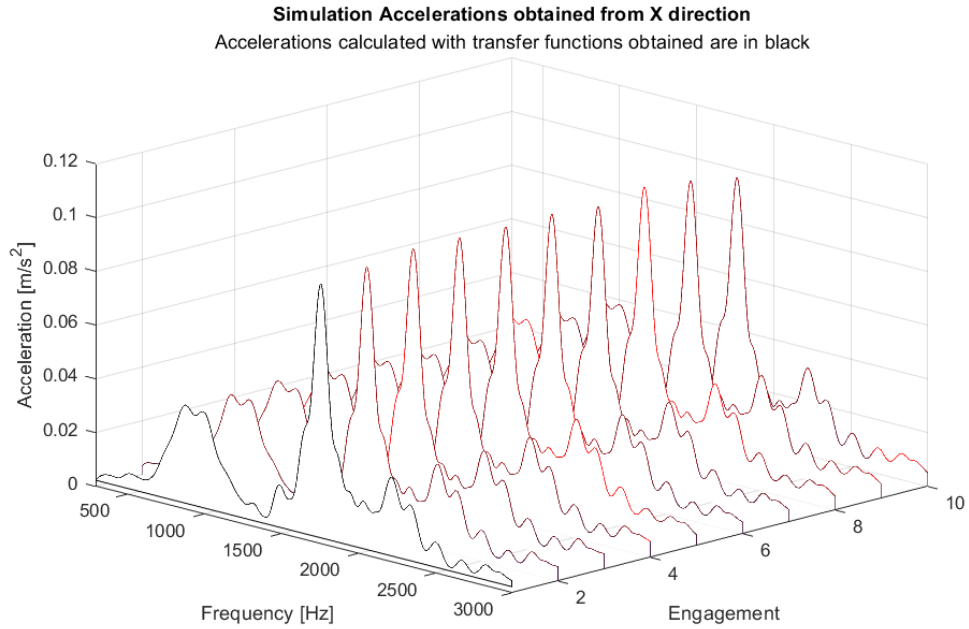

Figure 5.20 Acceleration Sampled from Test 4, X Direction

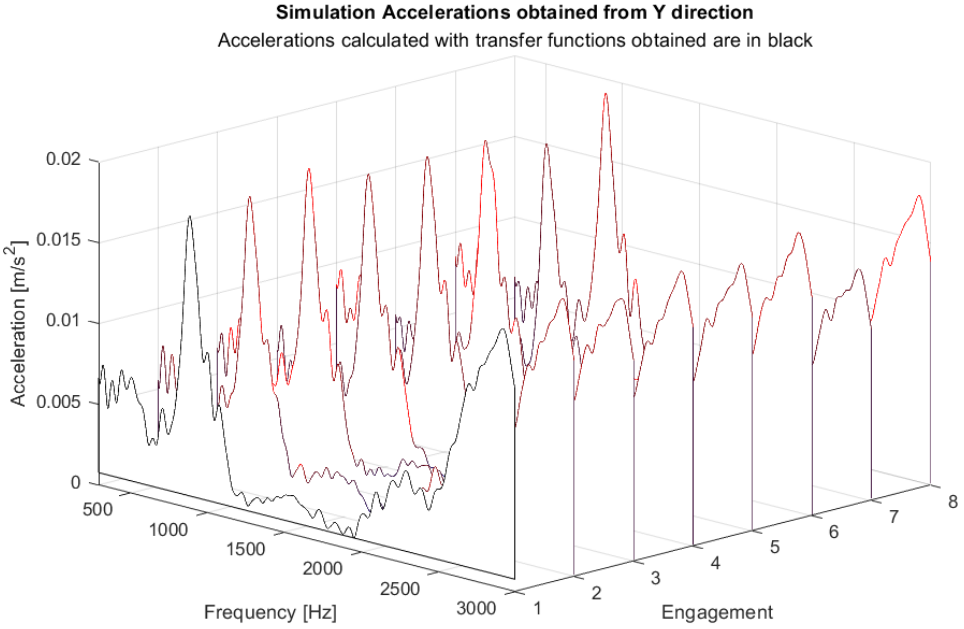

Figure 5.21 Acceleration Sampled from Test 3, Y Direction

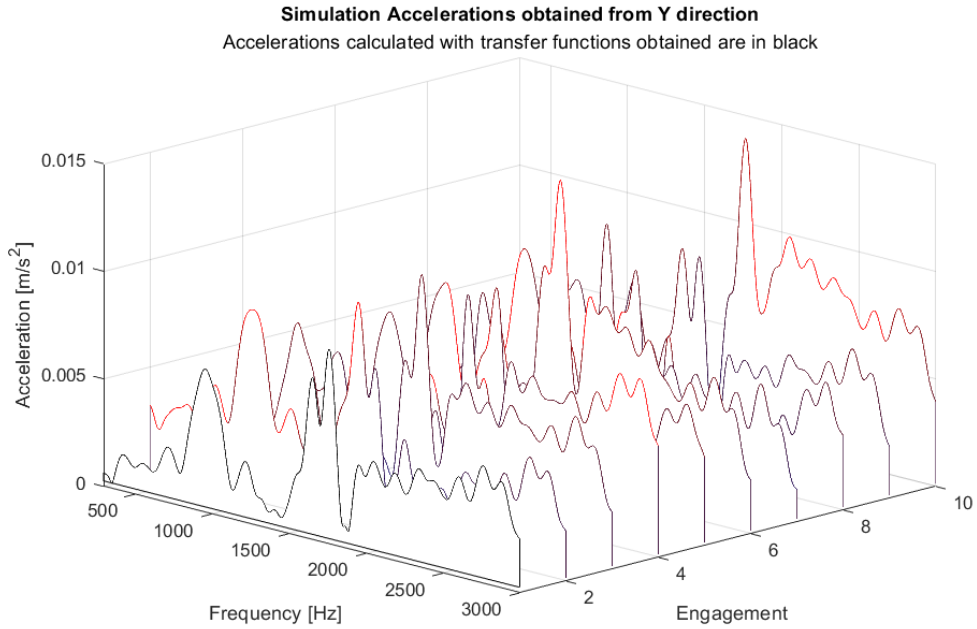

Figure 5.22 Acceleration Sampled from Test 4, Y Direction

As expected, zero crossings become a problem during identification as shown in Figure 5.23. Even though this problem did not appear in the simulation, it appears in experimental data, as any uncertainty in transfer functions results in dividing by a small number during FRF identification. 1550 [Hz]-1700 [Hz] frequency domain has been removed from frequency domain of identification and the process is repeated.

Figure 5.24 and Figure 5.25 provide the results. Unfortunately, the identification results cross FRFs are only correct in amplitude and some modes for G_{xy} and only for amplitude for G_{yx}. The rest of the results are accurate and G_{yy} is obtained fairly successfully for frequency domain under 1550 [Hz].

Results can be used for identification of dominant FRF like the one dimensional method offered in the previous section and it is a good measurement stick for checking how significant cross FRF are. Most of the problem can be attributed to the results in Figure 5.22 given its significant variation.

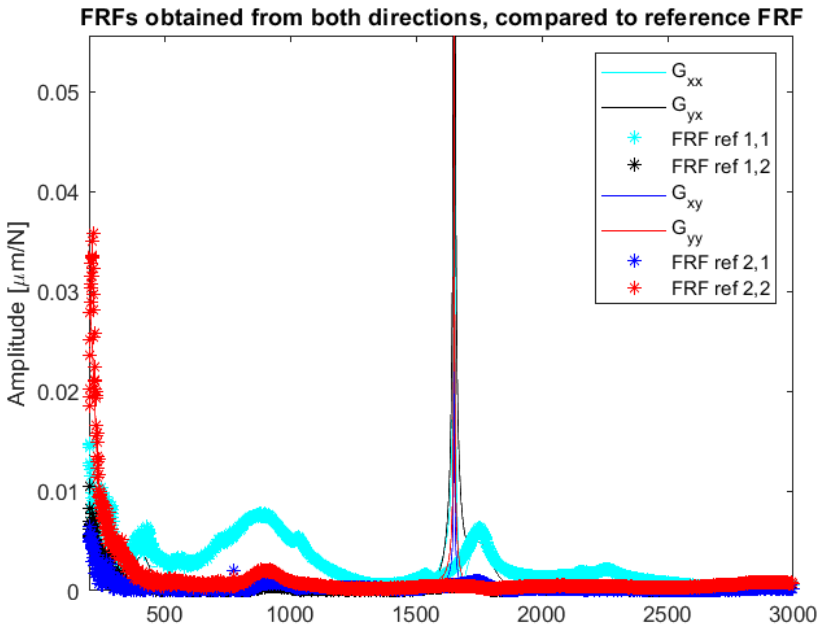

Figure 5.23 Passing Zero Crossing Returns Peaks with Very High Amplitude.

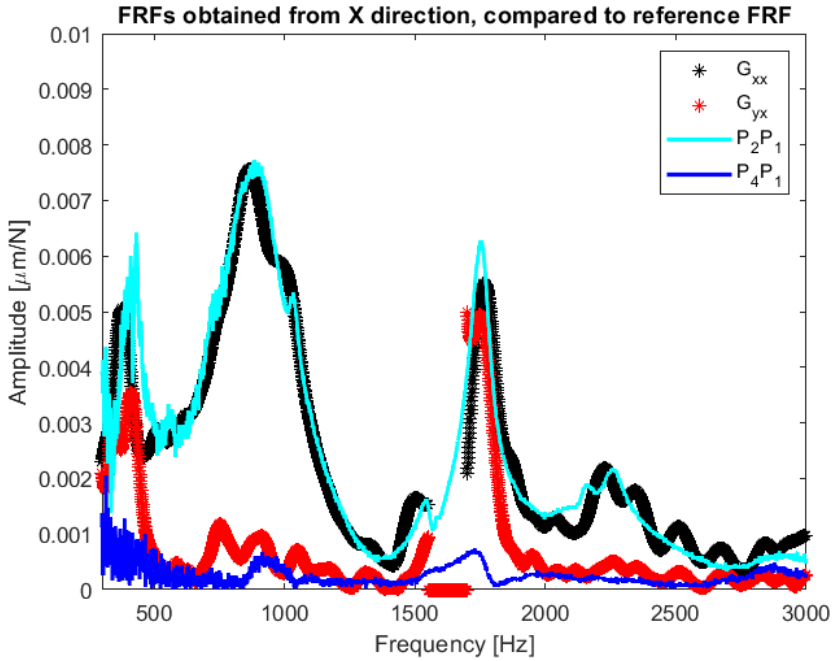

Figure 5.24 FRFs Obtained from X Direction, Two Dimensional FRF Identification

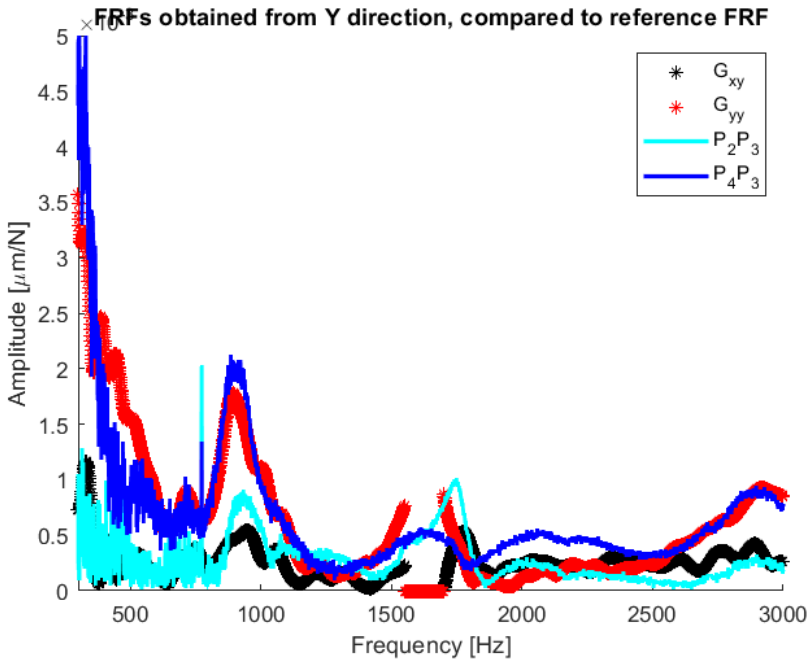

Figure 5.25 FRFs Obtained from Y Direction, Two Dimensional FRF Identification

CHAPTER 6

CONCLUSION AND FUTURE WORK

The method offered in this thesis has been confirmed to be useful for obtaining FRF at different spots accurately compared to tap tests, proving the approach, while still keeping mentioned advantages. Cutting parameters were selected for the machine-tool table-workpiece to be excited in the analyzed frequency domain. Identification of force coefficients has been performed by a selected region with consistent FRF and accuracy of force coefficients has been shown to compare acceleration results. More than 1000 tool contact separated into cutting path has been performed and they are combined in various regions and local identification of FRF has been performed. These results were achieved without a dynamometer and without initial knowledge of the material. As long as the same material is used, the same force coefficients can be applied without another tap test. A major possible advantage is that the method offers on-operation identification which allows for analysis of differences between operation conditions and tests done outside of the operation. This means that if machine transfer functions change during operation, the results obtained here can be more accurate than tap tests when the machine is not operational. Two dimensional identification did not offer the same accuracy that was expected by observing simulation results. However, it has successfully shown how critical cross FRF are for machines with unclear stiffness difference for Cartesian directions.

The advantages listed above are also present in many other methods mentioned in the introduction. However, this method does not need white noise and gives the shape and amplitude of FRF without additional assumptions such as mode frequencies or modal shapes. However, this method needs additional work for

accurate identification of mode parameters if they are desired because short window time is a limit for frequency resolution.

One important factor is that this method works with the assumption that the force model is correct. This is satisfied quite easily if the material type is known, cutting tool is basic such as the cutting tool selected has no helix angle and feed is low compared to tangential speed. However, as shown in the results constant force coefficients are not necessarily accurate enough. This issue can be solved by utilizing a well-known material. If the force model is not accurate enough, tests should be performed with the same angular speed every time in order to eliminate chip thickness difference from force calculation. In other words, it should be make sure as every excitation is done with same cutting parameters.

Significant cross correlation factors can distort identification of force coefficients if they are present. Likewise, current method does not offer an option to identify cross correlations. This issue has especially proven difficult for Y direction.

Due to lack of equipment that could take measurements during operation, application to the spindle of machine-tool has not been performed. There is no reason to think that this method cannot be applied to spindle if measurement is present such as a laser vibrometer. In addition, another possible application is to identify spindle through utilizing the given model since dynamic chip regeneration is affected by spindle dynamics. Identification of spindle with given model should be possible if dynamic chip thickness is intentionally increased.

As mentioned, methods for extending frequency response values into higher frequency domain are possible given zero crossings are controlled by angular speed of the cutter. Conversely, a lower frequency domain is studied as in most of articles listed in the introduction. Both cases offer additional challenges. A lower frequency domain requires higher excitations and dynamics of machine tool starts to become more significant. A higher frequencies means workpiece characteristics starts to be apparent.

Finally, the method should be extended to a lower frequency domain for operational identification because the literature indicates this is the frequency domain where operational FRFs can be different for machine-tool table.

To sum up, possible application areas are local FRF identification of machine tool structure, prediction of excitation and study of material force coefficient.

6.1 Industrial Applications

In terms of industrial applications, the thesis can be separated into three parts. Identification of force coefficients has the most immediate potential as dynamometers are not present in most manufacturing plants but chatter is a significant problem and force coefficients are a factor for chatter. Moreover, force coefficients are also a major determining factor for energy consumption. FRF identification is useful for quick identification of configurations where the machine-tool is more susceptible to vibrations. The milling model has not been designed for direct application. However, it is necessary for verification of results from experiments as checking for whether process parameters and machine-tool characteristics together allow the given identification process or not, even though dynamic chip regeneration can be safely omitted for most applications. In addition, being able to simulate vibrations, as mentioned in previous paragraphs, can be handy for future identification approaches.

In any sort of industrial application, the process should be re-developed in a way that it requires limited or no training from employees. Otherwise, the method can be offered as a package service.

.

REFERENCES

1. Hou, Junzhan & Zhou, Wei & Zhao, Ning. (2010). Methods for Prevention of Ignition during Machining of Magnesium Alloys. Key Engineering Materials. 447-448. 150-154. 10.4028/www.scientific.net/KEM.447-448.150.
2. Saleh, K. (2013). Modelling and analysis of Chatter Mitigation Strategies in milling (thesis).
3. What is OMA, https://community.sw.siemens.com/s/article/OMG-What-is-OMA-Operating-Modal-Analysis, last visited on June 2022
4. Bąk, P. A., & Jemielniak, K. (2016). Automatic experimental modal analysis of milling machine tool spindles. Proceedings of the Institution of Mechanical Engineers, Part B: Journal of Engineering Manufacture, 230(9), 1673–1683. https://doi.org/10.1177/0954405415623485
5. Kersting, P., Biermann, D. & Peuker, A. A measuring device for experimental modal analysis of thin-walled workpieces on five-axis milling machines. Int J Mater Form **3,** 451–454 (2010). https://doi.org/10.1007/s12289-010-0804-2
6. Koike, R. & Kakinuma, Yasuhiro & Aoyama, Tojiro & Ohnishi, Kouhei. (2016). Evaluation of Sensor-less Identification Method for Stable Spindle Rotation against Chatter with Milling Simulation Analysis. Procedia CIRP. 46. 169-172. 10.1016/j.procir.2016.03.138.doi: 10.1016/j.procir.2015.03.027
7. Cai, Hui & Luo, Bo & Mao, Xinyong & Gui, Lin & Song, Bao & Li, Bin & Peng, Fangyu. (2015). A Method for Identification of Machine-tool Dynamics under Machining. Procedia CIRP. 31. 502-507. 10.1016/j.procir.2015.03.027
8. Daming Wang and Yabing Pan , "A method to identify the main mode of machine tool under operating conditions", AIP Conference Proceedings 1829, 020039 (2017) https://doi.org/10.1063/1.4979771
9. Peng, Y., Li, B., Mao, X. et al. A method to obtain the in-process FRF of a machine tool based on operational modal analysis and experiment modal

analysis. Int J Adv Manuf Technol **95,** 3599–3607 (2018). https://doi.org/10.1007/s00170-017-1405-8

10. Bin Li, Bo Luo, Xinyong Mao, Hui Cai, Fangyu Peng, Hongqi Liu, A new approach to identifying the dynamic behavior of CNC machine tools with respect to different worktable feed speeds, International Journal of Machine Tools and Manufacture, Volume 72, 2013, Pages 73-84, ISSN 0890-6955, https://doi.org/10.1016/j.ijmachtools.2013.06.004.
11. Bin Li, Hui Cai, Xinyong Mao, Junbin Huang, Bo Luo, Estimation of CNC machine–tool dynamic parameters based on random cutting excitation through operational modal analysis, International Journal of Machine Tools and Manufacture, Volume 71, 2013, Pages 26-40, ISSN 0890-6955, https://doi.org/10.1016/j.ijmachtools.2013.04.001.
12. Iglesias, A. & Munoa, Jokin & Ramírez, C. & Ciurana, Joaquim & Dombovari, Z.. (2016). FRF Estimation through Sweep Milling Force Excitation (SMFE). Procedia CIRP. 46. 504-507. 10.1016/j.procir.2016.04.019
13. Özşahin, O., Budak, E., & Özgüven, H. N. (2011). Investigating Dynamics of Machine Tool Spindles under Operational Conditions. In Advanced Materials Research (Vol. 223, pp. 610–621). Trans Tech Publications, Ltd. https://doi.org/10.4028/www.scientific.net/amr.223.610
14. Berthold, Jan & Kolouch, Martin & Wittstock, Volker & Putz, Matthias. (2018). Identification of modal parameters of machine tools during cutting by operational modal analysis. Procedia CIRP. 77. 473-476. 10.1016/j.procir.2018.08.268
15. Li, B., Li, L., He, H. et al. Research on modal analysis method of CNC machine tool based on operational impact excitation. Int J Adv Manuf Technol **103,** 1155–1174 (2019). https://doi.org/10.1007/s00170-019-03510-x
16. Duan, Z., Li, C., Ding, W. et al. Milling Force Model for Aviation Aluminum Alloy: Academic Insight and Perspective Analysis. Chin. J. Mech. Eng. **34,** 18 (2021). https://doi.org/10.1186/s10033-021-00536-9

17. Caliskan, H., Kilic, Z. M., and Altintas, Y. (August 31, 2018). "On-Line Energy-Based Milling Chatter Detection." ASME. J. Manuf. Sci. Eng. November 2018; 140(11): 111012. https://doi.org/10.1115/1.4040617
18. Hui, Cai & Mao, Xinyong & Li, Bin & Luo, Bo. (2014). Estimation of FRFs of machine tools in output-only modal analysis. International Journal of Advanced Manufacturing Technology. 77. 117-130.
19. Pawełko, P., Powałka, B., & Berczyński, S. (2013). Estimation of cutting force model coefficients with regularized inverse problem. Advances in Manufacturing Science and Technology, 37(2). https://doi.org/10.2478/amst-2013-0012
20. Ag garwal, S., Nešić, N. & Xirouchakis, P. Cutting torque and tangential cutting force coefficient identification from spindle motor current. Int J Adv Manuf Technol **65,** 81–95 (2013). https://doi.org/10.1007/s00170-012-4152-x
21. Berthold, Jan & Kolouch, Martin & Wittstock, Volker & Putz, Matthias. (2016). Broadband excitation of machine tools by cutting forces for performing operational modal analysis. MM Science Journal. 2016. 1473-1481. 10.17973/MMSJ.2016_11_2016164.
22. Bediz, Bekir & Gozen, Bulent & Korkmaz, Emrullah & Ozdoganlar, O.. (2014). Dynamics of Ultra-High-Speed (UHS) Spindles used for Micromachining. International Journal of Machine Tools and Manufacture. 87. 10.1016/j.ijmachtools.2014.07.007
23. Yamato, Shuntaro & Imabeppu, Yasuhiro & Irino, Naruhiro & Suzuki, Norikazu & Kakinuma, Yasuhiro. (2019). Enhancement of Sensor-less Cutting Force Estimation by Tuning of Observer Parameters from Cutting Test. Procedia Manufacturing. 41. 272-279. 10.1016/j.promfg.2019.07.056.
24. Brecher, C. & Altstädter, H. & Daniels, M.. (2015). Axis Position Dependent Dynamics of Multi-axis Milling Machines. Procedia CIRP. 31. 508-514. 10.1016/j.procir.2015.03.068.
25. Zhou, Ji & Mao, Xinyong & Liu, Hongqi & Li, Bin & Peng, Yili. (2018). Prediction of cutting force in milling process using vibration signals of machine

tool. The International Journal of Advanced Manufacturing Technology. 99. 10.1007/s00170-018-2464-1.

26. Pulkit Gupta, Mohit Law, Suparno Mukhopadhyay, Evaluating tool point dynamics using output-only modal analysis with mass-change methods, CIRP Journal of Manufacturing Science and Technology, Volume 31, 2020, Pages 251-264, ISSN 1755-5817, https://doi.org/10.1016/j.cirpj.2020.06.001.
27. M. Martellotti, An analysis of milling process, ASME J. Manuf. Sci. Eng. 63 (1941) 677–700
28. Duan, Z., Li, C., Ding, W. et al. Milling Force Model for Aviation Aluminum Alloy: Academic Insight and Perspective Analysis. Chin. J. Mech. Eng. **34,** 18 (2021). https://doi.org/10.1186/s10033-021-00536-9
29. Mamedov, Ali. (2021). Micro Milling Process Modeling: A Review. Manufacturing Review. 8. 1-23. 10.1051/mfreview/2021003.
30. F A Niaki, A Pleta, L Mears. Trochoidal milling: investigation of a new approach on uncut chip thickness modeling and cutting force simulation in an alternative path planning strategy. Int. J. Adv. Manuf. Tech., 2018, 97(1-4): 641-656.
31. Koenigsberger, F. and Sabberwal, A. J. P. An investigation into the cutting forces pulsation during milling operations. Int. J. Mach. Tool Des. and Res., 1961, 1, 15–33
32. W.A. Kline, R.E. DeVor, The effect of runout on cutting geometry and forces in end milling, International Journal of Machine Tool Design and Research, Volume 23, Issues 2–3, 1983, Pages 123-140, ISSN 0020-7357, https://doi.org/10.1016/0020-7357(83)90012-4.
33. Budak, Erhan. (2006). Analytical models for high performance milling. Part I: Cutting forces, structural deformations and tolerance integrity. International Journal of Machine Tools and Manufacture. 46. 1478-1488. 10.1016/j.ijmachtools.2005.09.009.

34. E J A Armarego, R C Whitfield. Computer based modelling of popular machining operations for force and power prediction. CIRP Annals, 1985, 34(1): 65-69.
35. Yu, G., Wang, L. & Wu, J. Prediction of chatter considering the effect of axial cutting depth on cutting force coefficients in end milling. Int J Adv Manuf Technol **96,** 3345–3354 (2018). https://doi.org/10.1007/s00170-018-1745-z
36. Özşahin, O. (2018). Mikro takımların operasyon şartları altındaki uç nokta FTF'lerinin analitik yöntemler vasıtası ile belirlenmesi . Journal of the Faculty of Engineering and Architecture of Gazi University , 33 (2) , 529-540 . DOI: 10.17341/gazimmfd.416362
37. M. Postel, O. Özsahin, Y. Altintas, High speed tooltip FRF predictions of arbitrary tool-holder combinations based on operational spindle identification, International Journal of Machine Tools and Manufacture, Volume 129,2018, Pages 48-60, ISSN 0890-6955, https://doi.org/10.1016/j.ijmachtools.2018.03.004
38. Manufacturing Automation Laboratory, CUTPRO: MODAL ANALYSIS SOFTWARE MODULE (MODAL), https://www.malinc.com/products/cutpro/
39. Akçay, Recep & Akcay, Recep & Memiş, Emre & Memis, Emre & Özlü, Emre & Ozlu, Emre & Budak, Erhan. (2010). Havacılık sanayinde süreç optimizasyonu için kararlılık diyagramlarının kullanımı, 2. Ulusal Talaşlı İmalat Sempozyumu (UTIS 2010), Konya, Türkiye
40. Caixu YUE, Haining GAO, Xianli LIU, Steven Y. LIANG, Lihui WANG,A review of chatter vibration research in milling, Chinese Journal of Aeronautics, Volume 32, Issue 2, 2019, Pages 215-242, ISSN 1000-9361, https://doi.org/10.1016/j.cja.2018.11.007.
41. Wang, C., Zhang, X., Qiao, B., Cao, H., and Chen, X. (April 12, 2019), "Dynamic Force Identification in Peripheral Milling Based on CGLS Using Filtered Acceleration Signals and Averaged Transfer Functions." ASME. J. Manuf. Sci. Eng. June 2019; 141(6): 064501. https://doi.org/10.1115/1.4043362

42. IFFT, https://www.mathworks.com/help/matlab/ref/ifft.html, last visited on August 2022

APPENDICES

A. Appendix 1

This appendix gives FRF measurements through tap tests that is not presented at Chapters 3 and 4. This appendix verifies assumptions given as:

1. Cross-correlation factors are insignificant.
2. Measurement taken from workpiece is descriptive enough and as long as the direction is the same, placement position has limited effect.
3. Y direction is significantly stiffer.

Table A 1 gives differences between tap tests and Figure A 1 provides tap test hit spots. Figure A 2 and Figure A 3 gives tap test results regarding local variations of FRF of X and Y direction. Results indicate that while table position has no effect on FRF of X direction above 500 [Hz], different spots in Y direction has varying results. Measurement 3 is out of workpiece and likely dynamics of workpiece holder is involved. Movement in Z direction has also shown to be insignificant.

Table A 1: Tap Test Results (FRF) for Variations between Positions

Measurement	X Position [mm]	Z Position [mm]	Hydraulic Brakes	Motor Brakes
1	350	100	On	On
2	-350	100	On	On
3	-350	100	On	On
4	-350	100	On	On
5	-350	100	On	On
6	-350	100	Off	On
7	-350	100	Off	Off
8	-350	300	Off	Off
9	Same with 9	Same with 9	On	On
10	Same with 10	Same with 10	On	On

Measurements 9 and 10 were older and their exact position is missing. However, table position did not change.

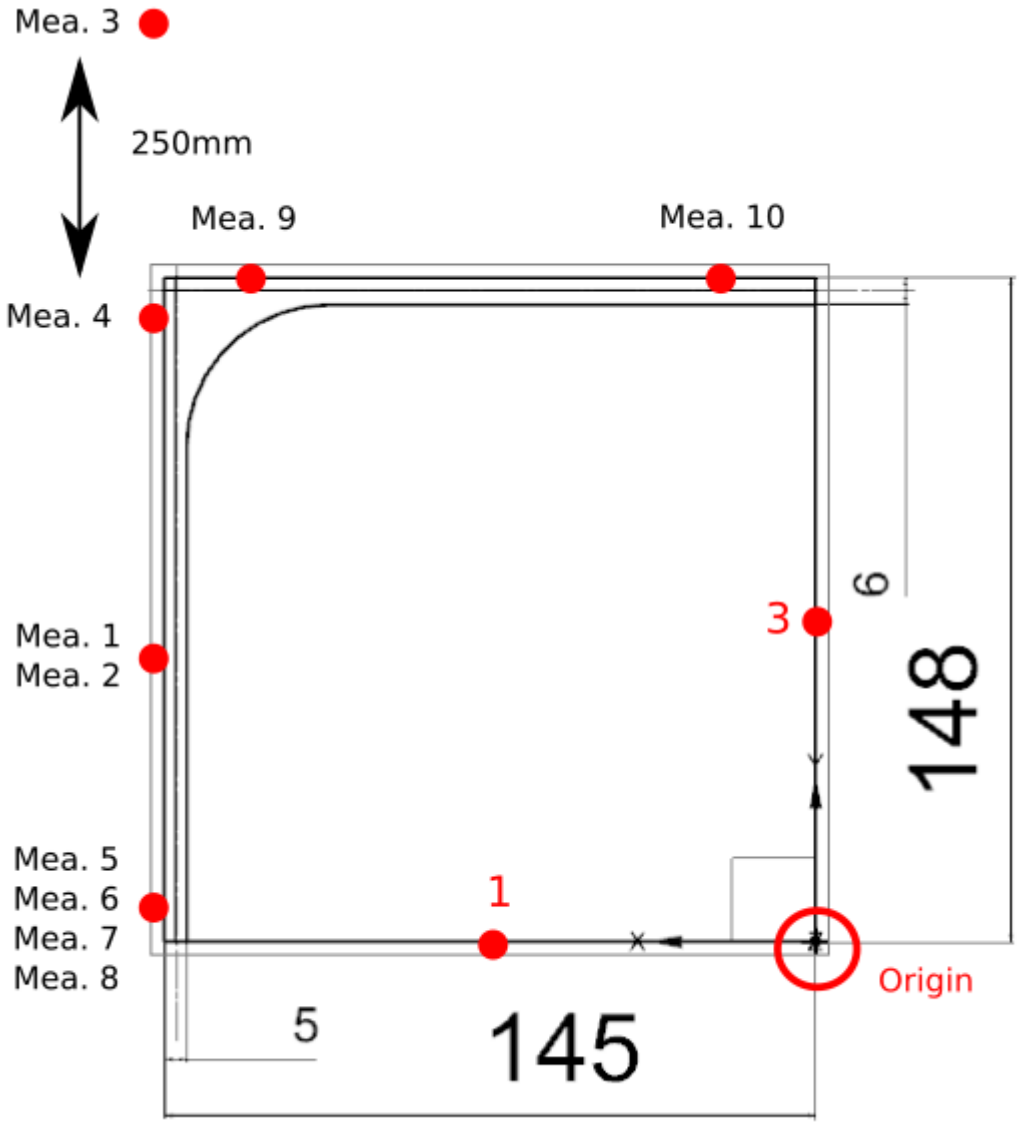

Figure A 1 Positions of Tap Test Spots

Hydraulic braking is also shown to be insignificant. Variation of FRF amplitude in domain 1500-2000 [Hz] should be a focus point. In addition, coherence values may be found at Figure A 4 to Figure A 7.

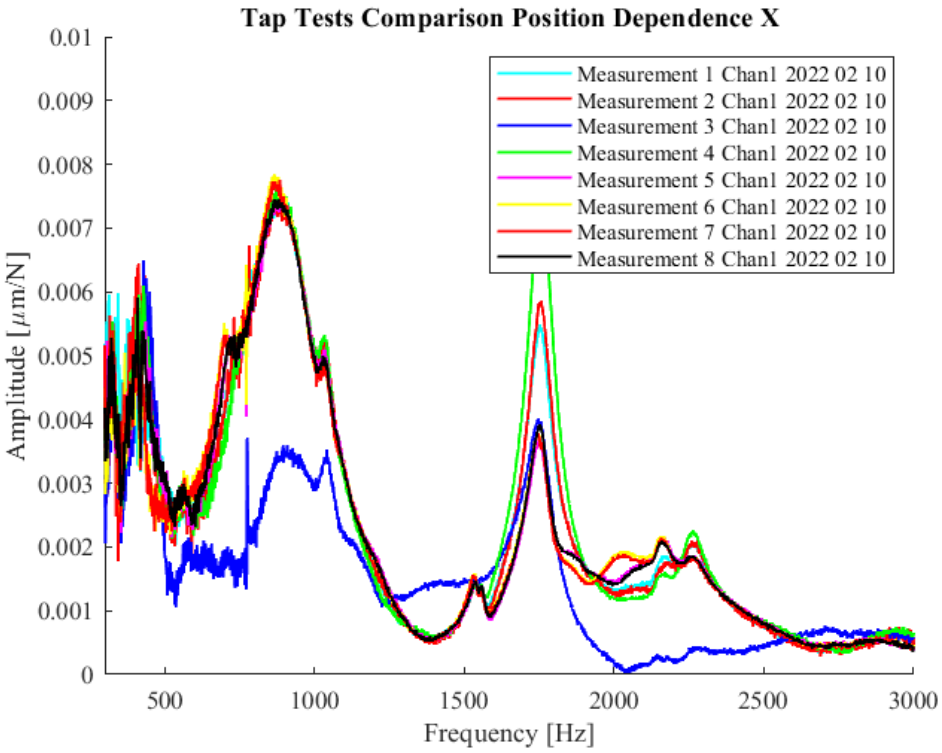

Figure A 2 X direction Tap Test Results from Various Spots

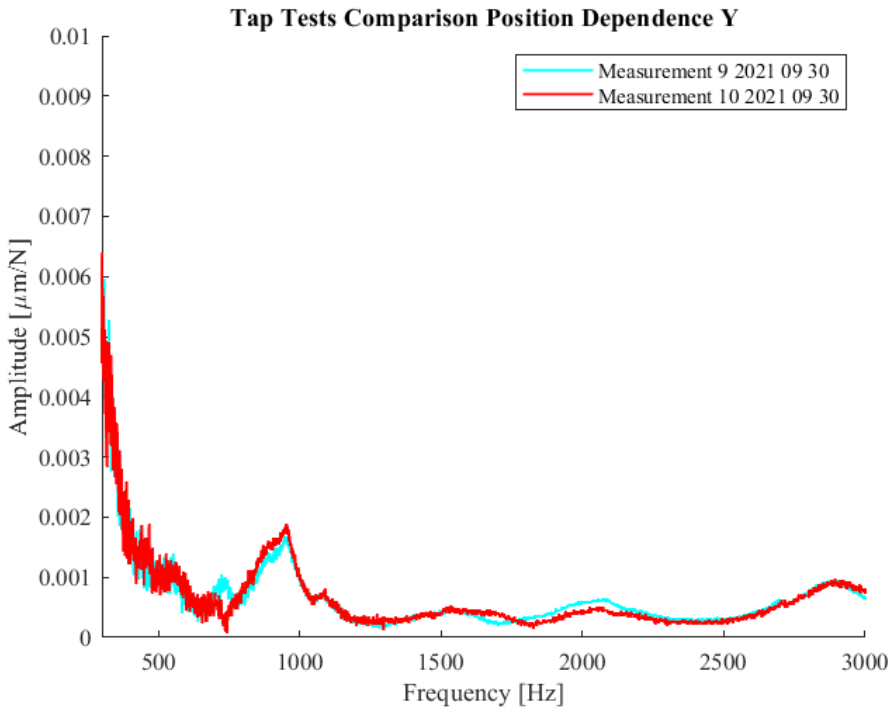

1

Figure A 3 Y direction Tap Test Results from Various Spots

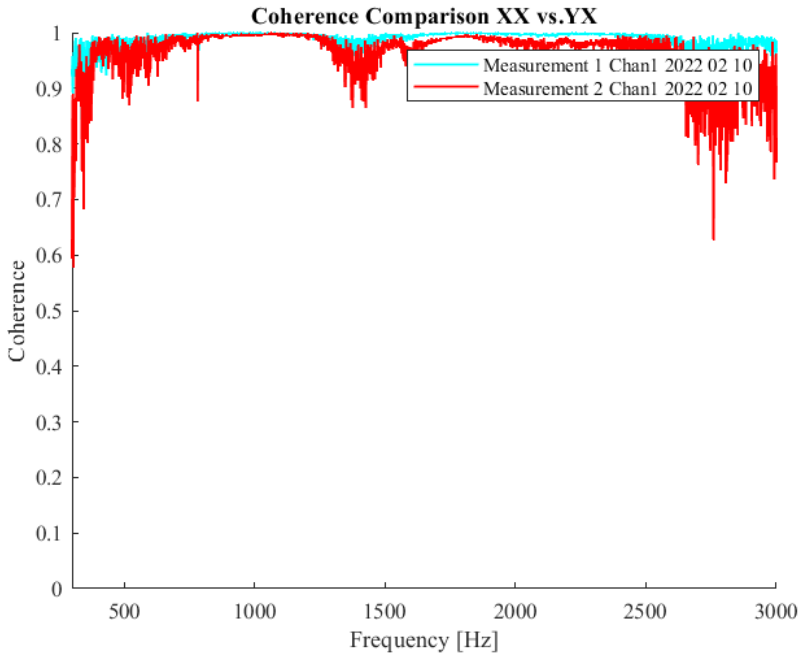

Figure A 4 Coherences of Previous Measurements 1 and 2

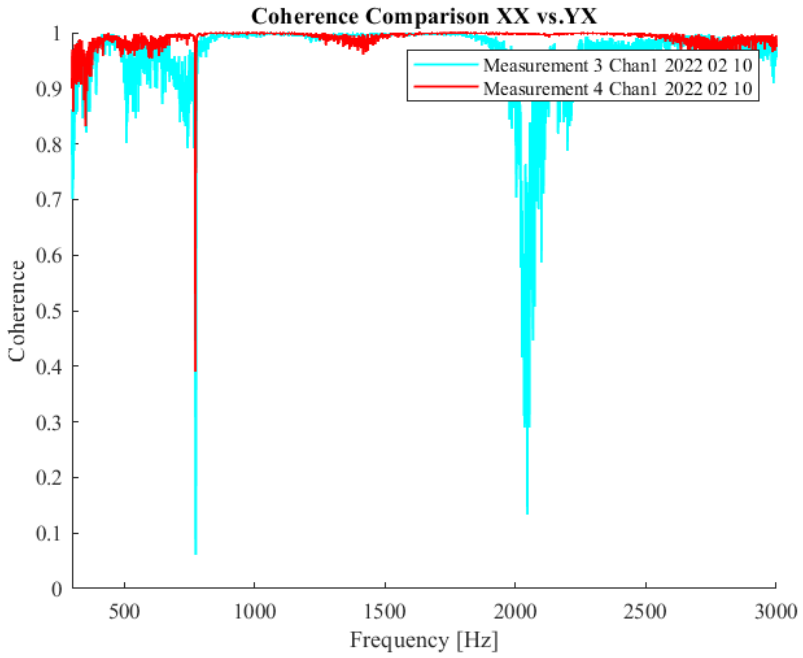

Figure A 5 Coherences of Previous Measurements 3 and 4

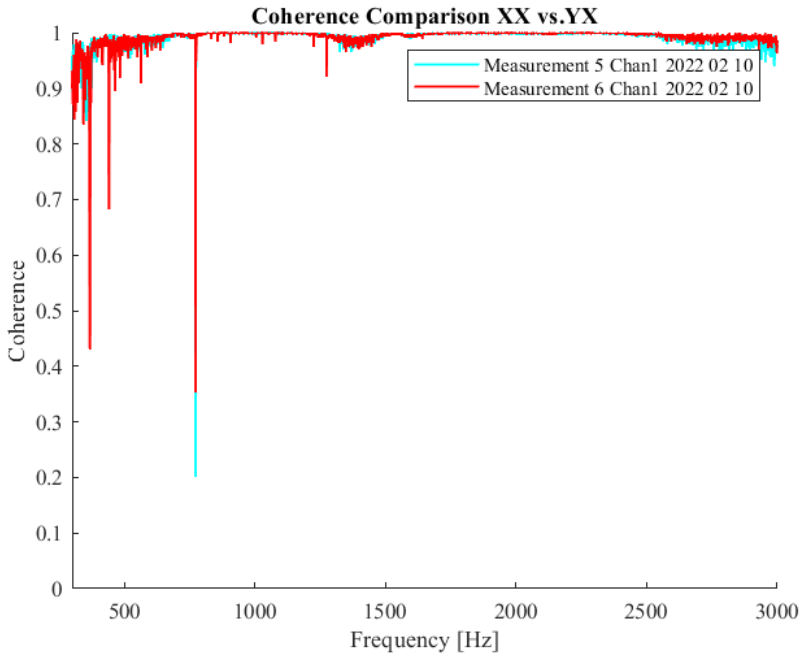

Figure A 6 Coherences of Previous Measurements 5 and 6

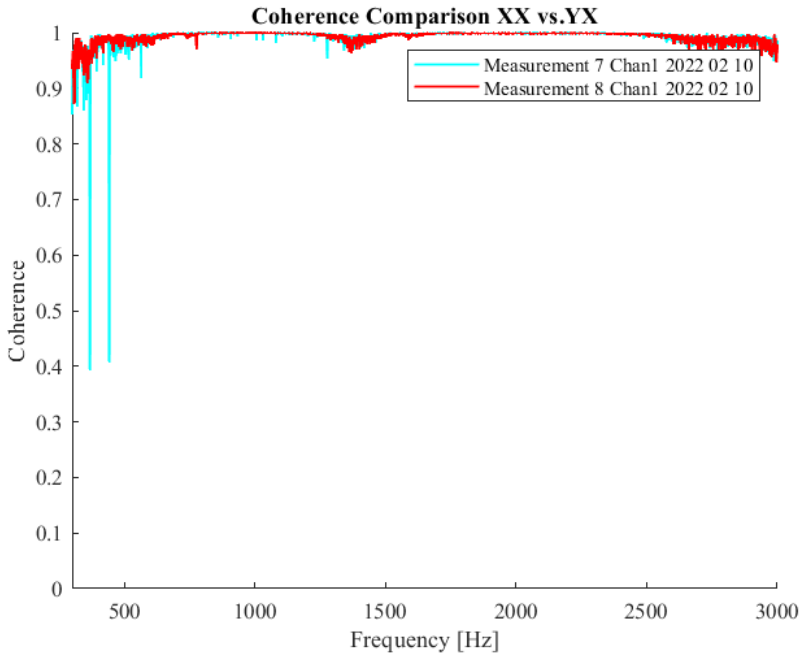

Figure A 7 Coherences of Previous Measurements 7 and 8

B. Appendix 2

This appendix shows that direct application of equation (3.5) for least squares method is not feasible because direct application of $\mathbf{H}(\omega)$ returns ill-conditioned matrice.

$\mathbf{H}(\omega)$ is defined as below:

$$\mathbf{H}(\omega) = \begin{bmatrix} \mathrm{H_{tc,x}}(\omega) & \mathrm{H_{rc,x}}(\omega) & \mathrm{H_{te,x}}(\omega) & \mathrm{H_{re,x}}(\omega) \\ \mathrm{H_{tc,y}}(\omega) & \mathrm{H_{rc,y}}(\omega) & \mathrm{H_{te,y}}(\omega) & \mathrm{H_{re,y}}(\omega) \end{bmatrix} \tag{B.1}$$

It can be formatted to a simpler form:

$$\mathbf{H}(\omega) = \begin{bmatrix} a_{11} & a_{12} & a_{13} & a_{14} \\ -a_{12} & a_{11} & -a_{14} & a_{13} \end{bmatrix} \tag{B.2}$$

$$a_{11} = \mathcal{F}\left(-\mathrm{c a_p} \cos\big(\theta(\mathrm{t})\big) \sin\big(\theta(\mathrm{t})\big)\, \mathrm{g}(t)\right) \tag{B.3}$$

$$a_{12} = \mathcal{F}\left(-\mathrm{c a_p} \sin^2\big(\theta(\mathrm{t})\big)\, \mathrm{g}(t)\right) \tag{B.4}$$

$$a_{13} = \mathcal{F}\left(-\mathrm{a_p} \cos\big(\theta(\mathrm{t})\big)\, \mathrm{g}(t)\right) \tag{B.5}$$

$$a_{14} = \mathcal{F}\left(-\mathrm{a_p} \sin\big(\theta(\mathrm{t})\big)\, \mathrm{g}(t)\right) \tag{B.6}$$

Here, a_{11} is a member of matrice $\mathbf{H}(\omega)$. Direct application of least squares method could look like this:

$$\begin{bmatrix} \mathrm{K_{tc}} \\ \mathrm{K_{rc}} \\ \mathrm{K_{te}} \\ \mathrm{K_{re}} \end{bmatrix} = (\mathbf{H^T H})^{-1} \mathbf{H^T} \widehat{\mathbf{F}_s}(\omega) \tag{B.7}$$

In this case $\mathbf{H^T H}$ can be written as:

$$\mathbf{H^T H} = \begin{bmatrix} a_{11} & -a_{12} \\ a_{12} & a_{11} \\ a_{13} & -a_{14} \\ a_{14} & a_{13} \end{bmatrix} \begin{bmatrix} a_{11} & a_{12} & a_{13} & a_{14} \\ -a_{12} & a_{11} & -a_{14} & a_{13} \end{bmatrix} \tag{B.8}$$

$$= \begin{bmatrix} a_{11}a_{11} + a_{12}a_{12} & a_{11}a_{12} - a_{12}a_{11} & a_{11}a_{13} + a_{12}a_{14} & a_{11}a_{14} - a_{12}a_{13} \\ a_{11}a_{12} - a_{12}a_{11} & a_{11}a_{11} + a_{12}a_{12} & -a_{11}a_{14} + a_{12}a_{13} & a_{11}a_{13} + a_{12}a_{14} \\ a_{11}a_{13} + a_{12}a_{14} & -a_{11}a_{14} + a_{12}a_{13} & a_{13}a_{13} + a_{14}a_{14} & a_{13}a_{14} - a_{14}a_{13} \\ a_{11}a_{14} - a_{12}a_{13} & a_{11}a_{13} + a_{12}a_{14} & a_{13}a_{14} - a_{14}a_{13} & a_{13}a_{13} + a_{14}a_{14} \end{bmatrix}$$

$$= \begin{bmatrix} a_{11}a_{11} + a_{12}a_{12} & 0 & a_{11}a_{13} + a_{12}a_{14} & a_{11}a_{14} - a_{12}a_{13} \\ 0 & a_{11}a_{11} + a_{12}a_{12} & -a_{11}a_{14} + a_{12}a_{13} & a_{11}a_{13} + a_{12}a_{14} \\ a_{11}a_{13} + a_{12}a_{14} & -a_{11}a_{14} + a_{12}a_{13} & a_{13}a_{13} + a_{14}a_{14} & 0 \\ a_{11}a_{14} - a_{12}a_{13} & a_{11}a_{13} + a_{12}a_{14} & 0 & a_{13}a_{13} + a_{14}a_{14} \end{bmatrix} \quad \text{(B.9)}$$

$a_{11}a_{14} - a_{12}a_{13}$ can be written as below:

$$\begin{aligned} & a_{11}a_{14} - a_{12}a_{13} \\ & = \mathcal{F}\left(-\mathrm{ca_p}\cos\big(\theta(\mathrm{t})\big)\sin\big(\theta(\mathrm{t})\big)\,\mathrm{g}(t)\right)\mathcal{F}\left(-\mathrm{a_p}\sin\big(\theta(\mathrm{t})\big)\,\mathrm{g}(t)\right) \\ & - \mathcal{F}\left(-\mathrm{ca_p}\sin^2\big(\theta(\mathrm{t})\big)\,\mathrm{g}(t)\right)\mathcal{F}\left(-\mathrm{a_p}\cos\big(\theta(\mathrm{t})\big)\,\mathrm{g}(t)\right) \end{aligned} \quad \text{(B.10)}$$

$$= \frac{\mathrm{ca_p^2}}{2\pi}\int_{-\infty}^{\infty}\cos\big(\theta(\mathrm{t})\big)\sin\big(\theta(\mathrm{t})\big)\sin\big(\theta(\mathrm{t}-\tau)\big)\,d\tau$$

$$-\frac{\mathrm{ca_p^2}}{2\pi}\int_{-\infty}^{\infty}\cos\big(\theta(\mathrm{t}-\tau)\big)\sin\big(\theta(\mathrm{t})\big)\sin\big(\theta(\mathrm{t})\big)\,d\tau = 0$$

$\mathbf{H^T H}$ can be re-written as:

$$\mathbf{H^T H} = \begin{bmatrix} a_{11}a_{11} + a_{12}a_{12} & 0 & a_{11}a_{13} + a_{12}a_{14} & 0 \\ 0 & a_{11}a_{11} + a_{12}a_{12} & 0 & a_{11}a_{13} + a_{12}a_{14} \\ a_{11}a_{13} + a_{12}a_{14} & 0 & a_{13}a_{13} + a_{14}a_{14} & 0 \\ 0 & a_{11}a_{13} + a_{12}a_{14} & 0 & a_{13}a_{13} + a_{14}a_{14} \end{bmatrix} \quad \text{(B.11)}$$

Replacing columns 2 and 3 with each other gives:

$$\mathbf{H^T H} = \begin{bmatrix} a_{11}a_{11} + a_{12}a_{12} & a_{11}a_{13} + a_{12}a_{14} & 0 & 0 \\ a_{11}a_{13} + a_{12}a_{14} & a_{13}a_{13} + a_{14}a_{14} & 0 & 0 \\ 0 & 0 & a_{11}a_{11} + a_{12}a_{12} & a_{11}a_{13} + a_{12}a_{14} \\ 0 & 0 & a_{11}a_{13} + a_{12}a_{14} & a_{13}a_{13} + a_{14}a_{14} \end{bmatrix} \quad \text{(B.12)}$$

This results in ill-conditioned matrice.